Direct Numerical Simulation of dynamic droplet wetting on superhydrophobic substrates by means of a diffuse-interface phase-field method using OpenFOAM

Direkte Numerische Simulation dynamischer Benetzungsprozesse von Tropfen auf superhydrophoben Oberflächen mittels einer Diffuse-Interface Phasenfeldmethode in OpenFOAM

Master Thesis by Michael Holzinger, Department of Computational Engineering

April 11, 2019

Supervisors: Prof. Dr. Dieter Bothe, Dr.-Ing. Holger Marschall
Department of Mathematics, Group Mathematical Modeling and Analysis

TECHNISCHE
UNIVERSITÄT
DARMSTADT

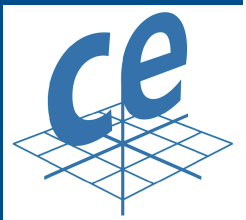

Direct Numerical Simulation of dynamic droplet wetting on superhydrophobic substrates by means of a diffuse-interface phase-field method using OpenFOAM

Direkte Numerische Simulation dynamischer Benetzungsprozesse von Tropfen auf superhydrophoben Oberflächen mittels einer Diffuse-Interface Phasenfeldmethode in OpenFOAM

Vorgelegte Master Thesis von Michael Holzinger

1. Gutachten: Prof. Dr. Dieter Bothe
2. Gutachten: Dr.-Ing. Holger Marschall

Tag der Einreichung:

Erklärung zur Abschlussarbeit gemäß §23 Abs. 7 APB der TU Darmstadt

Hiermit versichere ich, Michael Holzinger, die vorliegende Master-Thesis ohne Hilfe Dritter und nur mit den angegebenen Quellen und Hilfsmitteln angefertigt zu haben. Alle Stellen, die Quellen entnommen wurden, sind als solche kenntlich gemacht worden. Diese Arbeit hat in gleicher oder ähnlicher Form noch keiner Prüfungsbehörde vorgelegen.

Mir ist bekannt, dass im Falle eines Plagiats (§38 Abs.2 APB) ein Täuschungsversuch vorliegt, der dazu führt, dass die Arbeit mit 5,0 bewertet und damit ein Prüfungsversuch verbraucht wird. Abschlussarbeiten dürfen nur einmal wiederholt werden.

Bei der abgegebenen Thesis stimmen die schriftliche und die zur Archivierung eingereichte elektronische Fassung überein.

Thesis Statement pursuant to §23 paragraph 7 of APB TU Darmstadt

I herewith formally declare that I, Michael Holzinger, have written the submitted thesis independently. I did not use any outside support except for the quoted literature and other sources mentioned in the paper. I clearly marked and separately listed all of the literature and all of the other sources which I employed when producing this academic work, either literally or in content. This thesis has not been handed in or published before in the same or similar form.

I am aware, that in case of an attempt at deception based on plagiarism (§38 Abs. 2 APB), the thesis would be graded with 5,0 and counted as one failed examination attempt. The thesis may only be repeated once.

In the submitted thesis the written copies and the electronic version for archiving are identical in content.

Datum/Date: Unterschrift/Signature:

_____ _____

Abstract

The dynamic wetting process and shape evolution of a droplet impacting perpendicular on a planar, plain and super-hydrophobic substrate are investigated by means of direct numerical simulation of an immiscible and isothermal binary fluid system. A diffuse-interface phase-field method is used, where the Cahn-Hilliard equation, describing the evolution of the phase-field parameter, is coupled with the Navier-Stokes system. The model parameter of the phase-field method are the capillary width, the mobility, the mixing energy parameter and the equilibrium contact angle on fluid-solid boundaries. The mixing energy parameter model will be extended in this work in order to deal with dynamic out-of equilibrium behavior of the diffuse-interface on a local scope. 2D-axis-symmetric simulations in combination with adaptive mesh refinement will be performed, the latter allowing for an immense reduction of control volumes far from the diffuse-interface. For validation, two experimental setups are chosen, which have comparable involved dynamics. First, the wetting factors for a water droplet with diameter 2.04 mm and initial velocity $0.83\,\mathrm{m\,s^{-1}}$ on a substrate with contact angle 145° is studied, determining appropriate phase-field parameters. Subsequently, the shape evolution of a water droplet with diameter 1.97 mm and initial velocity $1.0\,\mathrm{m\,s^{-1}}$ on a substrate with contact angle 160° is validated using parameter sets from previous simulations. For all simulations different mixing energy parameters models are compared with each other.

Kurzfassung

Der dynamische Benetzungsprozess und die Profilentwicklung eines Wassertropfens, der senkrecht auf eine ebene, glatte und super-hydrophobe Oberfläche aufprallt, wird durch Direkte Numerischen Simulation eines unvermischbaren, isothermen Zweiphasen-Gemisches untersucht. Eine Diffuse-Interface Phasenfeldmethode kommt zum Einsatz, bei der die Cahn-Hilliard Gleichung, welche die Entwicklung des Phasenfeldparameters beschreibt, mit den Navier-Stokes Gleichungen gekoppelt wird. Die Modellparameter der Phasenfeldmethode sind die Kapillarbreite, die Mobilität, der Mischungsenergieparameter und der Gleichgewichtswinkel an Fluid-Festkörper Rändern. Das Model des Mischungsenergieparameters wird im Rahmen dieser Arbeit erweitert, um lokal die Dynamik eines aus dem Gleichgewicht gebrachten Diffuse-Interfaces zu beschreiben. 2D-achsensymmerische Simulationen werden durchgeführt in Kombination mit Adaptiver Gitterverfeinerung, welche die Anzahl der Kontrollvolumen abseits des Diffuse-Interfaces deutlich reduziert. Zur Validierung werden zwei Experimente ausgesucht, welche eine vergleichbare Dynamik aufweisen. Zu Beginn wird der Benetzungsfaktor eines Wassertropfens mit 2.04 mm Durchmesser und einer Anfangsgeschwindigkeit von $0.83\,\mathrm{m\,s^{-1}}$ auf einer Oberfläche mit einem Kontaktwinkel von 145° untersucht, wobei geeignete Modellparameter bestimmt werden. Danach wird die Profilentwicklung eines Wassertropfens mit 1.97 mm Durchmesser und einer Anfangsgeschwindigkeit von $1.0\,\mathrm{m\,s^{-1}}$ auf einer Oberfläche mit einem Kontaktwinkel von 160° validiert, unter Verwendung der Parameter aus den vorherigen Simulationen. Bei allen Simulationen werden verschiedene Modelle des Mischungsenergieparameters miteinander verglichen.

Contents

1 Introduction

Nowadays, wetting processes play an important role in many industrial applications, for example painting and coating or fuel injection. Special properties of the involved surfaces, notably super-hydrophobicity, lead to many forward-looking technologies such as water-proofing of textiles or drag reduction in microchannels [4]. Natural or artificial super-hydrophobic surfaces are realized by nano- and micrometer scaled structures (Fig. 1.1a) leading to a layer of air underneath a piled drop, which is refered to as the Cassie or Fakir state [5]. Macroscopically, the contact angle between droplet and surface exceeds 90°, which results to a bulge of droplet volume over the contact area, see Fig. 1.1b-c. In the past few years, experimental studies have established a new understanding of how water drops advance on super-hydrophobic surfaces [4–6]. In motion direction the apparent advancing contact angle is 180° because the droplet bends down to the next micropillar. On the receding site, pinning and depinning events occur, where capillary bridges are formed and released. Such events are related with energy dissipation and high dynamic local behavior of the droplet-gaseous interface. Measuring methods are limited, hence a model-based analysis of experimental results is done to gain more insights. A direct numerical simulation is needed.

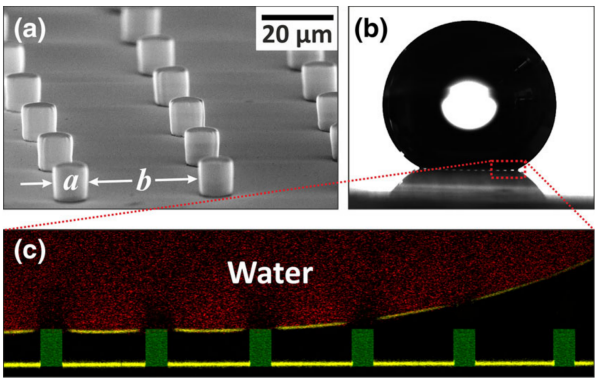

Figure 1.1.: (a) Array of micropillar structures scanned with electron micrograph. (b) Water droplet on a micro-structured super-hydrophobic substrate. (c) Confocal microscope image of the Cassie state. All images taken from [5].

An established way to describe fluids is by means of continuum mechanics, more precisely the Navier-Stokes equations. If a system of multiple fluids is considered, interfaces have to be modeled. Various diffuse-interface models exist, which describe the interface with a finite thickness, where physical properties vary continuously between pure bulk fluid phases. One representative used in this work is the Cahn-Hilliard diffuse-interface model, which introduces a phase-field variable acting as an order parameter to distinguish different fluid phases. Many works have used simulations based on the Cahn-Hilliard formulation, notably Jacqmin [7, 8], Ding et al. [9] and Yue et al. [1, 10]. The Cahn-Hilliard model is based on an energy formulation of the interface. The model parameter set determines the interfacial thickness, the Cahn-Hilliard diffusion and the energy content of the interface, the latter associated with a so-called mixing energy parameter. Naturally on a nanometer scale, the interfacial thickness is artificially enlarged, so that computations with feasible costs are possible. The Cahn-Hilliard diffusion is the driving force of fluid phase interactions within the diffuse interface. Diffuse-Interface models do not necessarily need microstructures to create super-hydrophobicity because the equilibrium contact angle is typically set as a parameter.

This work is restricted to an isothermal, immiscible system of two phases with density and viscosity contrast, here water and air at room temperature. A dynamic test case setup is applied, where a droplet impacts perpendicular on a plane, smooth substrate with an initial velocity and no initial height. For the first time the PHASEFIELDFOAM-solver, implemented in FOAM-EXTEND 3.2 and 4.0, is excessively used to validate the simulated transient characteristics of droplet spreading in such a dynamic wetting scenario. The interesting characteristics are the contact line motion, described by the so-called wetting factor, and the droplet shape behavior; corresponding experiments have been done by Roisman et al. [2] and Yun [3]. Improvements of the PHASEFIELDFOAM-solver will be investigated for the first time systematically, which are the coupled solution procedure for the phase-field equation in combination with adaptive mesh refinement. The latter will exhibit a tremendous reduction of computational costs, making former simulations on clusters run on a single-core standard laptop in the same time.

Fundamental questions of this work are: Can the diffuse-interface phase-field model appropriately describe dynamic wetting processes on super-hydrophobic substrates using simplifications like absent solid micro-structures or a fairly simple model for the contact angle? Is the assumption of a homogeneous mixing energy parameter still justified when the interface is exposed to dynamic processes?

The main objective of this work is to study three different models for the mixing energy parameter to deal with dynamic, out of equilibrium relaxation processes of the interface. So far the standard formulation for the mixing energy parameter is a temporally and spatially constant, homogeneous model throughout the whole computational domain. Yue et al. have proposed an approach which recalculates the mixing energy parameter every time-step, but still is spatially constant [1]. In this work a new mixing energy parameter approach is derived and tested thoroughly, which, to the author's knowledge, has not been reported yet. Another important topic, yet not main objective of this work, is the implementation of the viscosity model within the PHASEFIELDFOAM-solver. In summary, the simulation campaign will find an appropriate set of phase-field parameters for the given test cases, while testing two different implementations of the viscosity model and three different models for the mixing energy parameter.

2 Continuum Model

The phase-field method in the spirit of Cahn and Hilliard is introduced in the context of diffuse interface models for a mixture of two immiscible and isothermal fluids. The corresponding governing equations and the boundary conditions are presented as they are implemented in the phaseFieldFoam-solver. The generic structure of the governing equations and the closures are presented in subsequent sections to give rise to a potential variation of constitutive equations or rheological models. In the final section a new model with a local formulation of the mixing energy parameter is presented, which can be seen as extension of the global approach by Yue et al. [1].

2.1 Cahn-Hilliard Phase-Field Model

Fluid interfaces and their evolution or transport can be represented either by sharp- or diffusive-interface models. The latter goes back to the work of van der Waals [11], who formulated a continuous variation of density and viscosity between two fluids, unlike sharp-interface models, which assume a jump-discontinuity. Diffusive-interface models can be subdivided further into several sub-models. Therein, the phase-field model for immiscible fluids, going back to Hohenberg and Halperin [12], uses an energy-based variational formalism modeling the fluid free energy. As a consequence, deformations of the interface are described by a non-local mixing energy, balancing mixing and decomposition processes.

In this work the so-called Cahn-Hilliard phase-field model for diffuse interfaces is used. The transport of the phase-field parameter χ, acting as an order parameter to separate two phases, reads in its closed form

$$\partial_t \chi + \mathbf{u} \cdot \nabla \chi = \nabla^{\bullet}(\kappa \nabla \Phi(\chi)), \tag{2.1}$$

where κ is a non-negative diffusion coefficient denoted as the mobility, Φ is the chemical potential depended on the phase-field parameter itself and $\mathbf{u}$ is the barycentre velocity [1, 13]. In the following sections an expression for Φ will be derived using the energy-based formalism of the Cahn-Hilliard phase-field model. A functional expression is shown, which describes the phase-field parameter in a planar interface in equilibrium state. On this basis, the natural boundary condition of the phase-field on fluid-solid boundaries will be derived.

2.1.1 Helmholtz Free Energy

In their pioneering work [14], Cahn and Hilliard defined a mixing energy density f_{mix} to be a function of the phase-field parameter $\chi \in [-1, 1]$ and its corresponding gradient. The mixing energy density models the molecular interaction between different fluid phases. Integration of f_{mix} over the domain Ω yields the Helmholtz free energy F of a fluid system as

$$F(\chi, \nabla\chi) = \int_{\Omega} f_{\text{mix}}(\chi, \nabla\chi)\, d\mathbf{x} = \int_{\Omega} \left(\frac{\lambda}{\epsilon^2} \Psi(\chi) + \frac{\lambda}{2} |\nabla\chi|^2 \right) d\mathbf{x}. \tag{2.2}$$

Herein, λ is called mixing energy parameter scaling the mixing energy density, ϵ is a measure of the interfacial thickness called capillary width [1] and $\Psi(\chi)$ is a potential. The potential Ψ is chosen as a so-called double-well potential according to Ginzburg and Landau [15], which takes the form

$$\Psi(\chi) = \frac{1}{4}\left(\chi^2 - 1\right)^2. \tag{2.3}$$

The first term of f_{mix} in (2.2) represents an energy density, which vanishes in the pure bulk phases ($\chi \to \pm 1$) and has a maximum at the center of the interface ($\chi = 0$). Since two-phase systems in nature tend to minimizes the free surface energy, the potential term tends to separate different fluid phases from each other. The second term with the gradient expression of the phase-field parameter in (2.2) has the opposite effect, forcing mixing of different fluid phases. Note that other choices of the potential $\Psi(\chi)$ are possible, but the Ginzburg-Landau potential is the most often encountered model in literature, for example in [1, 9].

In a variational process the Helmholtz free energy F is minimized. The chemical potential is defined as the functional derivative of F with respect to the phase-field parameter, viz.

$$\Phi(\chi) := \frac{\delta F(\chi)}{\delta \chi} = \frac{\lambda}{\epsilon^2}\Psi'(\chi) - \lambda\nabla^2\chi. \tag{2.4}$$

As Jacqmin [7] pointed out, two mechanisms exist to adjust an interface that has been driven out of equilibrium. Firstly, gradients of the chemical potential lead to induced transport in the fluid system components, which is referred to as a diffusional mechanism. Secondly, the chemical potential will be part of a source term in the linear momentum equation, hence an advection mechanism takes place as well.

2.1.2 Diffuse-Interface

The Cahn-Hilliard phase-field model can describe a system of multiple fluids, where every pair of fluid components have an individual phase-field parameter modeled by (2.1) and an individual mixing energy density leading to a global Helmholtz free energy. However, this work is restricted to a binary system only. Fig. 2.1a shows a scenario of two fluids with densities $\rho_{\text{A}}, \rho_{\text{B}}$ and kinematic viscosities $\nu_{\text{A}}, \nu_{\text{B}}$ embedded in a domain Ω. In the pure bulk phase of fluid A the phase-field parameter takes the value -1 and for fluid B the value 1, respectively. Interim values indicate the interfacial region of finite thickness. The phase-field parameter varies over the interfacial region in a smooth but rapid way.

If the interface is assumed to be planar and in an equilibrium state, i.e. the chemical potential in (2.4) vanishes, the solution of the one-dimensional equation $\Phi(\chi(n)) = 0$, where n varies in interfacial normal direction, is given by

$$\chi_{\text{eq}}(n) = \tanh\left(\frac{n}{\sqrt{2}\epsilon}\right). \tag{2.5}$$

In equilibrium the thickness of the interface is uniform over the whole domain. As shown in Fig. 2.1b about 90% of the whole variation of χ occurs over length of $L = 4.1641\epsilon$. The tangent hyperbolic profile in (2.5) is only valid for the Ginzburg-Landau potential (2.3).

A model for the mixing energy parameter λ is derived using the fluid-fluid interfacial tension (surface tension) $\sigma = \text{const.}$ from the sharp-interface context [10]. The one-dimensional matching condition reads

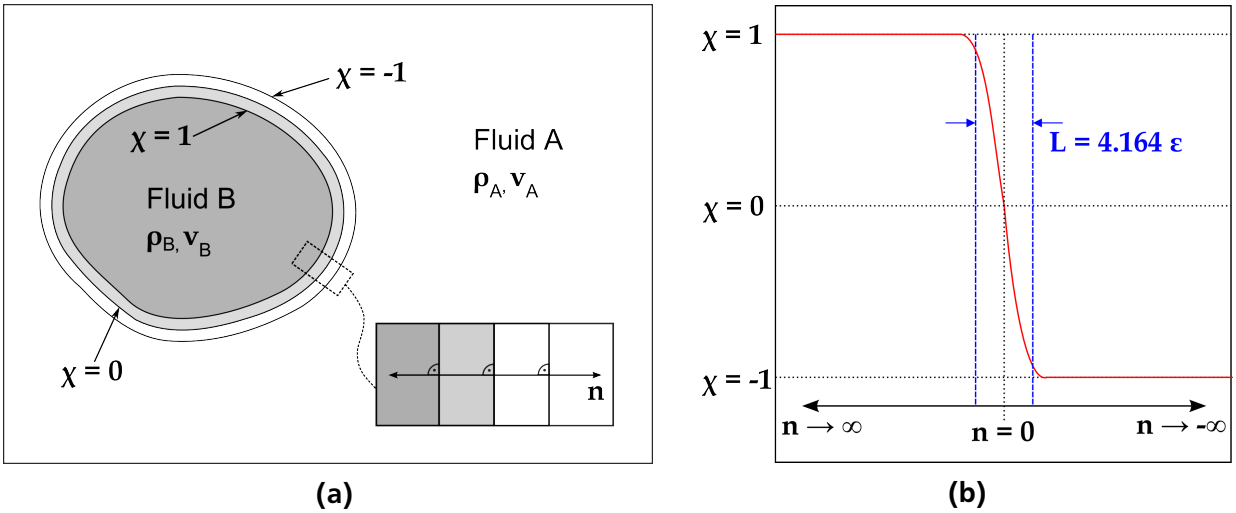

Figure 2.1.: Diffuse-interface model (a) of a binary fluid mixture with (b) a tangent hyperbolic transition of the phase-field parameter.

$$\sigma = \int_{-\infty}^{\infty} f_{\text{mix}}\, dn = \lambda \int_{-\infty}^{\infty} \left[\frac{1}{4\epsilon^2} \left(\chi_{\text{eq}}^2 - 1 \right)^2 + \frac{1}{2} \left(\frac{d\chi_{\text{eq}}}{dn} \right)^2 \right] dn \tag{2.6}$$

$$\overset{(2.5)}{\Rightarrow} \quad \lambda = \frac{3}{2\sqrt{2}} \sigma \epsilon \tag{2.7}$$

Eq. 2.7 will be referred to as the homogeneous mixing energy parameter model for λ, which is valid over the whole domain Ω and constant if the capillary width ϵ is constant. In this sense, ϵ can be considered as a main phase-field parameter and λ being only a secondary derived property if one wishes to relate to surface tension in the sharp-interface context.

2.1.3 Fluid-Solid Boundaries

When a binary fluid system in the sharp-interface context is in contact with a solid surface (wall), a contact line is established, see Fig. 2.2a. Young's law,

$$\sigma \cos \theta_{\text{e}} = \sigma_{\text{sA}} - \sigma_{\text{sB}}, \tag{2.8}$$

is used to describe the equilibrium contact angle θ_{e} from the fluid-fluid interfacial tension σ and the fluid-solid interfacial tensions σ_{sA} and σ_{sB} [10]. However, in the diffuse-interface model, Fig. 2.2b, there is no localised contact line but an interfacial zone. A contact line in the sense of a diffuse interface can only be interpreted as the iso-contour line for $\chi = 0$ ending on the wall. It is an advantage of the diffuse interface that contact line motion is observed, although no-slip conditions for the velocity are present [7]. While the mixing energy density f_{mix} is used to describe the inner domain of the fluid system, a wall energy density $f_{\text{w}}(\chi)$ applies on the solid surface. The free energy of the system reads [10]

$$F(\chi, \nabla\chi) = \int_{\Omega} f_{\text{mix}}(\chi, \nabla\chi)\, d\mathbf{x} + \int_{\partial\Omega} f_{\text{w}}(\chi)\, dS. \tag{2.9}$$

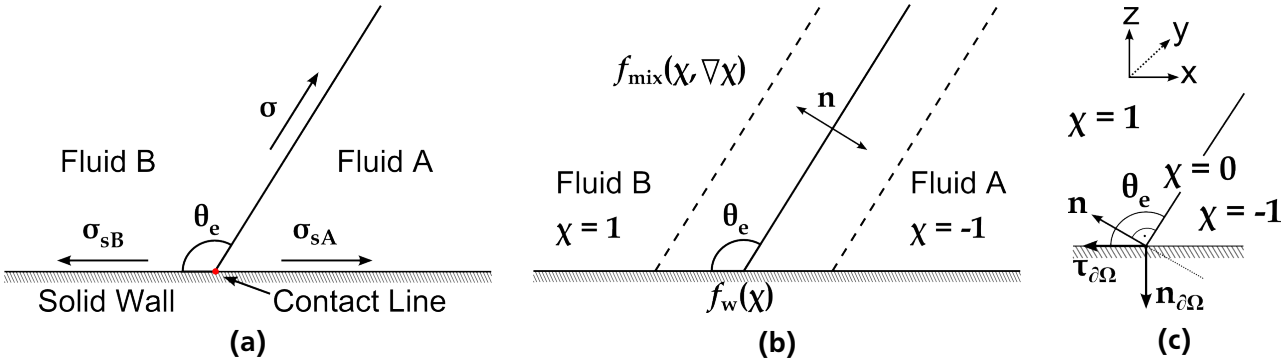

Figure 2.2.: Binary fluid system on a super-hydrophobic substrate with equilibrium contact angle $\theta_e > 90°$ (a) in the sharp-interface model with interfacial tensions and (b) in the diffuse-interface model with bulk and wall potentials. (c) Definition of the interfacial normal direction n relative to the wall orientation.

A natural boundary condition of the phase-field is formulated on the solid wall [10], which respects the variation of $f_w(\chi)$, viz.

$$\lambda \frac{\partial \chi}{\partial n_{\partial\Omega}} + f_w'(\chi) = 0. \tag{2.10}$$

Herein $n_{\partial\Omega}$ is the wall normal direction, cp. Fig. 2.2c, and f_w' denotes the variation of f_w with respect to χ. It is to be pointed out that in the diffuse-interface context Eq. 2.10 describes an equilibrium contact angle, resembling Cox's equation [7]. Therefore, the effective contact angle is non-constant and may vary due to relaxation. The notation "equilibrium" refers to the thermodynamic equilibrium.

In the following a derivation of the wall energy density is shown, which is rarely seen in literature. Considering Fig. 2.2c, the interfacial normal direction n can be expressed in terms of the wall normal direction $n_{\partial\Omega}$ and the wall tangential direction $\tau_{\partial\Omega}$, viz.

$$n = -n_{\partial\Omega}\sin(\theta_e - 90°) + \tau_{\partial\Omega}\cos(\theta_e - 90°) = n_{\partial\Omega}\cos(\theta_e) + \tau_{\partial\Omega}\sin(\theta_e). \tag{2.11}$$

Using (2.5), (2.11) and equilibrium assumption for the interface, the surface normal derivative of the phase-field reads

$$\begin{aligned} \frac{\partial \chi(n)}{\partial n_{\partial\Omega}} &= \frac{\partial \chi}{\partial n}\,\frac{\partial n}{\partial n_{\partial\Omega}} = \frac{1}{\sqrt{2}\epsilon}\left(1-\chi^2\right)\cos\theta_e \\ \overset{\text{multiply (2.7)}}{\Rightarrow} \quad \lambda \frac{\partial \chi}{\partial n_{\partial\Omega}} &= \underbrace{\frac{3}{4}\sigma\left(1-\chi^2\right)\cos\theta_e}_{=:\,-f_w'(\chi)}. \end{aligned} \tag{2.12}$$

From (2.12) f_w' can be identified and intergrated with respect to the phase-field parameter, viz.

$$f_w(\chi) = -\sigma\cos\theta_e\frac{\chi(3-\chi^2)}{4} + \frac{\sigma_{sA}+\sigma_{sB}}{2} \tag{2.13}$$

In (2.13) the integration constant is set to satisfy Young's law in (2.8), i.e. $f_w(-1) = \sigma_{sA}$ and $f_w(1) = \sigma_{sB}$. In summary, (2.10) expresses a local equilibrium at the wall and hence is referred to as the equilibrium boundary condition of the phase-field. The expression for the equilibrium boundary condition is influenced by the special choice of the Ginzburg-Landau potential in (2.3).

2.1.4 Mobility Parameter

The capillary width ϵ and the mobility parameter κ are considered as the main parameters of a Cahn-Hilliard-type diffuse-interface model, as they are introduced throughout the literature. The mixing energy parameter λ can be viewed as a secondary parameter arising from the main ones, under further assumptions.

The capillary width controls the thickness of the interface and is often given as the dimensionless Cahn number $C_h = \epsilon / L_{\text{ref}}$, where L_{ref} is a macroscopic length scale, for example a droplet diameter. The Cahn number influences the accuracy, efficiency and stability of a simulation [16]. However, such an intuitive interpretation is more difficult for κ. In order to artificially thicken the interface, a scaling model is used, which governs the mobility of the diffuse interface for different capillary widths than the physical one and is important for a consistent formulation in the sharp-interface limit, $\epsilon \to 0$ [10]. Different scaling laws $\kappa \propto \epsilon^n$ for some n are considered in literature [7] to give a first attempt for a mobility parameter value. This present work uses the scaling law

$$\kappa = M \epsilon^2 \tag{2.14}$$

with a mobility coeffient M. By default one can use $M = 1\,\mathrm{m\,s\,kg^{-1}}$ as a first attempt but then one should pursue calibration by validation simulations. The corresponding dimensionless number for κ is the Péclet number $Pe = L_{\text{ref}} U_{\text{ref}} / (\kappa \Phi_{\text{ref}})$ with U_{ref} the characteristic velocity and Φ_{ref} the characteristic value of the chemical potential [9]. The scaling law (2.14) has been used by Ding et al. [17], who have studied small droplets in rapid droplet spreading, and also in [18, 19], where the phaseFieldFoam-solver has been utilised. Some authors also emphasize that the mobility can be a function of the phase-field parameter itself [13], which further complicates the Navier-Stokes-Cahn-Hilliard system.

2.1.5 Non-Equilibrium Boundary Condition

In this work dynamic droplet spreading is studied, hence non-equilibrium formulations are considered. However, most studies with the Cahn-Hilliard model have only used the equilibrium boundary formulation (2.10) and have neglected near-wall non-equilibrium effects, such as the finite relaxation of the interface, for example in rapid wetting processes [20]. A more generalised formulation of (2.10) has been introduced by Jacqmin [8] and studied by Yue et al. [20] and Qian et al. [21], viz.

$$\frac{\partial \chi}{\partial t} + \mathbf{u}_{\text{w}} \cdot \nabla \chi = -\Gamma_{\text{w}} \underbrace{\left(\lambda \frac{\partial \chi}{\partial n_{\partial\Omega}} + f_{\text{w}}'(\chi) \right)}_{=:\,\Phi_{\text{w}}}. \tag{2.15}$$

Herein, the equilibrium boundary condition is referred to as the wall chemical potential Φ_{w}, $\mathbf{u}_{\text{w}}$ is the velocity of the wall, i.e. the solid surface, and Γ_{w} is a new introduced rate constant denoted as the wall relaxation parameter. Taking the limit $\Gamma_{\text{w}} \to 0$ together with $\kappa \to 0$ produces the sharp-interface limit, where advection is dominant. On the opposite, taking $\Gamma_{\text{w}} \to \infty$ and $\kappa \to \infty$ produces the diffuse-interface limit where diffusion is dominant and the stress singularity of the moving contact line is resolved [21].

Like the mobility, discussed in the previous section, the wall relaxation parameter should be such as a phenomenological parameter within the diffuse-interface context. However, there are interpretations related to molecular-kinetic theories to get at least an initial, physically reasonable guess of its magnitude. However, the value of Γ_{w} highly depends on the fluid system and involved fluid-surface combinations. For example, Jacqmin has proposed $\Gamma_{\text{w}} \approx 10^9\,\mathrm{s\,kg^{-1}}$ in [8] and Carlson et al. have used

$\Gamma_w \approx 7 \times 10^7\,\mathrm{s\,kg^{-1}}$ in [22]. Similar to (2.14), the scaling law for the relaxation parameter is expressed in terms of a relaxation factor G with default value $G = 1$, viz.

$$\Gamma_w = G \cdot 10^9\,\mathrm{s\,kg^{-1}}. \tag{2.16}$$

2.2 Cahn-Hilliard-Navier-Stokes Diffuse-Interface Model

After introducing the basic properties of the Cahn-Hilliard-type phase-field formulation, the coupling to Navier-Stokes equations is focused. Starting with the generic structure followed by closure assumptions, the system of Navier-Stokes-Cahn-Hilliard partial differential equations and boundary conditions is shown.

2.2.1 Generic Structure

As a starting point the generic structure of so-called class I diffuse-interface models is used [23], but restricted to isothermal conditions. Therein, a Navier-Stokes system is described with mass transport of both constituents and the momentum equation. In addition, the transport equation of the phase-field parameter is included, also formulations for the boundary and initial conditions are prescribed.

In the following, a system of two incompressible, viscous fluids is assumed with immiscible bulk phases. Each fluid phase can be assigned to a volumetric phase fraction $\alpha_i \in [0,1]$. Mixing processes of this binary system are only allowed within a diffuse, capillary interface transition region. The volume averaged phase-field parameter is given by $\overline{c} = \alpha_2 - \alpha_1$. As the difference of the volumetric phase fractions, $\overline{c}$ shares the same values for the bulk phases, e.g. $\overline{c} \in [-1,1]$. A general volume averaged quantity $\overline{\phi}$ can be calculated by

$$\overline{\phi} := \frac{1-\overline{c}}{2}\,\overline{\phi}^1 + \frac{1+\overline{c}}{2}\,\overline{\phi}^2, \tag{2.17}$$

where the phasic average $\overline{\phi}^k$ is defined from the conditional volume-averaged quantitiy $\overline{\phi_k} := \int_V \phi_k \, d\mathbf{x}$ via $\alpha_k\,\overline{\phi}^k := \overline{\phi_k}$, see [24] for further details. The unclosed generic form for Cahn-Hilliard-type two-phase flow is

$$\nabla^\bullet \overline{\mathbf{u}} = 0, \tag{2.18a}$$

$$\partial_t(\overline{\rho}\,\overline{\mathbf{u}}) + \nabla^\bullet(\overline{\rho}\,\overline{\mathbf{u}} \otimes \overline{\mathbf{u}}) = \nabla^\bullet\langle\boldsymbol{\sigma}\rangle - \nabla^\bullet(\overline{\mathbf{u}} \otimes \langle\mathbf{J}\rangle) + \overline{\mathbf{b}} + \langle\mathbf{f}\rangle_c\,, \tag{2.18b}$$

$$\partial_t\,\overline{c} + \nabla^\bullet(\overline{c}\,\overline{\mathbf{u}}) = -\frac{2}{\overline{\rho}^2 - \overline{\rho}^1}\nabla^\bullet\langle\mathbf{J}\rangle\,. \tag{2.18c}$$

The bracket notation $\langle\cdot\rangle$ denotes quantities which need further constitutive assumptions for closure. Therein, $\langle\boldsymbol{\sigma}\rangle$ is the total stress tensor, $\overline{\mathbf{b}}$ is the body force vector, $\langle\mathbf{f}\rangle_c$ denotes the interfacial energy density and $\langle\mathbf{J}\rangle$ is the sum of the relative phasic mass fluxes with respect to $\overline{\mathbf{u}}$, see [24] for further details.

The solenoidal condition (2.18a) results from the summation of the phasic continuity equations if the mixing procedure is exact, i.e. $\sum_k \alpha_k = 1$, and bulk phases are incompressible. In addition, in a diffuse-interface model it is required that the sum of the volumetric phase fluxes needs to vanish, i.e. $\sum_k \langle\mathbf{J}\rangle_k / \overline{\rho}^k = 0$. Hence, the Cahn-Hilliard model for binary fluids states that during mixing processes the volume is conserved. The diffusive flow is related to the local composition of the binary mixture and not to the densities [9]. This behaviour makes diffuse-interface simulations comparable to solutions obtained by incompressible Navier-Stokes equations. It can also be shown [9] that for mixtures

with density contrast the global mass of either species is conserved when there is no diffuse volume flux through the boundaries, i.e. $\mathbf{n} \cdot \langle \mathbf{J} \rangle_k / \overline{\rho}^k = 0$. A solenoidal velocity field also means that it is decoupled from diffuse fluxes, which is important in cases when diffuse fluxes get significantly large, thus reducing numerical instability [9].

The second term on the r.h.s of the linear momentum equation (2.18b) modifies the total stress tensor $\langle \boldsymbol{\sigma} \rangle$ to be an objective tensor [13]. The Cahn-Hilliard equation (2.18c) is obtained by the difference of the phasic continuity equations.

2.2.2 Closure Assumptions

The constitutive equations are given by

$$\langle \boldsymbol{\sigma} \rangle = -\langle p \rangle \mathbf{I} + \langle \boldsymbol{\tau} \rangle, \tag{2.19a}$$

$$\langle \boldsymbol{\tau} \rangle = \langle \eta \rangle \left(\nabla \overline{\mathbf{u}} + \nabla \overline{\mathbf{u}}^{\mathsf{T}} \right), \tag{2.19b}$$

$$\langle \eta \rangle = \overline{\rho}\ \langle \nu \rangle = \overline{\rho}\ \overline{\nu}, \tag{2.19c}$$

$$\langle \mathbf{f} \rangle_c = -\lambda \nabla^{\bullet} \left(\nabla \overline{c} \otimes \nabla \overline{c} \right), \tag{2.19d}$$

$$\langle \mathbf{J} \rangle = \langle \mathbf{J}_1 \rangle + \langle \mathbf{J}_2 \rangle = -\left(\frac{\overline{\rho}^2 - \overline{\rho}^1}{2} \right) \kappa \nabla \Phi(\overline{c}). \tag{2.19e}$$

The fluids are described as Newtonian fluids, hence the total stress tensor (2.19a) is split in a volumetric part, introducing the pressure $\langle p \rangle$, and a deviatoric part (2.19b). The deviatoric part contains the dynamic viscosity $\langle \eta \rangle$, which, as a scalar field, also needs to be described further. A straight forward assumption is to simply use the linear average (2.17) for the dynamic or kinematic viscosity in (2.19c). Alternatively, an harmonic average can be used [25]. In both cases the numerical model has to ensure the boundedness of the phase-field parameter to prevent negative material parameters especially for strong variational fluids. Shifts from expected phase-field parameter values are a natural consequence in phase-field simulations, even tough $\overline{c}$ is conserved globally [26].

The interfacial energy density (2.19d) takes the form of a Korteweg-tensor and is part of the so-called Model-H by Hohenberg and Halperin [12]. Using tensor calculus rules, one can reformulate (2.19d) into $\Phi(\overline{c}) \nabla \overline{c}$ and a remaining gradient term. The latter will be absorbed by the pressure

$$\tilde{p} := p + \frac{\lambda}{\epsilon^2} \Psi(\overline{c}) + \frac{\lambda}{2} |\nabla \overline{c}|^2, \tag{2.20}$$

where the tilde notation will be neglected further on. The closure for the phase-field flux $\mathbf{J}$ in (2.18c) and (2.18b) is achieved by a Fick's equation for diffusion (2.19e) with the mobility κ as the diffusivity constant.

2.2.3 Governing Equations

Inserting the closure terms (2.19a) to (2.19e) into the generic forms (2.18a) to (2.18c) yields the final form of the Cahn-Hilliard-Navier-Stokes system to describe the diffuse-interface model of two incompressible, immiscible and isothermal Newtonian fluids:

$$\nabla^{\bullet}\,\overline{\mathbf{u}} = 0, \tag{2.21a}$$

$$\begin{aligned}\partial_t(\overline{\rho}\,\overline{\mathbf{u}}) + \nabla^{\bullet}(\overline{\rho}\,\overline{\mathbf{u}}\otimes\overline{\mathbf{u}}) = &-\nabla p_{\mathrm{d}} - \nabla\left(\overline{\rho}\,\mathbf{g}^{\bullet}\mathbf{x}\right) + \overline{\rho}\,\overline{\nu}\nabla^{\bullet}\left(\nabla\overline{\mathbf{u}} + \nabla\overline{\mathbf{u}}^{\mathsf{T}}\right)\\ &- \frac{\overline{\rho}^2 - \overline{\rho}^1}{2}\kappa\nabla^{\bullet}\left(\overline{\mathbf{u}}\otimes\nabla\Phi\right) + \Phi\nabla\overline{c}\,,\end{aligned} \tag{2.21b}$$

$$\partial_t\overline{c} + \nabla^{\bullet}(\overline{c}\,\overline{\mathbf{u}}) = \kappa\nabla^2\Phi, \tag{2.21c}$$

with

$$\Phi(\overline{c}\,) = \frac{\lambda}{\epsilon^2}[\,\overline{c}\,(\overline{c}\,-1)(\overline{c}\,+1)] - \lambda\nabla^2\overline{c}\,. \tag{2.21d}$$

In the linear momentum equation (2.21b) the pressure has been split up into its dynamic part p_{d}, while the static part has been absorbed into the buoyancy term, i.e. the gravitational field $\mathbf{g}$. The term $\Phi\nabla\overline{c}$ models interfacial forces in the diffuse-interface context, i.e. as a continuum force, and exhibits a key principle: Advection processes, disturbing the shape of the interface by lengthening, thickening or thinning, alter the total amount of free energy, which is countered by interfacial processes [7]. Alternatively, the formulation $\overline{c}\,\nabla\Phi$ can be used, which follows from reformulating the pressure $\hat{p} = p - \Phi\,\overline{c}\,$. However, the used model in this work has the advantage that its pressure formulation ensures the divergence-free velocity constraint and also makes less smoothness demands on the chemical potential [27].

2.2.4 Boundary Treatment / Initial Condition

The boundary condition for the phase-field model of two-phase Navier-Stokes flows is based on the works of Jacqmin [7], which can be derived as

$$\overline{\mathbf{u}}_{|\partial\Omega} = \mathbf{0}, \tag{2.22a}$$

$$\partial_n\Phi = 0, \tag{2.22b}$$

$$\partial_n\overline{c} = \frac{\sqrt{2}}{2}\frac{1}{\epsilon}\cos\theta_{\mathrm{e}}\left(1-\overline{c}^{\,2}\right), \tag{2.22c}$$

$$(\overline{\mathbf{u}}\,,\overline{c}\,)_{|t=0} = (\overline{\mathbf{u}}_0,\overline{c}_{\,0}). \tag{2.22d}$$

Equation 2.22a is the commonly used no-slip condition at the wall. This means that only the Cahn-Hilliard diffusion process can lead to a relative motion of the contact line. The phase-field equation needs to be described by two conditions (2.22b) and (2.22c). The first one is the no-flux condition, which means that the variation of the chemical potential in normal direction to the wall needs to vanish. The second one is the equilibrium boundary condition from (2.10) which models the interfacial fluid-solid boundaries with given equilibrium contact angle θ_{e}, as well as pure bulk regions where $\partial_n\overline{c} = 0$ applies. The homogeneous mixing energy parameter from (2.7) was inserted, since λ is both spatially and temporally constant. Alternatively, if (2.15) is used, a non-equilibrium or out-of-equilibrium boundary condition arises, viz.

$$\partial_n\overline{c} = \frac{\sqrt{2}}{2}\frac{1}{\epsilon}\cos\theta_{\mathrm{e}}\left(1-\overline{c}^{\,2}\right) - \frac{2\sqrt{2}}{3}\frac{1}{\sigma\epsilon\,\Gamma_{\mathrm{w}}}\left(\frac{\partial\,\overline{c}}{\partial\,t} + \mathbf{u}_{\mathrm{w}}\cdot\nabla\overline{c}\right). \tag{2.23}$$

2.3 Local Model for an Inhomogeneous Mixing Energy Parameter

So far, the current implemented theory of the phaseFieldFOAM-solver has been described. The first suggestion of a correction scheme for dynamic flow scenarios in the present diffuse-interface phase-field model has been from Yue et al. [1], who have simulated a drop deforming in a shear flow with Reynolds number $Re = L_{\text{ref}} U_{\text{ref}} / \nu = 0$. The computational results have showed a reduced drop deformation that has been described as a consequence of interfacial relaxation. Compared to Yue et al., the present work uses a droplet impact setup with $Re \approx 2000$, i.e. a water droplet with a diameter of about 2 mm and an initial velocity of about $1\,\mathrm{m\,s^{-1}}$. Hence, higher dynamics of the interface are expected. Thinking of the first contact of the droplet with the solid surface, the interface can not be treated homogeneously, as parts can fall while other parts impact simultaneously. All in all, a local model for the mixing energy parameter λ is advised.

This section first takes a look at Yue's global approach, then subsequently enhancing it with a localization procedure. The chemical potential and the natural boundary condition are deduced consistently from a variational argument with the Helmholtz free energy. Lastly, the right-hand side of the momentum equation is recalculated in order to see if additional terms arise.

2.3.1 Global Mixing Energy Parameter Model [1]

As Yue et al. [1] have pointed out, a fixed λ causes an elevated 'effective interfacial tension' that suppresses drop deformation . They have gained a more realistic interface behaviour by recalculating λ each time step according to the matching condition

$$\sigma S = \int_\Omega \left(\frac{\lambda}{2} |\nabla \bar{c}\,|^2 + \frac{\lambda}{\epsilon^2} \Psi(\bar{c}\,) \right) d\mathbf{x} \tag{2.24}$$

$$\Leftrightarrow \qquad \lambda_{\text{global}} := \frac{\sigma S}{\int_\Omega \left(\frac{1}{2} |\nabla \bar{c}\,|^2 + \frac{1}{\epsilon^2} \Psi(\bar{c}\,) \right) d\mathbf{x}} \tag{2.25}$$

where λ is the constant homogeneous mixing energy model, pulled out of the integral in (2.24), and S is the circumference of the interface for the iso-contour $\bar{c} = 0$. Eq. 2.25 can be referred to as the global mixing energy parameter model; global in the sense that it is spatially but not temporally constant. Yue et al. have also stated [1] that large-scale problems with complex interfaces, especially splitting interfaces, seem to be impractically described by the matching condition (2.24).

2.3.2 Localisation of Yue's Approach

The step-wise derivation of the local mixing energy parameter model is shown in the following, clearly demonstrating all model assumptions.

1.) Equilibrium vs. Non-Equilibrium Assumption

The assumption of a planar interface in equilibrium leads to a vanishing chemical potential, which means that both term on the right side in (2.4) are equal. Hence, the potential term in (2.6) can be expressed in terms of the phase-field gradient, which results in a formulation of σ that is often encountered in literature [7, 9]. Inserting (2.5) into (2.6) results in an homogeneous mixing energy parameter model. Thus, if both the potential and gradient part in (2.24) are maintained further on, the interface can be assumed to be in a non-equilibrium state.

2.) Diffuse-Interface Surface Integration

Yue's matching condition (2.24) is expressed as a volume integration over the whole domain Ω, which has resulted from an integration of (2.6) along the contour of $\bar{c} = 0$. The expansion from 1D to 3D in the diffuse-interface context is denoted here as diffuse-interface surface integration.

3.) Localisation Process

Localisation of (2.24) leads to

$$\sigma a^{\Sigma} = \lambda \left(\frac{|\nabla \bar{c}|^2}{2} + \frac{\Psi(\bar{c})}{\epsilon^2} \right) \tag{2.26}$$

where $a^{\Sigma} \equiv S_i / V_i$ is the (local) interfacial area per unit volume.

4.) Modeling the Interfacial Area per Unit Volume

To model a^{Σ}, the interface is assumed to be planar and in equilibrium state. Substituting (2.7) into (2.6) followed by expressing the potential term with the phase-field gradient and resorting leads to an expression for an inverse interfacial length scale [8, 28], viz.

$$\frac{2\sqrt{2}}{3} \frac{1}{\epsilon} = \int_{-\infty}^{\infty} \left(\frac{d\bar{c}}{dn} \right)^2 dn. \tag{2.27}$$

Applying diffuse-interface surface integration on (2.27) results in

$$\frac{2\sqrt{2}}{3} \frac{S}{\epsilon} = \int_{\Omega} |\nabla \bar{c}|^2 \, d\mathbf{x}. \tag{2.28}$$

After a localisation of (2.28) and resorting, the interfacial area per unit volume reads

$$a^{\Sigma} = \frac{3}{2\sqrt{2}} \epsilon |\nabla \bar{c}|^2. \tag{2.29}$$

5.) Local Mixing Energy Parameter Model

Inserting (2.29) into (2.26) and resorting leads to a local model of the mixing energy parameter, viz.

$$\lambda_{\text{local}} := \frac{3}{2\sqrt{2}} \sigma \epsilon \, \frac{|\nabla \bar{c}|^2}{\frac{|\nabla \bar{c}|^2}{2} + \frac{\Psi(\bar{c})}{\epsilon^2}}. \tag{2.30}$$

Eq. 2.30 is the main result of this section and, to the author's knowledge, has not been reported yet. λ_{local} is local in the sense that it is both spatially and temporally non-constant. The denominator in (2.30) allows that λ_{local} can potentially describe non-equilibrium processes. In equilibrium the fraction is equal to one, so that λ_{local} gets constant and the homogeneous model (2.7) is resembled. The fraction formulation however is indefinite in the pure bulk phases. Hence, λ_{local} should only be applied in the interfacial region, while in the pure bulk phases the homogeneous mixing energy parameter model (2.7) should be valid.

6.) Comparison with Literature

A main part of the derivation of (2.30) is the a^{Σ}-model, which is barely encountered in literature in the diffuse-interface context. Notable work has been done by Sun and Beckermann [28]. Their definition of the interfacial area per unit volume has an algebraic form, viz.

$$a^{\Sigma}_{\mathrm{SB}} = (1 - \overline{c}^{\,2})/(2\sqrt{2}\epsilon). \tag{2.31}$$

For a planar interface in equilibrium state, equating a^{Σ}_{SB} and $|\nabla \overline{c}\,|$ has the same equilibrium solution for the phase-field parameter (2.5) as the present model. With diffuse-interface surface integration it can be shown from [28], that the connection of a^{Σ}_{SB} and a^{Σ} is

$$a^{\Sigma} = 3\sqrt{2}\epsilon \left(a^{\Sigma}_{\mathrm{SB}}\right)^2. \tag{2.32}$$

Hence, inserting (2.31) into (2.32) would suggest that

$$\tilde{a}^{\Sigma} = \frac{3}{2\sqrt{2}}\epsilon\left(\frac{1}{2}\frac{\Psi(\overline{c}\,)}{\epsilon^2}\right), \tag{2.33}$$

which is similar to using the potential term $\Psi(\overline{c}\,)$ to simplify (2.6) and repeating the derivation to get (2.29). In fact, gradient and potential term are alike for vanishing chemical potential, so the question is, what supports the usage of (2.29) instead of (2.33)?

If the interfacial area per unit volume has an algebraic form like (2.33), then one assumes that $\tilde{a}^{\Sigma}$ is constant on an iso-contour line and varies only in interfacial direction. If $\overline{c}$ varies arbitrarily in a large-scale system, then a relation between the normal gradient and an algebraic model is generally not observed [28], hence the equilibrium assumption is violated. An algebraic expression of a^{Σ} would cancels out any influence of the macroscopic interface curvature. The polynomial formulation of a^{Σ}_{SB} has been declared as an attempt that appears physically meaningful; behaving like a Dirac delta function to pick out the interface. Other functional relationships have not been excluded. This supports the present usage of (2.29) instead of (2.33), since a^{Σ} does not suffer from any iso-contour line restrictions.

Additionally, an algebraic numerator formulation in (2.30) has the consequence that λ_{local} would increase if the interface is thickened (indicated only by a smaller gradient) and vice versa. From an energetic point-of-view a thickened interface means that the mixing energy is distributed over a larger domain, so locally an energy decrease must take place due to conservation of energy. Interfacial parts with lower energy should be represented by a decreased λ_{local}, as they contribute less to the cohesion of the interface; from mechanics known as tangential forces. This behavior can only be seen if (2.29) is used instead of (2.33).

2.3.3 Chemical Potential and Boundary Condition

In this section the variational process for the full expression of the total free energy will be excercised in order to shown consistency with fundamental work, see [29]. The derivation for a constant λ can also be found in [30]. Generally one has a functional F and a corresponding functional derivative (or first variation) δF:

$$F(\overline{c}\,) = \int_{\Omega} f\,[\mathbf{x}, \overline{c}\,(\mathbf{x}), \nabla \overline{c}\,(\mathbf{x})]\, d\mathbf{x}, \qquad \delta F(\overline{c}\,, \overline{c}^{\,\star}) = \int_{\Omega} \frac{\delta F}{\delta \overline{c}}(\mathbf{x})\ \overline{c}^{\,\star}(\mathbf{x})\, d\mathbf{x}$$

where $\overline{c}^{\,\star}(\mathbf{x})$ describes the change in $\overline{c}$. The term $\frac{\delta F}{\delta \overline{c}}$ is the functional (or variational) derivative of F and defined as the chemical potential Φ [29]. In the following, the explicit notation of spatial dependence will

be neglected, but it is pointed out that $\lambda = \lambda_{\text{local}} = \lambda(\mathbf{x})$ is considered. The total free energy including the boundary expression reads

$$\begin{aligned} F(\bar{c}) &= \int_\Omega f_{\text{mix}}(\bar{c})\, d\mathbf{x} + \int_{\partial\Omega} f_{\text{w}}(\bar{c})\, dS \\ &= \int_\Omega \left(\frac{\lambda}{\epsilon}\Psi(\bar{c}) + \frac{\lambda}{2}(\nabla\bar{c}\cdot\nabla\bar{c}) \right) d\mathbf{x} + \int_{\partial\Omega} f_{\text{w}}(\bar{c})\, dS, \end{aligned}$$

where

$$f_{\text{mix}}(\bar{c}) := \frac{\lambda}{\epsilon^2}\Psi(\bar{c}) + \frac{\lambda}{2}(\nabla\bar{c}\cdot\nabla\bar{c})$$

has been used. To gain the chemical potential and the natural boundary condition for $\bar{c}$ within this framework, the first variation of the total free energy is considered, viz.

$$\frac{\delta}{\delta\gamma}\Big(F[\bar{c} + \gamma\bar{c}^\star] \Big)\Big|_{\gamma=0} = 0,$$

where $\gamma\bar{c}^\star$ is the increment of the phase-field parameter. Hence,

$$\begin{aligned} 0 &= \frac{\delta}{\delta\gamma}\left(\int_\Omega \left[\frac{\lambda}{2}(\nabla\bar{c} + \gamma\nabla\bar{c}^\star)\cdot(\nabla\bar{c} + \gamma\nabla\bar{c}^\star) + \frac{\lambda}{\epsilon}\Psi(\bar{c} + \gamma\bar{c}^\star) \right] d\mathbf{x} + \int_{\partial\Omega} f_{\text{w}}(\bar{c} + \gamma\bar{c}^\star)\, dS \right)\Big|_{\gamma=0} \\ &= \int_\Omega \left[\lambda\nabla\bar{c}\cdot\nabla\bar{c}^\star + \lambda\gamma\nabla\bar{c}^\star\cdot\nabla\bar{c}^\star + \frac{\lambda}{\epsilon}\bar{c}^\star\Psi'(\bar{c} + \gamma\bar{c}^\star) \right] d\mathbf{x} + \int_{\partial\Omega} \bar{c}^\star f_{\text{w}}'(\bar{c} + \gamma\bar{c}^\star)\, dS \Big|_{\gamma=0} \\ &= \int_\Omega \left[\lambda\nabla\bar{c}\cdot\nabla\bar{c}^\star + \frac{\lambda}{\epsilon}\Psi'(\bar{c})\, \bar{c}^\star \right] d\mathbf{x} + \int_{\partial\Omega} f_{\text{w}}'(\bar{c})\, \bar{c}^\star\, dS. \end{aligned}$$

Now using $\nabla\bullet(\lambda\bar{c}^\star\nabla\bar{c}) = \lambda\bar{c}^\star\nabla^2\bar{c} + \bar{c}^\star\nabla\bar{c}\cdot\nabla\lambda + \lambda\nabla\bar{c}\cdot\nabla\bar{c}^\star$ and applying the divergence theorem, one obtains

$$0 = \int_\Omega \underbrace{\left[\frac{\lambda}{\epsilon}\Psi'(\bar{c}) - \lambda\nabla^2\bar{c} - \nabla\lambda\cdot\nabla\bar{c} \right]}_{=:\,\Phi(\bar{c},\nabla\bar{c})} \bar{c}^\star d\mathbf{x} + \int_{\partial\Omega} \underbrace{\left[\lambda\partial_n\bar{c} + f_{\text{w}}'(\bar{c}) \right]}_{\text{equilibrium b.c.}} \bar{c}^\star\, dS.$$

Since this is true for an arbitrary function $\bar{c}^\star$, in equilibrium the chemical potential vanishes. The formulation of the chemical potential is an extension of the standard formulation (2.21d). The equilibrium boundary condition has the same structure as (2.22c) but the value of λ has to be treated locally and can not be replaced in terms of σ and ϵ. If λ is explicitly a function of $\bar{c}$ and/or $\nabla\bar{c}$ then this variational procedure needs to be considered again in order to respect the boundary treatment.

2.3.4 Consequences for the Momentum Equation

The interfacial energy density $\langle \mathbf{f} \rangle_c$ in (2.19d) has resulted from the assumption of an homogeneous mixing energy parameter, when applying the divergence on a stress tensor $\langle \boldsymbol{\sigma}_c \rangle$. The stress tensor of the binary system can be gained by a variational procedure, also called virtual work principle, see Yue et al. [1]. Applying volume averaging and divergence on $\langle \boldsymbol{\sigma}_c \rangle$, the coupling term $\Phi \nabla \overline{c}$ needs to be reconstructed within the momentum equation. This procedure will be used to identify any changes when assuming that λ is inhomogeneous.

A general formulation of the local stress tensor [1, 13] is given by

$$\langle \boldsymbol{\sigma}_c \rangle = -\frac{\partial f_{\text{mix}}(\chi, \nabla\chi)}{\partial \nabla \chi} \otimes \nabla \chi, \tag{2.34}$$

with the partial derivative of the mixing energy density, defined by (2.2), with respect to the gradient of χ. Although λ is defined by (2.30), the dependence of χ and especially $\nabla\chi$ is not considered here, because this would lead to very complex expressions. Note that different models for $\langle \boldsymbol{\sigma}_c \rangle$ can be found in literature [31]; the usage depends on the phenomena behind the test cases, e.g. Marangoni effect. The divergence of the volume averaged tensor $\langle \bar{\boldsymbol{\sigma}}_c \rangle$ from (2.34) reads

$$\begin{aligned}
\nabla\bullet\langle \bar{\boldsymbol{\sigma}}_c \rangle &= \nabla\bullet[-\lambda(\nabla\overline{c} \otimes \nabla\overline{c})] \\
&= -\lambda\nabla\bullet(\nabla\overline{c} \otimes \nabla\overline{c}) - (\nabla\overline{c} \otimes \nabla\overline{c})\nabla\lambda \\
&= -\lambda\left[(\nabla \otimes \nabla\overline{c})\nabla\overline{c} + \nabla^2\overline{c}\,\nabla\overline{c}\right] - (\nabla\lambda \cdot \nabla\overline{c})\nabla\overline{c} \\
&= -\lambda\left[\frac{1}{2}\nabla|\nabla\overline{c}|^2 + \nabla^2\overline{c}\,\nabla\overline{c}\right] - (\nabla\lambda \cdot \nabla\overline{c})\nabla\overline{c} \underbrace{+\frac{\lambda}{\epsilon^2}\Psi'(\overline{c})\nabla\overline{c} - \frac{\lambda}{\epsilon^2}\nabla\Psi(\overline{c})}_{=\,\mathbf{0}} \\
&= \left[\frac{\lambda}{\epsilon^2}\Psi'(\overline{c}) - \lambda\nabla^2\overline{c} - \nabla\lambda \cdot \nabla\overline{c}\right]\nabla\overline{c} - \lambda\nabla\left(\frac{1}{\epsilon^2}\Psi(\overline{c}) + \frac{1}{2}|\nabla\overline{c}|^2\right) \\
&= \Phi\nabla\overline{c} \underbrace{- \nabla\left(\frac{\lambda}{\epsilon^2}\Psi(\overline{c}) + \frac{\lambda}{2}|\nabla\overline{c}|^2\right)}_{\text{absorbed into pressure}} + \underbrace{\left(\frac{1}{\epsilon^2}\Psi(\overline{c}) + \frac{1}{2}|\nabla\overline{c}|^2\right)\nabla\lambda}_{=:\,\tilde{s}_{\text{mix}}},
\end{aligned} \tag{2.35}$$

where, compared to the standard formulation, an additional source term $\tilde{s}_{\text{mix}}$ appears on the right-hand side of the momentum equation. In the last transformation step the pressure formulation (2.20) has been reproduced, which would have been more straight-forward for a constant λ. This not only allows for a comparison of the pressure with the standard model, but also for a vanishing $\tilde{s}_{\text{mix}}$ in cases of homogeneous λ-formulations or (bulk-)regions. Furthermore, a non-modified pressure formulation shows a pressure 'hump' inside the diffuse interface, which have been pointed out by Sun and Beckermann [28]. They have also showed that planar interfaces in equilibrium have identical far-field (e.g. bulk) pressures, while spherical interfaces have different far-field pressures. The pressure difference is of the order of $\sigma\tilde{\kappa}$, where $\tilde{\kappa} = 2/r$ is the curvature of a sphere of radius r.

In summary, the new local formulation of the mixing energy parameter shows additional terms in the chemical potential and momentum equation, that scales with $\nabla\lambda$. The standard λ-formulation is resembled in this new model when λ is homogeneous. Interfaces in equilibrium are still characterized by the standard homogeneous mixing energy parameter value $\lambda = 3\sigma\epsilon/(2\sqrt{2})$. No addition terms arise for the equilibrium boundary condition, but the instantaneous λ-value, i.e. λ_{global} or λ_{local}, has to be applied.

3 Numerical Method

In this chapter an overview of the improved numerical method of the PHASEFIELDFOAM-solver is given. The overall solution algorithm for the pressure-velocity coupling, namely the PIMPLE-algorithm, is not discussed in detail here. The main part of this chapter deals with the discretisation of the Cahn-Hilliard equation (2.21c), since it is a non-linear fourth-order partial differential equation. Special techniques to improve the implicitness of the discretisation of the non-linear chemical potential (2.21d) and the boundary term (2.22c) or (2.23) are presented. The coupled semi-discretised matrix system of the phase-field and chemical potential is introduced for each technique. This is a crucial improvement compared to the currently used segregated approach, where the chemical potential is calculated after the solution of the phase-field, and has been systematically tested in this work. The boundary conditions will be discretised with the same techniques to be consisted with the bulk-solution. Lastly, the numerical method to deal with the indefiniteness of the local mixing energy parameter model is shown.

3.1 Discretisation of the Cahn-Hilliard Equation

Non-linear terms in the Cahn-Hilliard equation (2.21c) and (2.21d) and the natural boundary condition (2.22c) or (2.23) originate from the mixing energy density (2.2) and the wall energy potential (2.13), more precisely the corresponding derivative with respect to the phase-field parameter. In the first section a general formalism of two selected linearisation schemes is shown, which are referred to as *stable* in terms of energy-stable and *optimal* in terms of the order in time of the phobic numerical dissipation [32]. When applying no linearisation, the corresponding method is called *none*. In subsequent sections, the linearisation schemes are applied on the mixing energy density and the wall energy potential.

3.1.1 Linearisation of Non-Linear Terms

The basic idea of two selected semi-implicit linear schemes are considered in the following, going back to the works of Eyre [33]. The first one is the *stable* scheme, which is first-order in time and derived by adding additional phobic numerical dissipation. An example of a 'phobic' term is the non-linear potential part of the Helmholtz free energy (2.2), while 'philic' is the gradient part. The implicit discretisation of an arbitrary non-linear potential P is split in a convex (or contractive) part P_c, that consists only of the new value $\overline{c}^{n+1}$, and a non-convex (or expansive) part P_e with the old values of $\overline{c}$ by introducing a parameter β, viz.

$$P\left(\overline{c}^{n+1}, \overline{c}^{n}\right) = P_c\left(\overline{c}^{n+1}, \beta\right) + P_e\left(\overline{c}^{n}, \beta\right). \tag{3.1}$$

The *stable* scheme follows from differentiation of (3.1) with respect to the phase-field parameter denoted by $(.)'$, viz.

$$P'\left(\overline{c}^{n+1}, \overline{c}^{n}\right) = P_c'\left(\overline{c}^{n+1}, \beta\right) + P_e'\left(\overline{c}^{n}, \beta\right). \tag{3.2}$$

The introduced parameter β is restricted by an energetical analysis so that the scheme is unconditionally, i.e. time-step independently energy-stable [32]:

$$\beta \geq \frac{3\left(\overline{c}^{n}\right)^2 - 1}{2}. \tag{3.3}$$

Since $\bar{c}^2 \leq 1$ should hold for the boundedness of the phase-field approach, the minimum value of the parameter is $\beta = 1$, which will be the default value in this work. This is equivalent to introducing the least possible numerical diffusion.

The *optimal* scheme is second-order in time and guarantees optimal dissipation compared to the *stable* method. Unfortunately this comes at the cost that the *optimal* scheme is only conditionally solvable, i.e. a restriction to the time-step arises [32]. The *optimal* scheme is derived from the Hermite quadrature formula

$$\int_a^b g(x)\,dx = (b-a)g(x) + \frac{1}{2}(b-a)^2 g'(x) + \cdots$$

with neglected higher-order terms, such that the non-linear potential can be written as

$$\begin{aligned} P\left(\bar{c}^{n+1}\right) - P\left(\bar{c}^{n}\right) &= \left(\bar{c}^{n+1} - \bar{c}^{n}\right) P'\left(\bar{c}^{n}\right) + \frac{1}{2}\left(\bar{c}^{n+1} - \bar{c}^{n}\right)^2 P''\left(\bar{c}^{n}\right) \\ P'\left(\bar{c}^{n+1}, \bar{c}^{n}\right) &= P'\left(\bar{c}^{n}\right) + \frac{1}{2}\left(\bar{c}^{n+1} - \bar{c}^{n}\right) P''\left(\bar{c}^{n}\right), \end{aligned} \tag{3.4}$$

where $(.)''$ denotes the second derivative with respect to the phase-field.

3.1.2 Cahn-Hilliard Equation

The Cahn-Hilliard system consists of two second-order non-linear PDE's for the phase-field variable (2.21c) and the chemical potential (2.21d). A semi-(time-)discretised form of each equation is achieved by treating the diffusive term implicit, while advective terms and non-linear potential parts remain explicit [1]. Both equations are assembled in a single block matrix for a simultaneous solution process. The solution system is represented by

$$\begin{cases} [\![\, \partial_t \bar{c}\,]\!] - [\![\, \kappa \nabla^2 \Phi\,]\!] & = -\nabla^{\bullet}(\mathbf{u}\,\bar{c})^n \\ [\![\, \lambda \nabla^2 \bar{c}\,]\!] + [\![\, \Phi\,]\!] & = \frac{\lambda^n}{\epsilon^2}\Psi'\left(\bar{c}^{n}\right) - \nabla\lambda^n \cdot \nabla\bar{c}^{n}, \end{cases} \tag{3.5}$$

where the double brackets notation $[\![.]\!]$ denotes an implicit finite-volume discretisation process. Eq. 3.5 is formulated without linearisation of non-linear terms (*none*-method). The mixing energy parameter λ, in the most general form λ_{local}, always stems from the previous time-step. The homogeneous and global λ-approaches are contained within the matrix system (3.5), since the additional term with $\nabla\lambda^n$ vanishes in this case. Improved implicitness, and therefore enhanced stability [1], can be achieved by linearisation of the Ginzburg-Landau potential. For the *stable* method the potential must be expanded exactly as

$$\begin{aligned} \Psi\left(\bar{c}\right) &= \frac{1}{4}\left(\bar{c}^4 - 2\bar{c}^2 + 1\right) = \frac{1}{4}\left(2\beta\,\bar{c}^2\right) + \frac{1}{4}\left(\bar{c}^4 - 2(\beta+1)\,\bar{c}^2 + 1\right) \\ \overset{(3.2)}{\Rightarrow}\ \Psi'\left(\bar{c}^{n+1}, \bar{c}^{n}\right) &= \beta\,\bar{c}^{n+1} + \Psi'\left(\bar{c}^{n}\right) - \beta\,\bar{c}^{n} \qquad \text{with} \quad \Psi'\left(\bar{c}^{n}\right) = \left(\bar{c}^{n}\right)^3 - \bar{c}^{n}, \end{aligned} \tag{3.6}$$

in order to be consistent with restriction (3.3). The *optimal* discretisation scheme follows from (3.4) as

$$\Psi'\left(\bar{c}^{n+1}, \bar{c}^{n}\right) = \frac{1}{2}\left[3\left(\bar{c}^{n}\right)^2 - 1\right]\bar{c}^{n+1} - \frac{1}{2}\left[\left(\bar{c}^{n}\right)^3 + \bar{c}^{n}\right]. \tag{3.7}$$

The implicit terms can now be transferred to the off-diagonal coupling entry of the chemical potential, viz.

$$\begin{cases} [\![\partial_t \bar{c}\,]\!] - [\![\kappa\nabla^2\Phi]\!] & = -\nabla^\bullet(\mathbf{u}\bar{c})^n \\ [\![\lambda\nabla^2\bar{c}\,]\!] - \frac{\lambda^n}{\epsilon^2}\beta[\![\bar{c}\,]\!] + [\![\Phi]\!] & = \frac{\lambda^n}{\epsilon^2}(\Psi'(\bar{c}^n) - \beta\bar{c}^n) - \nabla\lambda^n\cdot\nabla\bar{c}^n \end{cases} \tag{3.8}$$

and

$$\begin{cases} [\![\partial_t \bar{c}\,]\!] - [\![\kappa\nabla^2\Phi]\!] & = -\nabla^\bullet(\mathbf{u}\bar{c})^n \\ [\![\lambda\nabla^2\bar{c}\,]\!] - \frac{\lambda^n}{\epsilon^2}\frac{1}{2}\left(3(\bar{c}^n)^2 - 1\right)[\![\bar{c}\,]\!] + [\![\Phi]\!] & = -\frac{\lambda^n}{\epsilon^2}\frac{1}{2}\left((\bar{c}^n)^3 + \bar{c}^n\right) - \nabla\lambda^n\cdot\nabla\bar{c}^n, \end{cases} \tag{3.9}$$

where in (3.8) the *stable* scheme (3.6) and in (3.9) the *optimal* scheme (3.7) was used to discretize the Ginzburg-Landau potential.

3.1.3 Non-Linear Wall Potential

To complete the system of equations the boundary condition (2.22c) needs to be discretised using the same linearisation methods. The surface energy density f_w is therefore rewritten by introducing a non-linear wall potential $\Psi_\mathrm{w}(\bar{c})$ as

$$f_\mathrm{w}(\bar{c}) = \frac{\sigma\cos\theta_\mathrm{e}}{2}\underbrace{\left(\frac{\bar{c}^3 - 3\bar{c}}{2}\right)}_{\equiv\,\Psi_\mathrm{w}(\bar{c})} + \underbrace{\frac{\sigma_{sA}+\sigma_{sB}}{2}}_{\text{const.}}. \tag{3.10}$$

Form this general form, one can see the close relation to Young's law (2.8). The wall potential allows for a smooth transition over both pure phases A and B, since $\Psi_\mathrm{w} \in [-1,1]$ monotonously for $\bar{c} \in [-1,1]$. The *stable* linearisation is done in the following way to be consistent with restriction (3.3):

$$\begin{aligned} \Psi_\mathrm{w}(\bar{c}) &= \frac{1}{2}\left(\bar{c}^3 - 3\bar{c}\right) = \frac{3}{4}\beta\bar{c}^2 + \frac{1}{2}\left(\bar{c}^3 - 3\bar{c}\right) - \frac{3}{4}\beta\bar{c}^2 \\ \overset{(3.2)}{\Rightarrow}\ \Psi'_\mathrm{w}\left(\bar{c}^{n+1},\bar{c}^n\right) &= \frac{3}{2}\beta\bar{c}^{n+1} + \Phi'_\mathrm{w}(\bar{c}^n) - \frac{3}{2}\beta\bar{c}^n \qquad \text{with} \quad \Psi'_\mathrm{w}(\bar{c}^n) = \frac{3}{2}\left[(\bar{c}^n)^2 - 1\right]. \end{aligned} \tag{3.11}$$

The *optimal* scheme from (3.4) reads

$$\Psi'_\mathrm{w}\left(\bar{c}^{n+1},\bar{c}^n\right) = \frac{3}{2}\left(\bar{c}^n\bar{c}^{n+1} - 1\right). \tag{3.12}$$

By comparison, one can see that the *optimal* scheme is equivalent to choosing $\beta = \bar{c}^n$ in the *stable* approach. The restriction $\beta \geq 1$ needs to be fulfilled only on a global scope for an unconditionally stable scheme. Optimal dissipation however assumes a local value for β at the cost of time-step restrictions.

3.1.4 Non-Equilibrium Boundary Condition

The enhanced non-equilibrium boundary condition (2.15) can be written as

$$\lambda \partial_n \bar{c} + f_w'(\bar{c}) + \frac{1}{\Gamma_w} D_t \bar{c} = 0, \tag{3.13}$$

where D_t denotes the material derivative. To discretize (3.13) with improved implicitness a so-called 'convective' boundary condition is used, viz.

$$0 = \lambda \partial_n \bar{c} + \alpha(\bar{c}_b - \bar{c}_{ref}) \qquad \text{with} \quad \partial_n \bar{c} = (\bar{c}_b - \bar{c}_c)\delta. \tag{3.14}$$

Therein, $\bar{c}_b$ is the boundary value, $\bar{c}_c$ is the nearest cell-centered value, $\bar{c}_{ref}$ is a reference value, δ is the inverse distance between the cell-centers of the cells with values $\bar{c}_b$ and $\bar{c}_c$ and α is some parameter, denoted as transfer coefficient. $\bar{c}_{ref}$ will gather all terms of the previous time-step values of $\bar{c}$, while $\bar{c}_b$ is set to be the new value $\bar{c}^{n+1}$. The convective boundary condition is transferred to the more popular mixed-(or Robin-)type boundary condition

$$\bar{c}_b = w\bar{c}_{ref} + (1-w)(\bar{c}_c + g_{ref}\,\delta), \tag{3.15}$$

with a weighting function w and a reference gradient g_{ref}. If $\bar{c}_b \neq 0$ the convective formulation (3.14) can be represented by a derived boundary condition

$$\bar{c}_b = \underbrace{\frac{\alpha}{\alpha+\lambda\delta}}_{w}\bar{c}_{ref} + \underbrace{\frac{\lambda\delta}{\alpha+\lambda\delta}}_{1-w}\bar{c}_c, \tag{3.16}$$

which is based on the mixed formulation (3.15) with $g_{ref} \equiv 0$. If $\bar{c}_b = 0$, i.e. an explicit scheme is preferred, then (3.16) can not result from a reformulation of (3.14). In this case the reference gradient is used so that $g_{ref} \equiv \partial_n \bar{c}$ and the weighting function needs to fulfill $w = 1$. In order to use the derived boundary condition (3.16) the parameters α and $\bar{c}_{ref}$ need to be determined. This is done by equating the coefficients of (3.13) and (3.14) while setting $\bar{c}_b = \bar{c}^{n+1}$. Therefore, the discretisation of $f_w'(\bar{c})$ from previous sections is summarized in an advantageous representation, viz.

$$\text{stable :} \qquad f_w'\left(\bar{c}^{n+1}, \bar{c}^n\right) = \frac{3}{4}\sigma\cos\theta_e\,\beta\;\bar{c}^{n+1} - \frac{3}{4}\sigma\cos\theta_e\left[1 + \beta\,\bar{c}^n - (\bar{c}^n)^2\right], \tag{3.17}$$

$$\text{optimal :} \qquad f_w'\left(\bar{c}^{n+1}, \bar{c}^n\right) = \frac{3}{4}\sigma\cos\theta_e\,\bar{c}^n\,\bar{c}^{n+1} - \frac{3}{4}\sigma\cos\theta_e, \tag{3.18}$$

$$\text{none :} \qquad f_w'(\bar{c}^n) = -\frac{3}{4}\sigma\cos\theta_e\left[1 - (\bar{c}^n)^2\right]. \tag{3.19}$$

The material derivative of the phase-field $D_t\bar{c}$ is semi-(time-)discretised in the general form

$$\frac{\gamma_{n+1}}{\Delta t}\bar{c}^{n+1} - \frac{\gamma_n\bar{c}^n - \gamma_{n-1}\bar{c}^{n-1} - \Delta t\;\mathbf{u}_w\cdot\nabla\bar{c}^n}{\Delta t}. \tag{3.20}$$

with time-discretisation dependent parameters γ_i and the wall velocity $\mathbf{u}_w$. For example, the Euler implicit scheme reads $\{\gamma_{n+1}, \gamma_n, \gamma_{n-1}\} = \{1, 1, 0\}$. In Tab. 3.1 and Tab. 3.2 the α, $\bar{c}_{ref}$ and g_{ref} parameters of all linearisation methods are summarized for the non-equilibrium and equilibrium boundary condition.

Method	Transfer Coefficient α	Reference Value $\overline{c}_{\mathrm{ref}}$	Reference Gradient g_{ref}
stable	$\frac{3}{4}\sigma\cos\theta_{\mathrm{e}}\,\beta+\frac{\gamma_{n+1}}{\Gamma_{\mathrm{w}}\Delta t}$	$\frac{1}{\alpha}\left[\frac{3}{4}\sigma\cos\theta_{\mathrm{e}}\left(1+\beta\,\overline{c}^{\,n}-(\overline{c}^{\,n})^2\right)\right]$ $+\frac{1}{\alpha}\left[\frac{\gamma_n\overline{c}^{\,n}-\gamma_{n-1}\overline{c}^{\,n-1}-\Delta t\,\mathbf{u}_{\mathrm{w}}\cdot\nabla\overline{c}^{\,n}}{\Gamma_{\mathrm{w}}\Delta t}\right]$	0
optimal	$\frac{3}{4}\sigma\cos\theta_{\mathrm{e}}\,\overline{c}^{\,n}+\frac{\gamma_{n+1}}{\Gamma_{\mathrm{w}}\Delta t}$	$\frac{1}{\alpha}\left[\frac{3}{4}\sigma\cos\theta_{\mathrm{e}}+\frac{\gamma_n\overline{c}^{\,n}-\gamma_{n-1}\overline{c}^{\,n-1}-\Delta t\,\mathbf{u}_{\mathrm{w}}\cdot\nabla\overline{c}^{\,n}}{\Gamma_{\mathrm{w}}\Delta t}\right]$	0
none	0	0	$\frac{3}{4}\frac{\sigma}{\lambda}\cos\theta_{\mathrm{e}}\left(1-(\overline{c}^{\,n})^2\right)$ $+\frac{\gamma_n\overline{c}^{\,n}-\gamma_{n-1}\overline{c}^{\,n-1}-\Delta t\,\mathbf{u}_{\mathrm{w}}\cdot\nabla\overline{c}^{\,n}}{\lambda\Gamma_{\mathrm{w}}\Delta t}$

Table 3.1.: Parameters of the derived non-equilibrium boundary condition (*stable* and *optimal* linearisation method) and fixed-gradient non-equilibrium boundary condition (*none*).

Method	Transfer Coefficient α	Reference Value $\overline{c}_{\mathrm{ref}}$	Reference Gradient g_{ref}
stable	$\frac{3}{4}\sigma\cos\theta_{\mathrm{e}}\,\beta$	$\frac{1}{\beta}\left(1+\beta\,\overline{c}^{\,n}-(\overline{c}^{\,n})^2\right)$	0
optimal	$\frac{3}{4}\sigma\cos\theta_{\mathrm{e}}\,\overline{c}^{\,n}$	$\frac{1}{\overline{c}^{\,n}}$	0
none	0	0	$\frac{3}{4}\frac{\sigma}{\lambda}\cos\theta_{\mathrm{e}}\left(1-(\overline{c}^{\,n})^2\right)$

Table 3.2.: Parameters of the derived equilibrium boundary condition (*stable* and *optimal* linearisation method) and fixed-gradient equilibrium boundary condition (*none*).

3.2 Local Mixing Energy Parameter

The local mixing energy parameter model (2.30), derived in this work, has one disadvantage. The fraction notation will cause instabilities due to its indefiniteness when the gradient of the phase-field gets close to zero. To avoid numerical instabilities the local cell value λ_i is modified according to

$$\lambda_i = \frac{3}{2\sqrt{2}}\sigma\epsilon\,\frac{\max\left\{|\nabla\overline{c}|^2, s\right\}_i}{\max\left\{\frac{|\nabla\overline{c}|^2}{2}+\frac{\Psi(\overline{c})}{\epsilon^2}, s\right\}_i}, \tag{3.21}$$

where the maximum application secures that numerator and denominator never fall below a given value $s>0$. In the pure fluid phases the value of $|\nabla\overline{c}|^2$ would fall below s, which is prevented, so the homogeneous mixing energy parameter value is always applied in the bulk. The location of the transfer region of both λ-models is controlled solely by s, but also difficult to be set for different interface properties. To improve the handling of the local approach the following choice for the value s will be applied in (3.21):

$$s \equiv 2\frac{\Psi(\delta_c)}{\epsilon^2} \qquad \text{with} \qquad 0\leq\delta_c<1. \tag{3.22}$$

Eq. 3.22 introduces the correction width δ_c, which now has the interpretation as the phase-field value for which the mixing energy parameter models pass over. The analytic structure in (3.22) mimics the interfacial equilibrium case, i.e. when the terms in the denominator in (3.21) are equal. Additionally, (3.22) scales with ϵ, which potentially allows for a general usage of this approach.

4 Implementation Details

The implementation details for physical properties like the viscosity and density are shown. Consecutively, the implementation of the mixing energy correction procedure is explained giving also an overview of the main solution routine of phaseFieldFoam.

4.1 Viscosity Calculation

In this section the viscosity calculation procedure is shown, as it is implemented in the phaseFieldFoam-solver. Three different viscosity models are available, which determine the face-interpolated dynamic laminar viscosity μ_f. A non-trivial task is an appropriate choice of the viscosity models within the solver framework. In section 4.1.2 two implementation variants are shown. The first one used in chapter 5 and the second is studied additionally in chapter 6.

4.1.1 Viscosity Models

For a binary immiscible mixture with bulk dynamic laminar viscosities μ_A, μ_B, the face-interpolated dynamic laminar viscosity μ_f is calculated from a re-normalized phase-field order parameter on faces, i.e. $\hat{\bar{c}}_f \in [-1, 1]$. The latter enforcement is necessary to guarantee non-negative viscosities and densities because the phase-field parameter naturally shows shifts from its expected values in the bulk phases [26]. Several models for μ_f are selectable in phaseFieldFoam; the corresponding keywords are given in italic notation further on. The face-interpolated dynamic laminar viscosity for *arithmetic* (seriel), *harmonic* (parallel) and *blended* models are given by

$$\text{seriel / arithmetic}: \quad \mu_f^{(S)} = \frac{\hat{\bar{c}}_f + 1}{2}\,\mu_B - \frac{\hat{\bar{c}}_f - 1}{2}\,\mu_A, \tag{4.1}$$

$$\text{parallel / harmonic}: \quad \mu_f^{(P)} = \frac{\mu_A \mu_B}{\mu_f^{(S)}}, \tag{4.2}$$

$$\text{blended}: \quad \mu_f^{(B)} = \eta_f\,\mu_f^{(P)} + (1-\eta_f)\,\mu_f^{(S)}, \tag{4.3}$$

where η_f is the face viscosity weighting factor computed by $\eta_f = |\hat{\mathbf{n}}_{DI} \cdot \hat{\mathbf{n}}_{Sf}|$. Therein, $\hat{\mathbf{n}}_{DI}$ is the face unit interfacial normal vector determined using the face-interpolated gradient $(\nabla \bar{c})_f$ and $\hat{\mathbf{n}}_{Sf}$ is the standard face unit normal vector [34].

4.1.2 Viscosity Interpolations

The viscosity models need to be implemented, which has been done in two slightly different ways (versions) *V1* and *V2*, shown in listings 4.1 and 4.2. Differences between both viscosity interpolation methods occur in the velocity equation in file *UEqn.H* and the function to update ρ and μ (*updateProperties*) in the class *diffuseInterfaceProperties.C*.

From *V1* to *V2* the laplacian expression $\mu\nabla^{\bullet}\nabla\mathbf{u}$ in *UEqn.H* has changed, precisely the explicit treatment of the non-constant part of the dynamic viscosity given as a scalar product with $\mathbf{u}$. In *V1* the explicit treatment uses the face-interpolated value μ_f, while in *V2* the cell-centered value μ is used. The function *updateProperties(rho, mu)* is called after the solution of the phase-field parameter. In both versions the density is calculated the same but the dynamic viscosities vary. For version *V1* the dynamic viscosity μ is calculated directly from the bulk values μ_A and μ_B, while for version *V2* the dynamic viscosity is calculated via the kinematic viscosity, i.e. $\mu = \rho\,\nu$.

```
// UEqn.H
{
    // Calculate muf according to
    // viscosity model
    ...
    fvVectorMatrix UEqn
    (
        fvm::ddt(rho, U)
      + fvm::div(rhoPhi, U)
      - fvm::laplacian(muf, U)
      - (fvc::grad(U) & fvc::grad(muf))
      - phaseField.diffRhoPhi(U)
    );
    ...
}

// diffuseInterfaceProperty.C
updateProperties(
    volScalarField& rho,
    volScalarField& mu)
{
    // Re-normalize order parameter C
    ...
    rho == (C + scalar(1))/2.*rhob_
         - (C - scalar(1))/2.*rhoa_;
    mu == (C + scalar(1))/2.*mub
        - (C - scalar(1))/2.*mua;


}
```

Listing 4.1: Extractions of relevant code segments for viscosity interpolation method *V1*.

```
// UEqn.H
{
    // Calculate muf according to
    // viscosity model
    ...
    fvVectorMatrix UEqn
    (
        fvm::ddt(rho, U)
      + fvm::div(rhoPhi, U)
      - fvm::laplacian(muf, U)
      - (fvc::grad(U) & fvc::grad(mu))
      - phaseField.diffRhoPhi(U)
    );
    ...
}

// diffuseInterfaceProperty.C
updateProperties(
    volScalarField& rho,
    volScalarField& mu)
{
    // Re-normalize order parameter C
    ...
    rho == (C + scalar(1))/2.*rhob_
         - (C - scalar(1))/2.*rhoa_;
    mu == rho *
    (
        (C + scalar(1))/2.*nub_
      - (C - scalar(1))/2.*nua_
    );
}
```

Listing 4.2: Extractions of relevant code segments for viscosity interpolation method *V2*.

4.2 Implementation of the Correction Scheme

To make use of the new formulation of the mixing energy parameter it is necessary to understand the structure of the phaseFieldFOAM-solver, presented in appendix A. The basic design principle of phaseFieldFOAM follows a highly modular approach, which guarantees extensibility. For example the current Cahn-Hilliard and Allen-Cahn parameters (λ, γ) are encapsulated in the *capillaryInterface*-class, which is a concrete representative of the abstract *diffuseInterfaceType*-class. In this section the extension of the *capillaryInterface*-class is described in terms of a global and local approach for the mixing energy parameter. Subsequently, the new implementation of the λ-field within the solution process is shown.

4.2.1 Extension of the *capillaryInterface*-class

Following the current design principle, the task to calculate the mixing energy parameter λ is delegated to a new abstract base class *mixingEnergyCorrection*, see Fig. 4.1, so that future works can easily add new correction features. The concrete implementation of the global λ-model (2.25) and the local λ-model (2.30) is done within the respective derived classes *globalCorrection* and *localCorrection*. Endusers can switch between correction and non-correction via a modified subdictionary, see Listing 4.3, located in the */constant/phaseFieldProperties* dictionary. If no correction is desired, then choosing 'yes' for 'equilibrium'

leads to the homogeneous λ-model (2.7) denoted as *lambdaEqu*, no matter what correction method is given. Note that the viscosity model is also selected in the *capillaryInterface*-subdictionary. On a higher level, the *diffuseInterfaceProperty*-class is also modified. Similiar to the density and viscosity recalculation, an additional function *updateLambda(lambda)* is implemented. The function takes the mixing energy parameter field by reference and recalculates the latter with the chosen correction method.

Figure 4.1.: Restructured *capillaryInterface*-class extended by the abstract *mixingEnergyCorrection*-class which handles multiple λ-models.

```
capillaryInterface
{
    meanFaceViscosity "arithmetic"; // alternatives: "harmonic", "blended"

    mixingEnergyCorrection
    {
        // whether to apply correction
        equilibrium no;

        // mixing energy parameter model
        method  globalCorrection; // alternative: localCorrection

        localCorrection
        {
            // range: 0 <= corrWidth < 1
            // applying correction for cells with -corrWidth <= C <= corrWidth
            corrWidth   0.5;
        }
    }
}
```

Listing 4.3: Subdictionary in */constant/phaseFieldProperties* to control the mixing energy correction.

4.2.2 Modifications of the Solution Process

On the top-level of the PHASEFIELDFOAM-solver the mixing energy parameter is introduced as a cell-centered scalar field and registered as an *IOobject* in *createField.H*, see Listing 4.4. Similar to the chemical potential the boundary treatment is described with a zero-gradient. The *phaseField*-object, which is the main interface to handle the phase-field evolution, is extended by the reference of the mixing energy parameter. In Listing 4.5 the PIMPLE-algorithm of PHASEFIELDFOAM is shown, which is the outer *while*-loop. Calculations of the phase-field and mixing energy parameter are encapsulated in *phaseFieldEqn.H*. Further modifications to describe the local λ-model are related to the pressure-velocity coupling. In *pEqn.H* the recalculation of the volumetric flux ϕ is extended by the additional momentum source term $\tilde{s}_{\text{mix}}$ from derivation (2.35).

$\tilde{s}_{\text{mix}}$ is denoted as *mixSurfaceEnergyDensity* and calculated in the class *CahnHilliard.C*, see Listing 4.6. The *solve*-method is extended with the reference for λ and delegated to the abstract base class for different solution methods, currently *coupled* and *segregated*. In the class *coupled.C*, see Listing 4.7, the concrete solution method *pfFlux* is called. Therein, the block matrix system is subsequently created and solved. After retrieving the solution for the phase-field and chemical potential, the mixing energy parameter is recalculated by calling the function *updateLambda(lambda)*. If the number of solution cycles of the phase-field equation is increased (*nSubCycles* in Listing B.1), the mixing energy parameter is always recalculated consistently with the updated phase-field.

The classes to describe the contact angle, *equilibriumPhaseContactAngleFvPatchScalarField.C* and *outOfEquilibriumPhaseContactAngleFvPatchScalarField.C*, have been changed to use the mixing energy parameter field directly from the internal cell-centered values.

```
volScalarField lambda
(
    IOobject
    (
        "lambda",
        runTime.timeName(),
        mesh,
        IOobject::NO_READ,
        IOobject::AUTO_WRITE
    ),
    mesh,
    dimensioned<scalar>
    (
        "0",
        dimForce,
        (3*sigma*epsilon/
            (2*Foam::sqrt(2.))).value()
    ),
    "zeroGradient"
);
diffuseInterfaceEvolution
    phaseField(C, phi, Phi, lambda);
```

Listing 4.4: Top level initialisation of the mixing energy parameter in *createFields.H*.

```
int main(int argc, char *argv[])
{   ...
    #include "createFields.H"
    ...
    while (runTime.run())
    {   ...
        // --- SIMPLE loop
        while (pimple.loop())
        {
            #include "phaseFieldEqn.H"
            #include "UEqn.H"
            // --- PISO loop
            while (pimple.correct())
            {
                #include "pEqn.H"
            } ...
        } ...
    } ...
}
```

Listing 4.5: PIMPLE solution routine in *phaseFieldFoam.C*.

```
mixSurfaceEnergyDensity()
{   ...
    return
    (
        fvc::interpolate
        (
            diffuseInterfaceProp_
                .Psi(this->C())/sqr(epsilon)
          + 0.5*magSqr(fvc::grad(this->C()))
        )*fvc::snGrad(lambda())
    );
}
solve(
    volScalarField& C,
    volScalarField& Phi,
    volScalarField& lambda
)
{
    // Return mass flux
    return
    (
        CahnHilliardSolutionPtr_
            ->pfFlux(C, phi(), Phi, lambda)
    );
}
```

Listing 4.6: Additional momentum source term $\tilde{s}_{\text{mix}}$ and *solve*-method in *CahnHilliard.C*.

```
pfFlux(
    volScalarField& C,
    const surfaceScalarField& phi,
    volScalarField& Phi,
    volScalarField& lambda
)
{   ...
    // Create block matrix system
    ...
    // Solve block matrix system
    ...
    // Retrieve solution for C
    // and Phi
    ...
    // Re-calculate lambda
    diffuseInterfaceProp_
        .updateLambda(lambda);
    ...
}
```

Listing 4.7: Solution routine for the block matrix system in *coupled.C*.

5 Dynamic Droplet Spreading on a Super-Hydrophobic Substrate [2]

The simulation of a water droplet with initial velocity impacting on a planar and macroscopically smooth, super-hydrophobic surface is studied in this chapter. The impact behavior, i.e the motion of the contact line, can be described by the wetting factor $\beta_{\text{wet}} = D/D_0$, which is the ratio of the current droplet diameter D on the surface to the initial diameter D_0. For comparison, wetting is described in terms of a dimensionless time $\tau = tU_0/D_0$, where the simulation time t is linearly shifted if $U_0 > 0$. The setup and experimental data from Roisman et al. [2] is used for validation.

Additionally to the droplet spreading behavior, phase volume conservation is examined. For a given phase-field initialization the phase volume conservation error is defined as the relative variation of the total sum of phase-field-weighted cell volumes, viz.

$$e_V(\tau) \equiv \frac{\left(\sum_i \overline{c}_i V_i\right)_\tau - \left(\sum_i \overline{c}_i V_i\right)_{\tau=0}}{\left|\left(\sum_i \overline{c}_i V_i\right)_{\tau=0}\right|}. \tag{5.1}$$

A conservative method would ensure $e_V = 0$ at any time since the temporal derivative of the phase-field vanishes, viz.

$$\begin{aligned}\partial_t \int_\Omega \overline{c}\, dV \overset{V\neq V(t)}{=} \int_\Omega \partial_t \overline{c}\, dV &= \int_\Omega \nabla\bullet(\overline{c}\,\overline{\mathbf{u}})\, dV - \int_\Omega \kappa\nabla^2\Phi\, dV \\ &= \underbrace{\int_{\partial\Omega} \overline{c}\,\overline{\mathbf{u}}\cdot\mathbf{n}\; dS}_{\overline{\mathbf{u}}_{|\partial\Omega}\,=\,\mathbf{0}} - \underbrace{\int_{\partial\Omega} \kappa\nabla\Phi\cdot\mathbf{n}\; dS}_{\partial_n\Phi\,=\,0} = 0.\end{aligned}$$

The advantage of using (5.1) is that it respects any small shifts of the phase-field variable, i.e. slight variations of $\overline{c}_{\text{bulk}} = \pm 1$. Especially at high local curvature the surrounding droplet cells show $\overline{c} \gtrsim 1$. The shifts are an intrinsic consequence of the phase-field formulation and known in literature [26].

5.1 Case Setup

5.1.1 Physical Parameter

The fluid properties of the water droplet and the surrounding air and the corresponding surface tension are given in Tab. 5.1. Densities and kinematic viscosities are chosen to match the real physical situation for a constant temperature of 20 °C. The superhydrophobic surface, reported in [2], is made of coated glass with measured advancing and receding contact angles $\theta_{\text{adv}} = 156°$ and $\theta_{\text{rec}} = 134°$, respectively. It is assumed that the surface is macroscopically smooth without any microscopic structure. The equilibrium contact angle θ_{e} is calculated as the mean value of θ_{adv} and θ_{rec}, which gives $\theta_{\text{e}} = 145°$.

The initial droplet diameter is $D_0 = 2.04\,\text{mm}$ and the impact is perpendicular to the surface with initial velocity $U_0 = 0.83\,\text{m}\,\text{s}^{-1}$. In Fig. 5.1 the case setup is shown with parametrized dimensions and boundary

ρ_{air}	$1.2\,\text{kg}\,\text{m}^{-3}$
ρ_{water}	$998.2\,\text{kg}\,\text{m}^{-3}$
ν_{air}	$1.550 \times 10^{-5}\,\text{m}^2\,\text{s}^{-1}$
ν_{water}	$1.007 \times 10^{-6}\,\text{m}^2\,\text{s}^{-1}$
σ	$0.073\,\text{kg}\,\text{s}^{-2}$

Table 5.1.: Fluid properties of air and water at 20 °C.

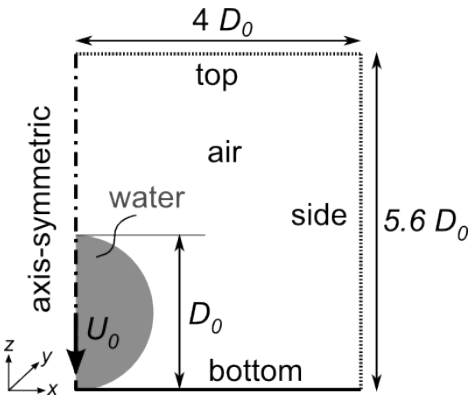

Figure 5.1.: Initial 2D-axis-symmetric case setup with chosen fixed domain dimensions and boundary notations.

notation. This work uses 2D-axis-symmetric simulations only to drastically reduce the computational cost. On the bottom wall, where the droplet is impacting, the *phaseContactAngle*-boundary condition for the phase-field parameter is applied, which can be either based on (3.1) or (3.2), respectively. All other boundaries guarantee zero-gradient of the phase-field and the chemical potential. The top and the side of the domain is modeled as an open boundary, which is a combination of a fixed zero-pressure and zero-gradient for the velocity. The wall-velocity of the bottom is zero and the pressure is modeled with vanishing flux.

5.1.2 Adaptive Mesh

The computational cost of solving the Navier-Stokes Cahn-Hilliard Systems highly depends on the number of variables, i.e. the number of control volumes. In phase-field simulations of binary immiscible fluids the resolution of the interface is a matter of particular interest in contrast to far-field bulk properties. An efficient way to focus on the interfacial resolution can be achieved by the use of the local dynamic adaptive mesh refinement technique, which has been implemented for 2D and 3D at the Technische Universität Darmstadt in FOAM-EXTEND 3.2. A coarse unstructured mesh, see Fig. 5.2, is refined with a chosen number of refinement levels N_{ref}. The whole domain is wedge-shaped with an opening angle of 5° and one cell in y-direction. Interface cells are determined and labeled by a certain criterion, here using the surface normal gradient with a threshold value of 0.1. Each labeled cell is successively split into four cells in this 2D-case until the target refinement level is reached (Fig. 5.3). At least two cells of one refinement level are maintained in each direction for a smoother cell size transition. During a simulation a refinement (or unrefinement) process is set to take place every 50th iteration. After this process the fluxes need to be recalculated, hence refinement intervals are chosen as large as possible. Since the adaptive mesh is frozen between refinement steps, a large interval can be achieved with an appropriate number of layers around the interface, here eight layers are chosen.

The resolution of the interface is expressed by the number of interfacial cells $N_{\text{I}} \approxeq 4D_0C_h/h$, where C_h is the Cahn number defined as the ratio of the capillary width and the initial droplet, i.e. $C_h = \epsilon/D_0$ and h denotes the mesh spacing of the finest level. In the x-z-plane the mesh with dimension $W \times H$ should have equal mesh spacing in each direction, thus

$$h = \frac{W\ D_0}{n_{\text{x}} 2^{N_{\text{ref}}}} \overset{!}{=} \frac{H\ D_0}{n_{\text{z}} 2^{N_{\text{ref}}}},$$

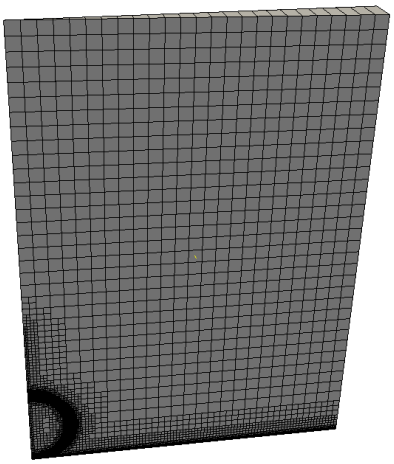

Figure 5.2.: Complete view of the quasi-2D initial unstructured mesh with 5 refinement levels.

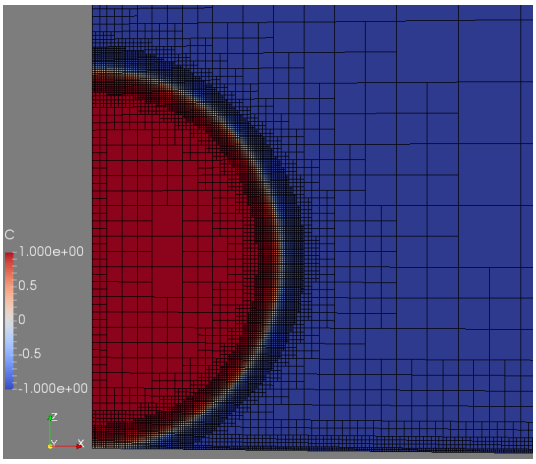

Figure 5.3.: Droplet cutout of the initial mesh with 5 refinements for $C_h = 0.01$ and 8 cells in interfacial direction.

where n_x and n_z are the number of control volumes (CVs) on the coarsest level in x- and z-direction. Note that OpenFOAM works with unstructured meshes, so hexahedral CVs neighboring refined hexahedral CVs are always polyhedra. The interfacial resolution of the adaptive mesh can be generally expressed by

$$N_I = 2^{2+N_{ref}} \frac{n_x}{W} C_h \stackrel{!}{=} 2^{2+N_{ref}} \frac{n_z}{H} C_h. \tag{5.2}$$

Additional to the refinement of the interface, the bottom is kept on the finest level as well. Along the axis a refined box with level $N_{ref} - 2$ and dimension $2D_0 \times 4\epsilon$ is applied to accelerate the refinement process. In Tab. 5.2 an overview of all employed meshes is given with corresponding reduction of total cell numbers compared to non-adaptive meshing. The domain size is optimized for $N_I = 8$ and $N_{ref} = 5$ at $C_h = 0.01$. This means that the high and low Cahn number can be set by $N_{ref} = 6$ or $N_{ref} = 4$ with the same interfacial resolution of eight cells. Besides $N_I = 8$ and $N_I = 16$ the number of interfacial cells is rounded down, compare (5.2). Running on a single processor on a standard laptop, the execution time for different interfacial resolution were about 4 hours for $N_I = 4$, 9 hours for $N_I = 8$ and 23 hours for $N_I = 16$.

N_I	n_x	n_z	N_{ref}	#CV initial	reduction in %
4	13	18	5	5841	-97.6
6	19	27	5	9489	-98.2
8	25	35	5	12797	-98.6
10	32	44	5	17074	-98.8
12	38	53	5	21031	-99.0
14	22	31	6	23932	-99.1
16	25	35	6	27377	-99.2

Table 5.2.: Setup of mesh properties for different interfacial resolutions with initial numbers of control volumes (#CV) and reduction of total cell amount compared to a corresponding non-adaptive mesh.

5.1.3 Solution Process

The solution procedure uses the PIMPLE-algorithm, see Listing 4.5. From preliminary investigation the PIMPLE-properties are set so that the velocity and pressure field after one refinement of the mesh are recalculated as fast as possible from the altered flux field. The number of outer corrections for the SIMPLE loop is set to three. Within a PIMPLE-iteration the phase-field is solved once. The pressure, like-wise within the PISO-algorithm, is solved once. The mesh refinement results in a higher mesh non-orthogonality, i.e. an angular deviation of face normal vectors and vectors connecting the cell centers. Such mesh induced errors are reduced by applying two non-orthogonal correction steps within a PISO-loop.

The time-step of the simulations is kept at $\Delta t = 0.5\,\mu s$, so that the Courant number $\mathrm{Co} = |\mathbf{u}| * \Delta t / h$ is of the order of 0.05. The choice of the time-step is influenced by the huge variance of cell volumes due to the mesh refinement. The ration of maximal over minimal cell volume varies from $V_{\max}/V_{\min} = 0.82 \times 10^6$ to $V_{\max}/V_{\min} = 12.85 \times 10^6$ for $N_\mathrm{I} = 4$ and $N_\mathrm{I} = 16$, respectively. The condition number of the solution matrix declines with increasing $V_{\max}/V_{\min}$. Additionally to usage of preconditioners, a smaller time-step improves the solution process. In App. B the complete solution and scheme dictionaries can be found.

5.2 Simulation Campaign

A summary of different models, methods and parameters within the phase-field context is given, which are available in the phaseFieldFoam-solver. Thereafter, the simulation campaign for the experiment by Roisman et al. [2] is described.

5.2.1 Parameter Space

The different models and methods are shown in Tab. 5.3. All simulations for the present test case are restricted to the viscosity interpolation method *V1* and viscosity model *harmonic*. During the present work, the *coupled* solution method was improved and the boundary conditions were consistently discretised with the different linearisation methods. New features are also the global and local mixing energy parameter models. In Tab. 5.4 the parameters of the phase-field model are presented with corresponding values applied in this work. So far, C_h, N_I and M have been the standard phase-field parameters in simulations, the latter often described by the Péclet number. Additionally, the relaxation parameter G is used for the non-equilibrium boundary condition and the correction width δ_c needs to be specified for the local mixing energy parameter model.

Model / Method	Representation
solution procedure of the Cahn-Hilliard system	*coupled* (3.5), [*segregated*]
linearisation method of non-linear potentials	*stable* (3.2), *optimal* (3.4), *none*
boundary condition of $\bar{c}$ on solid surfaces	equilibrium (2.22c), non-equilibrium (2.23)
mixing energy parameter	homogeneous (2.7), global (2.25), local (2.30)
viscosity interpolation method	*V1* (Listing 4.1), [*V2*]
viscosity model	*harmonic* (4.2), [*arithmetic*, *blended*]

Table 5.3.: Overview of different models and methods applied in the phase-field model for the present test case. Additionally available yet unused models are shown in square brackets.

Parameter	Description	Values
C_h	Cahn number defined by $C_h = \frac{\epsilon}{D_0}$	{ 0.005, 0.01, 0.02 }
N_I	number of control volumes in interfacial direction / interfacial resolution	{ 4, 6, 8, 10, 12, 14, 16 }
M	mobility factor for scaling law $\kappa = M\epsilon^2$	{ 1/4, 1/2, 1, 2, 4, 8, 16, 32 }
G	relaxation factor for scaling law $\Gamma_\mathrm{w} = G \cdot 10^9\,\mathrm{s\,kg^{-1}}$	{ 1/16, 1/8, 1/4, 1/2, 1 }
δ_c	correction width, local λ-model applied for cells with $\overline{c}_{\mathrm{corr}} = 0 \pm \delta_c$	{ 0.5, 0.6, 0.7, 0.8 }

Table 5.4.: Overview of different parameters of the phase-field model with brief description and studied values for the present test case.

5.2.2 Parameter Study

Since the parameter space is huge an appropriate sequence of simulations is needed. In the course of investigating the wetting factor evolution, the PHASEFIELDFOAM-solver is tested with the *coupled* solution procedure for the first time. There are three different linearisation methods available; it is decided to use the *stable*-method as default. In addition, the equilibrium boundary condition for the phase-field is used, of course linearised with the *stable*-method again. The stable-method is expected to be superior to non-linearisation but also more independent of a chosen time-step. If not declared otherwise, the homogeneous mixing energy parameter model is applied.

In section 5.3.1 the mobility is varied while having a moderate Cahn number and moderate to high interfacial resolution. From comparison with experimental data, a fitting mobility factor is determined and used further in subsequent studies. The grid convergence is subject to section 5.3.2, where lower and higher numbers of interfacial cells are applied. This is followed by a variation of the interfacial thickness in section 5.3.3, where a lower and higher Cahn number is tested.

So far the standard, often encountered parameters of a phase-field have been tested and the mobility has been set. Since the case in [2] is way more dynamic than letting a droplet fall without initial velocity, it is interesting to see the influence of the non-equilibrium boundary condition with relaxation in section 5.3.4. Additionally, a comparison of the different solution methods is given in section 5.3.5.

The main idea to deal with dynamic, out-of-equilibrium behavior of the diffuse-interface is to apply a new model for the mixing energy parameter. In section 5.3.6 the global λ-model by Yue is tested. Subsequently in section 5.3.7 the local λ-model is used, which has been developed in this work. Global and local model are directly compared with the homogeneous model using the same phase-field model-parameters. The local model is tested with respect to the correction width, the latter local-specific parameter deals with indefiniteness of the model.

Besides the wetting factor, additional information is gained from the droplet shape analysis in section 5.3.8. Therein, a selection of previous model is chosen and compared at two selected time-steps.

5.3 Simulation Results

5.3.1 Variation of Mobility

The first simulations show the basic phenomena regarding the whole wetting process, which will be representative for all subsequent sections. The variation of the mobility is done for the solution procedure *coupled* together with the linearisation method *stable* (3.8) and equilibrium boundary condition (3.2). The Cahn number and interfacial resolution are fixed to $C_h = 0.01$ and $N_\mathrm{I} = 8$.

On the left hand side of Fig. 5.4 the temporal evolution of wetting factors for different mobility factors are shown together with experimental data. Different wetting stages can be seen, which all simulations have in common. From initialization to $\tau \approx D_0/U_0 = 1$ the spreading phase is observed, where the droplet is wetting the surface until a maximal wetting factor is reached, here about $\beta_{\mathrm{wet,max}} \approx 1.56$. This is followed by a receding phase of the droplet. Finally at about $\tau \approx 4$ a total re-bounce is observed, where the droplet is no more in contact with the surface. The receding phase last about $2.5-3$-times as long as the spreading phase.

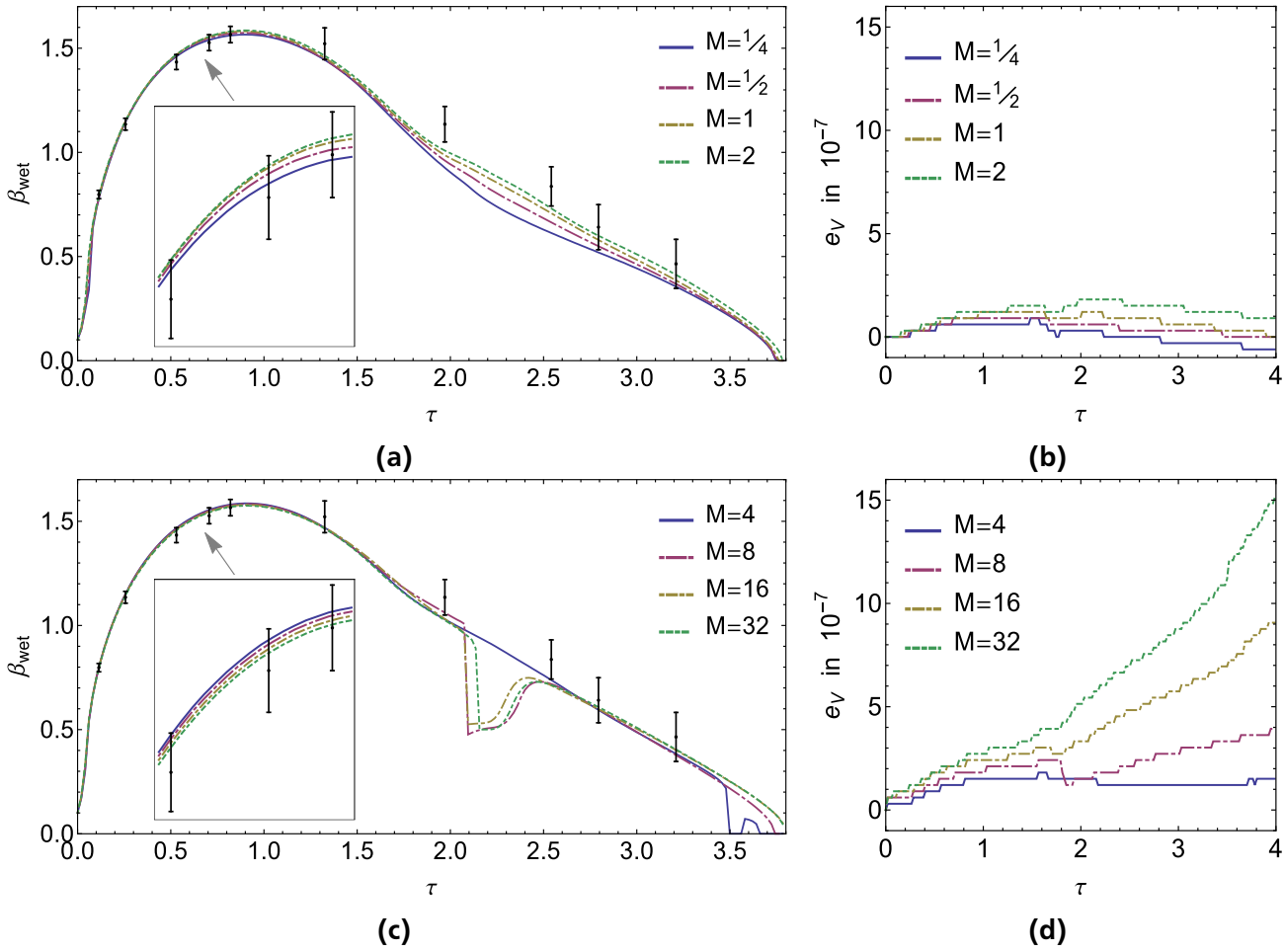

Figure 5.4.: Wetting factors (a,c) and corresponding phase volume conservation error (b,d) for different mobilities. Common simulation parameters are $C_h = 0.01$, $N_\mathrm{I} = 8$, solution with *coupled-stable* and equilibrium boundary condition.

In Fig. 5.5 the simulated shape evolution of the water droplet with $M = 1$ is shown. After initialization the droplet starts forming a rim close at the contact line. No bubble entrapment is observed on the bottom. As the rim grows at the outskirt area more and more water volume is gathered within it. This results in the formation of a thin film (lamella) around the central axis between $\tau = 1$ and $\tau = 1.5$.

The lamella does not break up, so no dry-out on the central axis is observed. In the receding phase the droplet forms a pyramidal structure and is lastly re-bounced vertically from the bottom in a jet-like structure.

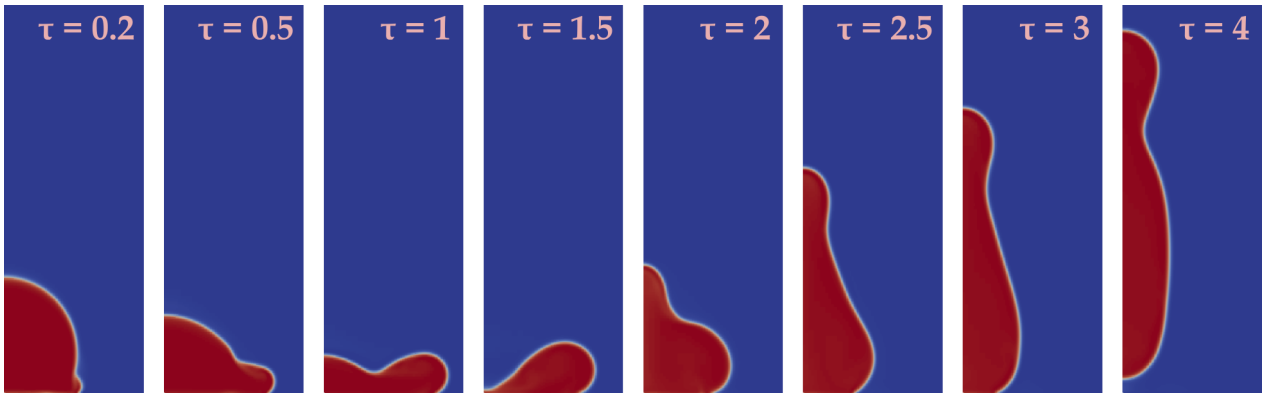

Figure 5.5.: Shape evolution of the water droplet in air for $M = 1$, $C_h = 0.01$, $N_\mathrm{I} = 8$, solution with *coupled-stable* and equilibrium boundary condition.

For all simulated mobility factors there is very good agreement of β_{wet} with the experimental data in the spreading phase. The mobility shows only little influence on the temporal spreading evolution on a macroscopic view until $\tau = 1.5$. The insets in Fig. 5.4a and 5.4c reveal that with about $M = 2$ or $M = 4$ the droplet spreading velocity, i.e. the velocity of the moving contact line, has a maximum value. In the receding phase from $\tau = 1.5$ to $\tau = 3.5$ the simulations show different behavior, but are still in agreement with the last experimental data point. Reducing the mobility, Fig. 5.4a, leads to a faster receding of the droplet and the variance to the experimental data increases. The experimental data predict a linear behavior during the receding phase. The best fitting trend is observed for $M = 2$ and $M = 4$. Increasing the mobility further, Fig. 5.4c, shows a characteristic break-in for $M \geq 8$ around $\tau \approx 2.2$. The reason for that is a complete dry-out of the lamella and the corresponding formation of a torus-shaped droplet, shown in Fig. 5.6 with simulation $M = 16$ for example. When the torus is retracting towards the axis a bubble entrapment is observed. The bubble is displaced by the water phase and moves towards the contact line. At about $\tau = 2.05$ the bubble is released to the surrounding air and the contact line is snapping back so that the wetting factor is again in agreement with the experimental trend.

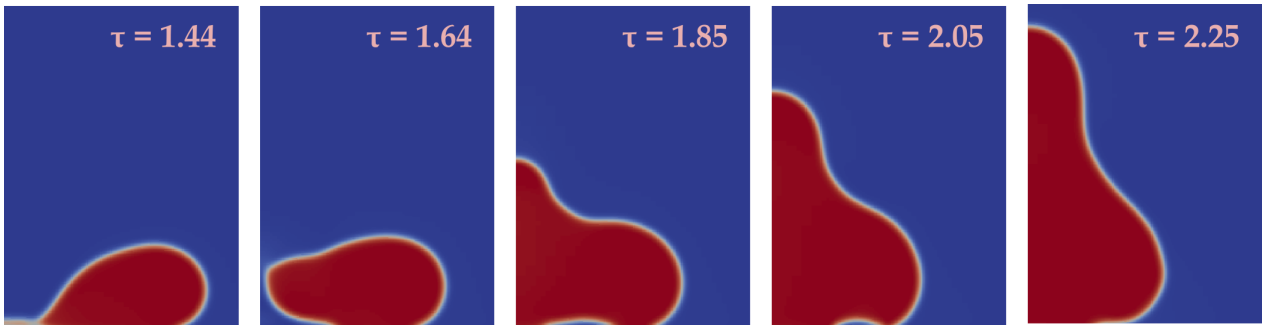

Figure 5.6.: Central dry-out and torus formation for $M = 16$, $C_h = 0.01$, $N_\mathrm{I} = 8$, solution with *coupled-stable* and equilibrium boundary condition.

Phase volume conservation errors for different mobility factors are shown in Fig. 5.4b and 5.4d. None of the simulations are accurate enough to ensure conservation up to the 7th digit. However, reducing the mobility leads to smaller variances. Looking at $M = 0.25$ the spreading phase shows a slight artificial increase of the water phase ($e_V > 0$), while in the receding phase the air phase increases ($e_V < 0$).

Until $M = 4$ the phase volume conservation error is limited within the simulated range. Increasing the mobility further a divergent behavior is observed.

Concluding, it has been shown that using the homogeneous mixing energy parameter model the mobility factor $M = 2$ is in good agreement with the experiment in both the spreading and receding phase, while ensuring phase volume conservation.

5.3.2 Variation of Interfacial Resolution

The next step is to look at the variation of interfacial resolution, i.e. the number of interfacial cells, for given $C_h = 0.01$ and $M = 2$. The choice of $N_\mathrm{I} = 8$ as the default resolution in the previous section is based on literature survey and expected as an appropriate, not to say high resolution.

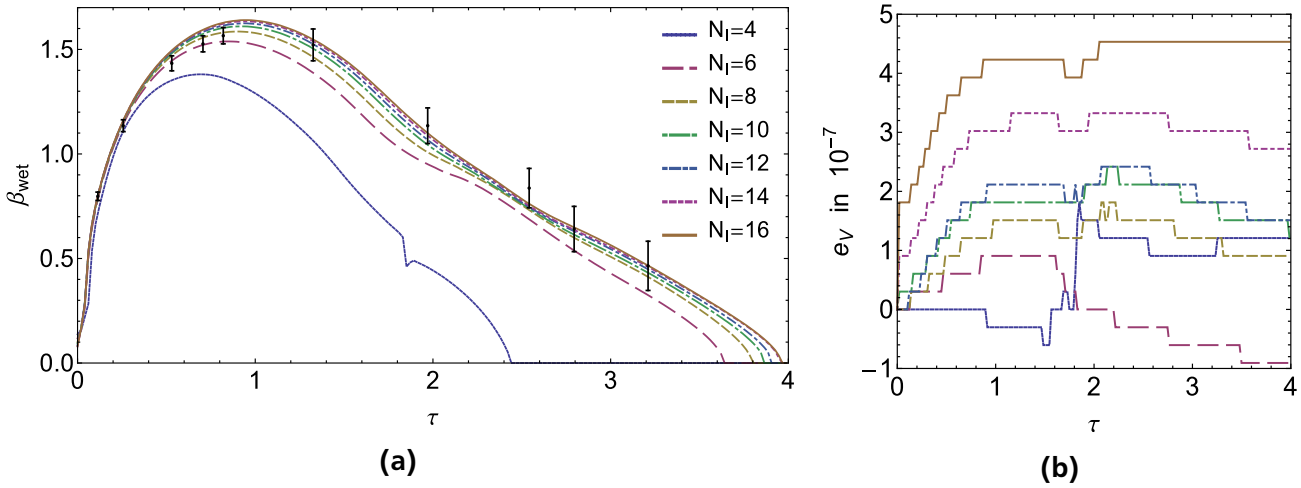

Figure 5.7.: Wetting factors (a) and corresponding phase volume conservation error (b) for different numbers of interfacial cells. Common simulation parameters are $C_h = 0.01$, $M = 2$, solution with *coupled-stable* and equilibrium boundary condition.

In Fig. 5.7a the number of interfacial cells was varied from $N_\mathrm{I} = 4$ to $N_\mathrm{I} = 16$. If only $N_\mathrm{I} = 4$ interfacial cells are used the simulation is clearly under-resolved as the wetting factor deviates even in the spreading phase. Comparing $N_\mathrm{I} = 6$ and $N_\mathrm{I} = 8$ the spreading phases are both in agreement with experimental data but $N_\mathrm{I} = 6$ underestimates the wetting factor in the receding phase. The overall influence of increasing the interfacial resolution is that it accelerates the contact line velocity in the spreading phase so that a higher $\beta_{\mathrm{wet,max}}$ value is reached. All simulations show a hierarchical behavior without intersection and for $N_\mathrm{I} \geq 8$ a contraction around $\tau \approx 2.5$. In the contraction zone the simulations are most likely synchronized compared to initialization, so the variance from different $\beta_{\mathrm{wet,max}}$ was compensated. After the contraction zone the wetting factors start diverging again with faster droplet retraction and total re-bounce for lower N_I. The variance from $N_\mathrm{I} = 14$ to $N_\mathrm{I} = 16$ is very small, so for a converged solution $N_\mathrm{I} = 14$ is necessary. Comparing $N_\mathrm{I} = 8$ and $N_\mathrm{I} = 14$ the spreading phase is better described by $N_\mathrm{I} = 8$ and slightly overestimated by $N_\mathrm{I} = 14$. During the receding phase $N_\mathrm{I} = 14$ is in better agreement with experiment passing through all confidence intervals. After the contraction zone the experimental data is again well matched for $N_\mathrm{I} = 8$. Regarding the phase volume conservation error, Fig. 5.7b, a higher interfacial resolution leads to a higher variance of e_V from zero. The variance is more than twice as large for $N_\mathrm{I} = 16$ as for $N_\mathrm{I} = 8$.

In conclusion, simulating dynamic droplet spreading with an interfacial resolution of $N_\mathrm{I} = 8$ does not guarantee a fully converged simulation although the wetting factor has been showed to be in good agreement with the experiment. Less dynamic test cases calculated with PHASEFIELDFOAM and 4−8 interfacial cells have been studied in [18] showing a good compromise between accuracy and computational cost.

5.3.3 Variation of Interfacial Thickness

With the Cahn number C_h one controls the capillary width ϵ and therefore the effective interfacial thickness. The latter limits the role of the diffuse-interface properties like the mobility. In this section the mobility law $\kappa = M\epsilon^2$ is investigated for a fixed interfacial resolution $N_\mathrm{I} = 8$. The Cahn number is controlled by the number of refinements, for example $N_\mathrm{ref} = 6$ for $C_h = 0.005$.

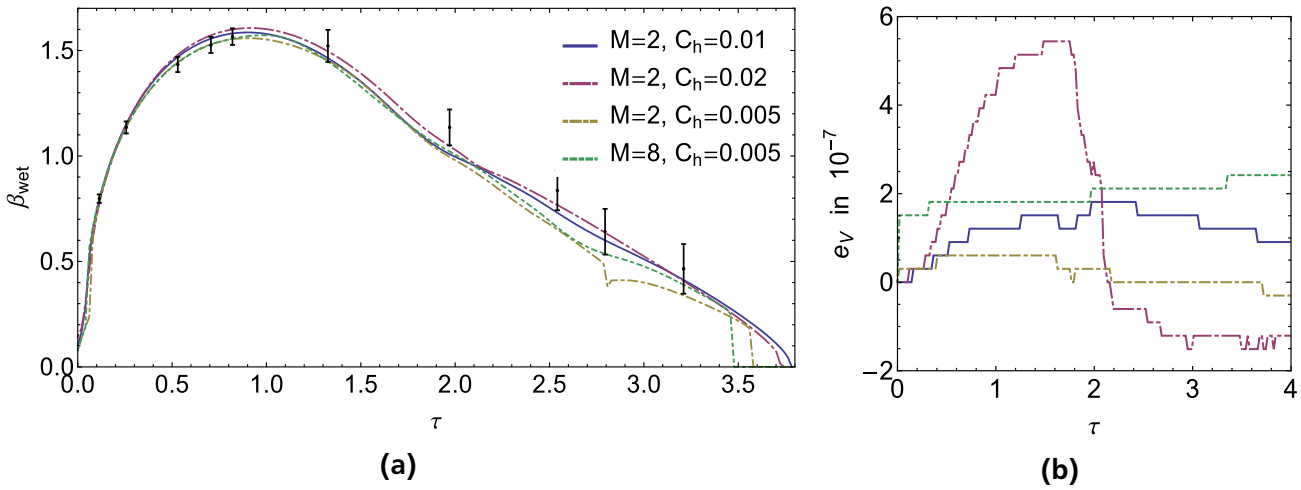

Figure 5.8.: Wetting factors (a) and corresponding phase volume conservation error (b) for different Cahn numbers and mobilities. Common simulation parameters are $N_\mathrm{I} = 8$, solution with *coupled-stable* and equilibrium boundary condition.

In Fig. 5.8a three different Cahn numbers are shown with $M = 2$, the latter choice based from previous sections. All C_h are in good agreement with experimental data in the spreading phase. The maximum wetting factor is slightly lower for $C_h = 0.005$ and higher for $C_h = 0.02$ compared to the default value $C_h = 0.01$ from previous sections. From $\tau \approx 1.3$ to $\tau \approx 1.9$ the wetting factors for $C_h = 0.01$ and $C_h = 0.005$ lie one above the other until the droplet recedes faster for lower C_h. The simulations with medium and high C_h are in better agreement with the experiment for the later receding phase. The small break-in at $\tau = 2.8$ for $C_h = 0.005$ results from a small bubble entrapment about four cell height ($\approx 20\,\mu$m). The minimum height of the lamella is of the same height and close to break-up but no torus is formed. The phase volume conservation error, Fig. 5.8b, shows a higher variance of the high Cahn number. The low Cahn number has the lowest observed variance of e_V from zero so far.

Another simulation was done for $M = 8$ with low Cahn number so that the same mobility is applied compared to $M = 2$ with $C_h = 0.01$. This run shows again a variance from experiment at $\tau = 2.5$. The total re-bounce of the droplet occurs even faster in this setup. The phase volume conservation error gets worse for higher mobilities with fixed $C_h = 0.005$, just as seen in previous sections for $C_h = 0.01$.

Concluding, it has been shown that reducing the interfacial thickness does not necessarily improve the conformity of phase-field simulation and experiment in dynamic cases.

5.3.4 Non-Equilibrium Boundary Condition

The non-equilibrium boundary condition is applied in this section, where the wall relaxation parameter is expressed by $\Gamma_\mathrm{w} = G \cdot 10^9\,\mathrm{s\,kg^{-1}}$ with a relaxation factor G. The resolution is fixed to $C_h = 0.01$ and $N_\mathrm{I} = 8$ and the mobility parameter is $M = 2$.

In Fig. 5.9 the wetting factors for decreasing relaxation factors are shown. For comparison, $G \to \infty$ belongs to the simulation with equilibrium boundary condition. Using a wall relaxation parameter of $\Gamma_\mathrm{w} = 10^9\,\mathrm{s\,kg^{-1}}$ is very close to the equilibrium case. The main influence of reducing G is seen in the

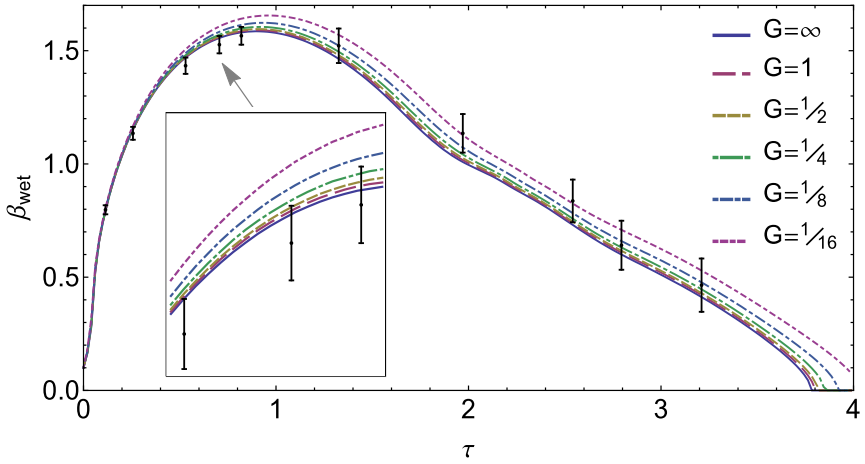

Figure 5.9.: Wetting factors for different relaxation factors. Common simulation parameters are $C_h = 0.01$, $N_I = 8$, $M = 2$, solution with *coupled-stable* and non-equilibrium boundary condition.

spreading phase. The contact line moves faster and the maximum wetting factor is higher. If $G < 0.25$ the wetting factor is overestimated during the spreading phase. The variance of the wetting factors around $\beta_{wet,max}$ for different G is approximately maintained during the receding phase. The non-equilibrium boundary condition shows less influence on the retraction behavior of the droplet. The phase volume conservation error of all simulations is limited by $e_V < 2 \times 10^{-7}$ in agreement with Fig. 5.8b for $M = 2$.

In conclusion, it is not necessary to apply the non-equilibrium boundary condition for the present test case. The non-equilibrium boundary condition affects only the spreading phase and leads to a faster wetting of the surface. However the spreading phase is already well described when the equilibrium boundary condition is used.

5.3.5 Comparison of Solution Methods

The default solution method so far was the *coupled* approach with *stable* linearisation of the (wall) chemical potential. In this section the *optimal* and *none* linearisation method are tested with different time-steps $\Delta t \leq 0.5\,\mu s$, $C_h = 0.01$, $N_I = 8$ and $M = 2$.

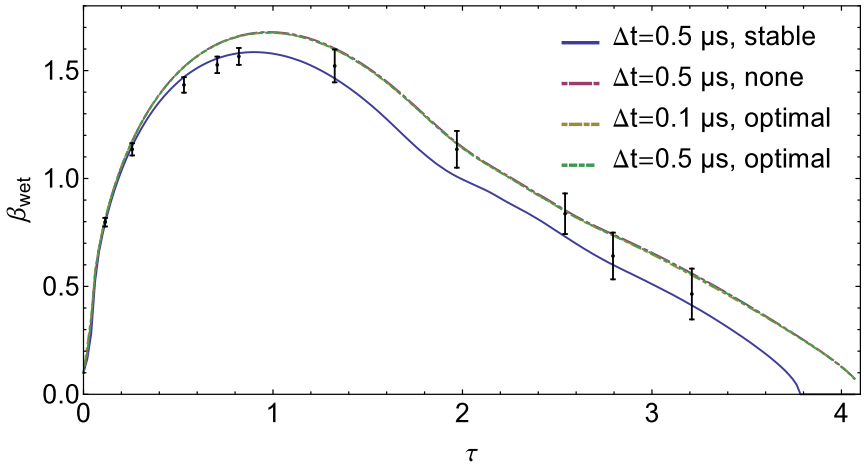

Figure 5.10.: Wetting factors for different time-steps and linearisation methods. Common simulation parameters are $C_h = 0.01$, $N_I = 8$, $M = 2$, solution with *coupled* and equilibrium boundary condition.

Fig. 5.10 shows that the *optimal* and *none* method have the same temporal evolution of the wetting factor, i.e. the same contact line velocity. Reducing the time-step to $\Delta t = 0.1\mu s$ has no consequence for the *optimal* linearisation. While the *stable* method describes well the spreading phase, the *optimal* and *none* methods lead to an overestimation of the wetting factor and hence its maximum value. In the receding phase one has approximately the same variance between *stable* and the remaining simulations at a given dimensionless time. The phase volume conservation error of all simulations is very similar and bounded by $e_V < 2 \times 10^{-7}$.

Concluding, it has been shown that selecting the *stable* linearisation method as default for the given test case is justified.

5.3.6 Global Mixing Energy Parameter Model

So far the homogeneous mixing energy parameter has been considered, which is now compared with the global mixing energy parameter model of Yue et al. [1], viz.

$$\lambda_{\text{global}} = \sigma \frac{S|_{\overline{c}=0}}{\int_\Omega \frac{1}{2}|\nabla \overline{c}\,|^2 + \frac{1}{\epsilon^2}\Psi(\overline{c})\,d\Omega} = \sigma \frac{S|_{\overline{c}=0}}{F(\overline{c})/\lambda}, \tag{5.3}$$

with initial values

$$\lambda_0 = \frac{3}{2\sqrt{2}}\sigma\epsilon = \lambda, \qquad S_0 = \frac{1}{72}\pi D_0^2, \qquad \left(\frac{F}{\lambda}\right)_0 = \frac{F}{\lambda}(\tau = 0) \equiv \frac{F_0}{\lambda_0}.$$

The initial value λ_0 is the homogeneous lambda model, while the initial iso-surface area S_0 with respect to $\overline{c} = 0$ is derived analytically from the initial droplet dimensions within the 5°-wedge-shaped domain. The numerator in (5.3) is expressed in terms of the Helmholtz free energy (2.2) divided by the homogeneous mixing energy parameter and associated with its starting value, for simplicity.

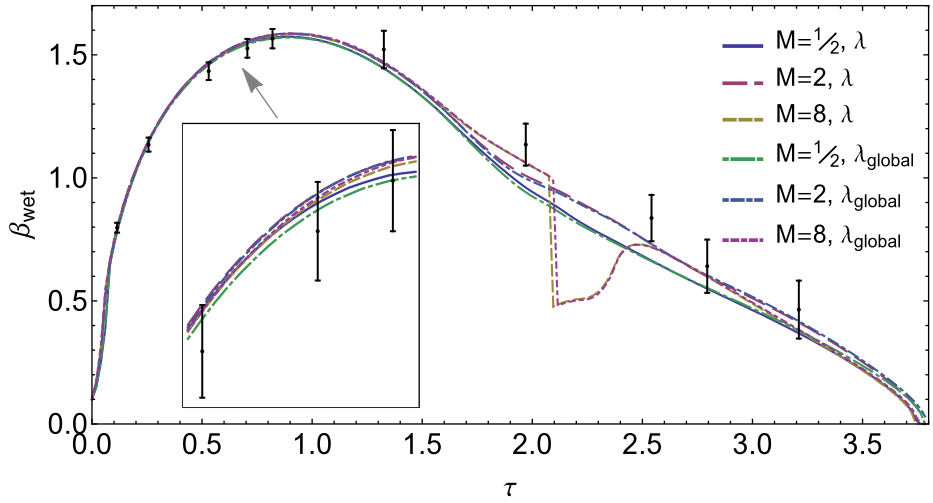

Figure 5.11.: Wetting factors for homogeneous and global mixing energy parameter model and different mobility factors. Common simulation parameters are $C_h = 0.01$, $N_\text{I} = 8$, solution with *coupled-stable* and equilibrium boundary condition.

In Fig. 5.11 the temporal evolution of the wetting factor for global and homogeneous mixing energy parameter model is shown with selected mobility factors. Only negligible differences are observed if both models are compared for the same mobility. The progress of the global mixing energy parameter, Fig. 5.12a, first shows that at initialization λ_{global} is about 1.5% higher compared to the homogeneous

model. The maximal variance depends on the mobility and occurs during the spreading phase around $\tau \approx 0.5$. Within the studied range of M a maximal variance of 5% of the global mixing energy parameter is observed.

Variances of λ_{global} from the homogeneous model are controlled by the ratio S/F. The iso-surface area in Fig. 5.12b and Helmholtz free energy in Fig. 5.12c are fluctuating around the initial value in time. During the spreading phase until $\tau = 0.8$ the iso-surfaces of all three mobilities are approximately the same. This does not hold for the Helmholtz free energy ratio F/F_0 in the same time-interval. The variance of F from initial value gets higher with increased mobility.

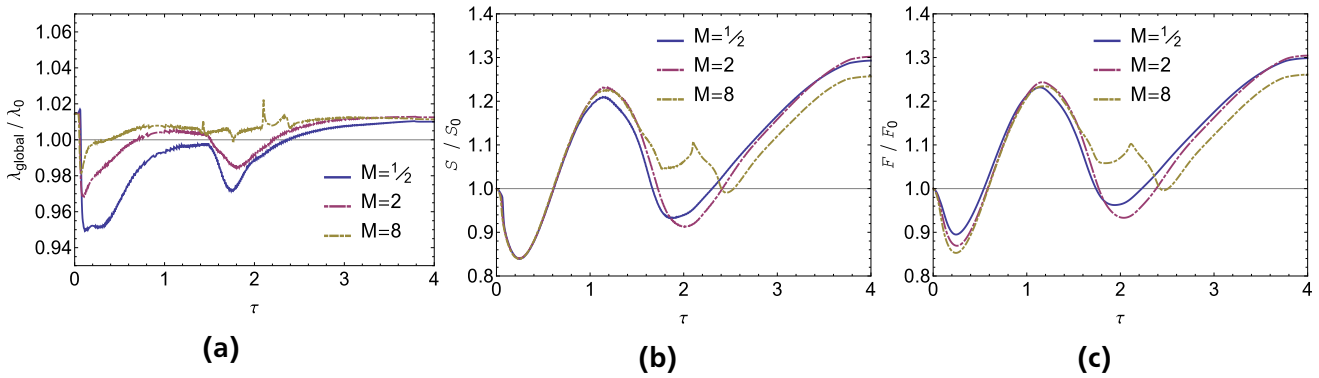

Figure 5.12.: Relative temporal evolution of (a) the global mixing energy parameter, (b) the iso-surface area for $\bar{c} = 0$ and (c) the Helmholtz free energy. Common simulation parameters are $C_h = 0.01$, $N_\text{I} = 8$, $M = 2$, solution with *coupled-stable* and equilibrium boundary condition.

In conclusion, the global mixing energy parameter has only negligible influence on the wetting factor for the given test case. From this point of view it is recommend to use the homogeneous model instead, in order to avoid the interpolation of the iso-contour surface S, which showed a slight increase of computational time. Yue et al. have applied the global model for droplets deforming in shear flow with a constant interfacial thickness of $\epsilon = 0.01$ and different droplet dimensions [1]. They have seen weaker effects of the adjusted λ-model when ϵ is smaller relative to the drop size, i.e. when the Cahn number is low. The Cahn number may be too low in the present case. The main reason for the weak effects of the global model on the wetting factor is that the variance to the homogeneous model is too low. An additional finding is that simulated droplets with high mobility have lower free surface energy compared to simulated droplets with low mobility.

5.3.7 Local Mixing Energy Parameter Model

The local mixing energy parameter model is defined using a limiting value $s \equiv \Psi(\delta_c)/\epsilon^2$ with the correction width δ_c. The interfacial region where the corrected inhomogeneous λ-value is applied ranges from $\bar{c}_{\text{corr}} = 0 \pm \delta_c$.

In Fig. 5.13a the influence of increasing δ_c is shown in comparison to the homogeneous λ-model. For $\delta_c = 0.5$ no variance occur during the spreading phase, while for $\delta_c > 0.6$ the contact line moves faster as the experiment has shown, leading to high variances for $\delta_c = 0.8$. From $\tau = 1$ to $\tau = 2.5$ it can be seen that although different maximal wetting factors are reached, all simulations are contracting again in the late receding phase, being in good agreement with the experiment. Looking at the phase volume conservation error, Fig. 5.13b the simulations with local mixing energy parameter have even lower total variation e_V compared to the homogeneous λ-model.

Regarding the evolution of the local minimum and maximum mixing energy parameter, Fig. 5.14, one first notices that at initialization λ_{min} is more than 10% lower and λ_{max} is more than 8% higher compared

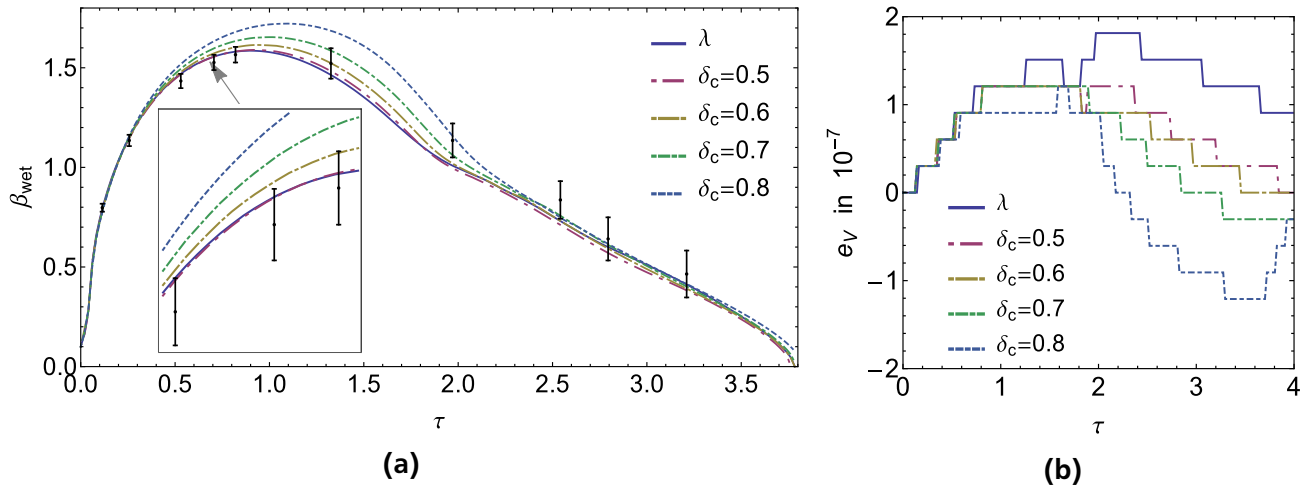

Figure 5.13.: Wetting factors (a) and corresponding phase volume conservation error (b) for different correction widths compared to the homogeneous λ-model. Common simulation parameters are $C_h = 0.01$, $N_\mathrm{I} = 8$, solution method *coupled-stable* with equilibrium boundary condition.

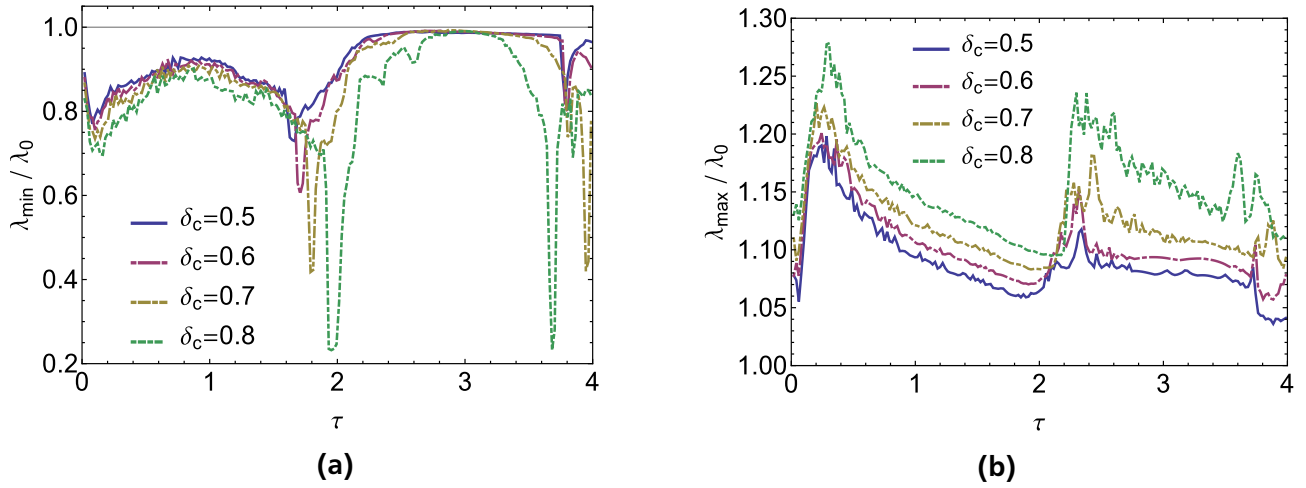

Figure 5.14.: Relative minimum (a) and maximum (b) mixing energy parameter compared to the homogeneous λ-model. Common simulation parameters are $C_h = 0.01$, $N_\mathrm{I} = 8$, solution method *coupled-stable* with equilibrium boundary condition.

to the homogeneous λ-model. Overall a hierarchical process is observed. The maximum total variance from 1.0 is found lower for smaller δ_c. Peaks in λ_{min} occur for $\delta_c = 0.8$, drastically reducing the mixing energy parameter locally. For $\delta_c = 0.6$, respectively $\delta_c = 0.5$, which have wetting factor progresses close to the homogeneous λ-model, the lowest λ_{local} is -40% and the highest λ_{local} is $+20\%$ compared to λ. In comparison $\lambda_{\mathrm{global}}$ shows a maximal total variance of 5%.

In Fig. 5.15 the temporal evolution of the mixing energy parameter field is shown. For all snapshots the scaling is fixed to $\lambda_{\mathrm{local}} = \lambda \pm 1\%$. Blue areas indicate lower and red areas indicate higher λ_{local}-values. Right after initialization ($\tau = 0.2$) most parts of the droplet are in free fall, which is respected by a smaller λ_{local}, since the interface is widened. At the contact line and the successively forming rim λ_{local} is increased. Before the thin lamella is formed ($\tau = 1$) the pressure around the axis increases, which tightens the interface leading to a higher λ_{local}. During $\tau = 1.5$ and $\tau = 2$ the maximum wetting factor was exceeded and the overall λ-value is lowered in the receding phase Similarly to the rim the forming tip of the jet ($\tau = 2.5$) shows higher λ. After the total re-bounce the total variation of the mixing energy

parameter from the homogeneous equilibrium model is lowered compared to the spreading phase. In summary using the local λ-model, an increased λ_{local} is observed at the moving contact line and at high local curvature.

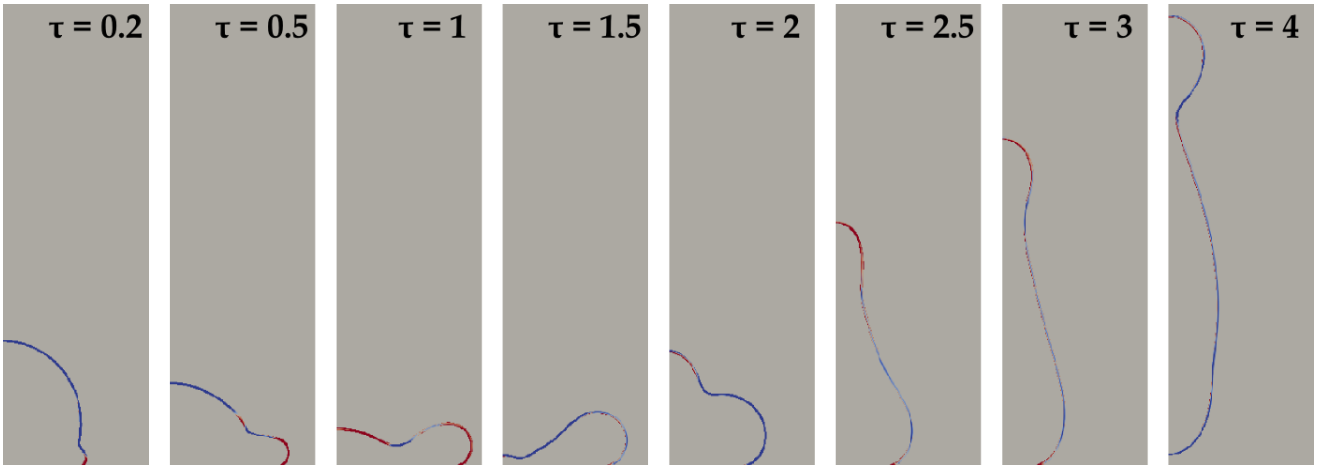

Figure 5.15.: In-homogeneous local mixing parameter field λ_{local} at different times. The scaling is set to $\lambda_{\text{local}} = \lambda \pm 1\%$ where red indicates higher and blue indicates lower values compared to the homogeneous parameter λ in gray. Simulation with $C_h = 0.01$, $N_\text{I} = 8$, $M = 2$, $\delta_c = 0.5$, solution with coupled-stable and equilibrium boundary condition.

Concluding, it has been shown that the local mixing energy parameter can describe the evolution of the wetting factor as appropriate as the homogeneous model, if the correction width is set properly. A natural choice of $\delta_c = 0.9$, which would refer to the 90% mark of total phase-field variation in interfacial normal direction, can be declared not possible. The value $\delta_c = 0.5$ is chosen for future investigation.

5.3.8 Droplet Shape for different Mixing Energy Parameter Models

The droplet shape analysis is another important mean to validate the diffuse-interface model. Unfortunately no experimental data is given in [2], so in this section a qualitative comparison between the different mixing energy parameter models is investigated at two selected time-steps. For the homogeneous λ-model the Cahn number varies from $C_h = 0.02$ to $C_h = 0.005$ and the resolution varies from $N_\text{I} = 8$ to $N_\text{I} = 16$. Both the global and local λ-model have $C_h = 0.01$ and $N_\text{I} = 8$, the latter additionally with $\delta_c = 0.5$ and $\delta_c = 0.6$.

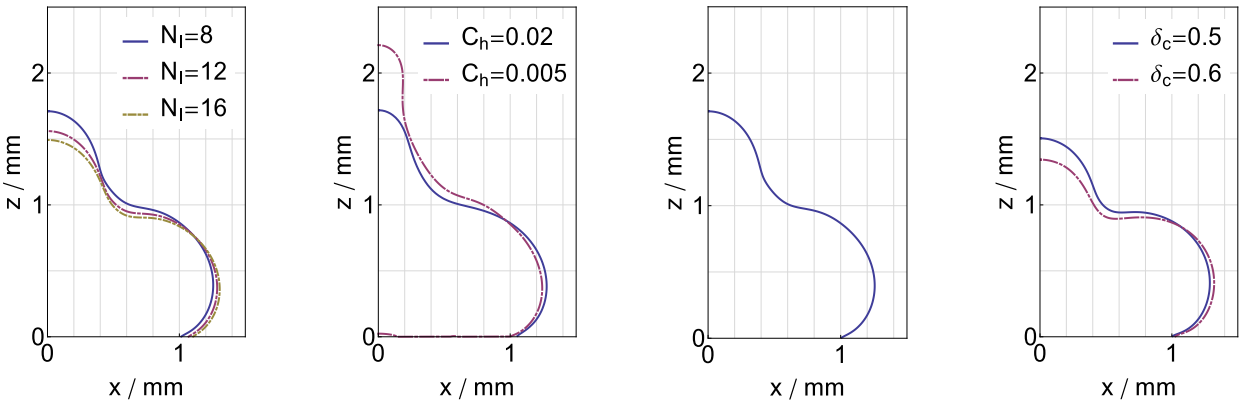

(a) λ, $C_h = 0.01$ **(b)** λ, $N_\text{I} = 8$ **(c)** λ_{global}, $C_h = 0.01$, $N_\text{I} = 8$ **(d)** λ_{local}, $C_h = 0.01$, $N_\text{I} = 8$

Figure 5.16.: Iso-contour lines for $\bar{c} = 0$ at $\tau = 2$ for various model parameters. The mobility factor is set to $M = 2$ and the solution method is *coupled-stable* with equilibrium boundary condition.

In Fig. 5.16 the droplet shapes, i.e. the iso-contour lines for $\bar{c} = 0$, at $\tau = 2$ for different parameters are shown. The droplet is in the receding phase, for all models the wetting factor is $\beta_{\text{wet}} \approx 1$. Larger discrepancies occur for the droplet shape. For the homogeneous model, lowering C_h speeds up the formation of the tip along the z-axis. Increasing N_I has the opposite effect, the tip formation is inhibited. Analogous to the wetting factor progress, the droplet shapes using global and homogeneous λ-models with corresponding resolutions are very much alike. The local mixing energy parameter model inhibits the tip formation. This effect is stronger the larger the correction width is chosen.

The situation after the total re-bounce at $\tau = 4$ is shown in Fig. 5.17. The general shape resembles a bowling pin, an elongated waist and spherical tip separated by a strangling. Again the global and homogeneous models are much alike. The delay in tip formation for higher N_I has proceeded from $\tau = 2$. For low Cahn number the droplet dimension in z-direction is slightly larger. Also for $C_h = 0.005$ the droplet shape is different and looks more like a bottle, which resembles a large scale capillary wave around $z = 2.5\,\text{mm}$. The droplet shapes for the local mixing energy parameter model are further stretched in z-direction. The tip forming delay from $\tau = 2$ for $\delta_c = 0.6$ is now reversed and the tip is over 1 mm ahead of the other λ-models. Increasing δ_c further leads to the detachment of the spherical tip into a separated secondary droplet.

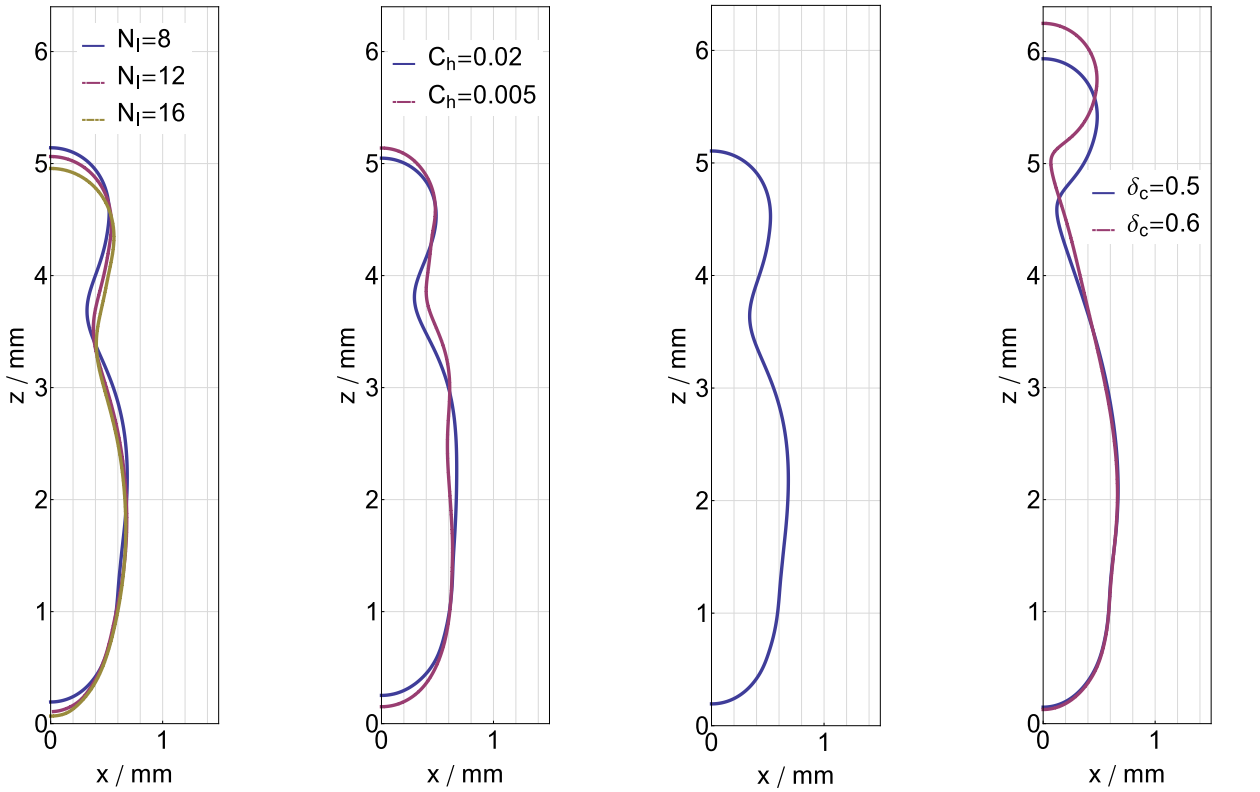

(a) λ, $C_h = 0.01$ **(b)** λ, $N_\text{I} = 8$ **(c)** λ_global, $C_h = 0.01$, $N_\text{I} = 8$ **(d)** λ_local, $C_h = 0.01$, $N_\text{I} = 8$

Figure 5.17.: Iso-contour lines for $\bar{c} = 0$ at $\tau = 4$ for various model parameters. The mobility factor is set to $M = 2$ and the solution method is *coupled-stable* with equilibrium boundary condition.

In conclusion, a majority of studied models have very similar droplet shape evolutions, especially no difference was observed for homogeneous and global λ-models. Interesting findings are the faster tip formation for low Cahn numbers and the droplet stretching effect of the local model, which increases with δ_c.

6 Shape Analysis of Droplet Spreading on a Super-Hydrophobic Substrate [3]

The simulation of a spherical water droplet with initial velocity impacting on a planar and macroscopically smooth, super-hydrophobic surface is studied in this chapter. Experimental data from Yun [3] are used, which are intentionally close to the experiment from Roisman in chapter 5 with similar droplet dimension, velocity and contact angle. In this sense, both experiments complement each other so that a complete validation of the droplet behavior, i.e. the contact line motion and droplet shape evolution, is achieved.

The objective in this chapter is to compare the simulated droplet shapes, i.e. the iso-contour lines for $\bar{c} = 0$, with experimental high-speed images taken from [3], shown in Fig. 6.1.

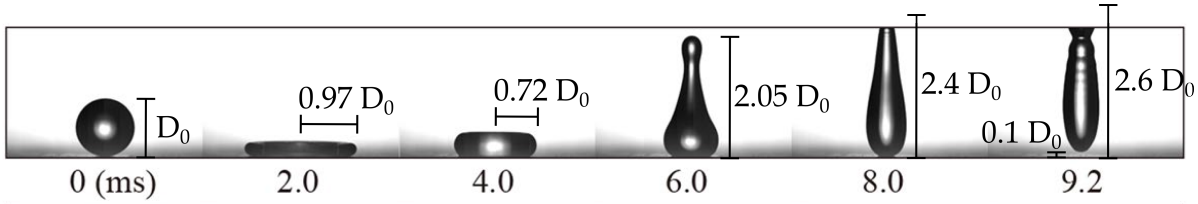

Figure 6.1.: High-speed images of a water drop ($D_0 = 1.97\,\mathrm{mm}, U_0 = 1.0\,\mathrm{m\,s^{-1}}, We = \rho D_0 U_0^2/\sigma = 27$) impacting on a super-hydrophobic substrate ($\theta_e = 160 \pm 3°$) from Yun [3]. Additional length scales were added, which stem from graphic analysis.

Additionally to the original figure, length scales in terms of the initial droplet diameter D_0 have been added in Fig. 6.1, which were derived from graphic analysis, i.e. manually. For $t = 8\,\mathrm{ms}$ and $t = 9.2\,\mathrm{ms}$ the drop was outside the range of the high-speed camera, so the corresponding length scales can only give a rough approximation.

6.1 Case Setup

Yun's experiment is close to Roismans's setup in Sec. 5.1, so in the following only the modifications are described. The initial droplet diameter is lowered to $D_0 = 1.97\,\mathrm{mm}$ and the impact velocity perpendicular to the surface is increased to $U_0 = 1.0\,\mathrm{m\,s^{-1}}$. As a consequence the 2D axis-symmetric computational domain size, shown in Fig. 6.2, is increased to a height of $8D_0$. In [3] a contact angle of $160 \pm 3°$ has been measured. Accordingly, the equilibrium contact angle for the *phaseContactAngle* boundary condition is set to $\theta_e = 160°$. Properties of the studied meshes are shown in Tab. 6.1. The reduction of the total amount of control volumes (#CV) is drastic due to the use of adaptive mesh refinement, see section 5.1.2. The solution process is left unchanged, details can be found in section 5.1.3.

6.2 Simulation Campaign

A summary of different models, methods and parameters within the phase-field context is given, which are available in the PHASEFIELDFOAM-solver and relevant for the present test case. Thereafter, the simulation campaign for the experiment by Yun [3] is described.

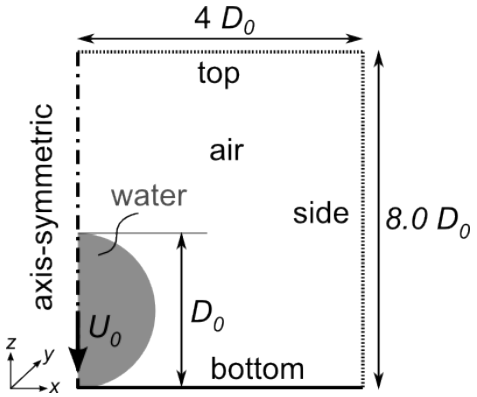

Figure 6.2.: Initial 2D-axis-symmetric case setup with chosen fixed domain dimensions and boundary notations.

N_I	n_x	n_z	N_ref	#CV init.	reduction
8	25	50	5	13172	-99.0%
16	25	50	6	27752	-99.5%

Table 6.1.: Setup of mesh properties for different interfacial resolutions.

6.2.1 Parameter Space

The different models and methods are shown in Tab. 6.2. Additionally to the study of the previous chapter, the viscosity interpolation method within the PHASEFIELDFOAM-solver was updated to a new version *V2*. In Tab. 5.4 the parameters of the phase-field model are presented with corresponding values applied in the present test case. The parameter space is reduced based on the findings of the previous chapter.

Model / Method	Representation
solution procedure of the Cahn-Hilliard system	*coupled* (3.5), [*segregated*]
linearisation method of non-linear potentials	*stable* (3.2), *optimal* (3.4), [*none*]
boundary condition of $\overline{c}$ on solid surfaces	equilibrium (2.22c), [non-equilibrium]
mixing energy parameter	homogeneous (2.7), global (2.25), local (2.30)
viscosity interpolation method	*V1* (Listing 4.1), *V2* (Listing 4.2)
viscosity model	*arithmetic* (4.1), *harmonic* (4.2), *blended* (4.3)

Table 6.2.: Overview of different models and methods applied in the phase-field model for the present test case. Additionally available yet unused models are shown in square brackets.

Parameter	Description	Values
C_h	Cahn number defined by $C_h = \frac{\epsilon}{D_0}$	{ 0.005, 0.01 }
N_I	number of control volumes in interfacial direction / interfacial resolution	{ 8, 16 }
M	mobility factor for scaling law $\kappa = M\epsilon^2$	{ 2 }
δ_c	correction width, local λ-model applied for cells with $\overline{c}_\mathrm{corr} = 0 \pm \delta_c$	{ 0.5, 0.6, }

Table 6.3.: Overview of different parameters of the phase-field model with brief description and studied values for the present test case.

6.2.2 Parameter Study

The experiment by Yun [3] is considered as a complement to the previous chapter by validating the droplet shape evolution, rather than the wetting factor. In order to ensure comparability of both test cases, in section 6.3.1 the *coupled* solution procedure is applied with *stable* and *optimal* linearisation to begin with. Most of the parameters stem from the previous test case, which were found in good agreement for *stable* linearisation. Analyzing the contact line motion an appropriate linearisation method will be chosen for further simulations.

In section 6.3.2 the simulated droplet shapes are validated for different mixing energy parameter models using approximated experimental droplet dimensions from graphic analysis. The viscosity calculation so far is done with interpolation method *V1* and model *harmonic*. Only a limited phase-field parameter space for Cahn number, mobility and interfacial resolution is used.

Instead of expanding the phase-field parameter space further, in section 6.3.3 the new viscosity interpolation method *V2* is validated, which allows the use of further viscosity models like *arithmetic* and *blended* in the present dynamic droplet spreading setup. Differences of the single viscosity models are examined and a comparison with the previous viscosity interpolation is given.

Finally, in section 6.3.4 a direction comparison of experimental and simulated droplet shapes is given. The influence of the interfacial thickness is studied for all viscosity models and interpolations combinations from sections 6.3.2 and 6.3.3.

6.3 Simulation Results

6.3.1 Comparison of Solution Methods

The first simulations are used to compare the two linearisation methods *stable* and *optimal*. The fixed parameters are chosen based on the findings of the previous chapter, where good agreement of the contact line motion with experimental data has been found for a comparable case setup. The fixed parameters are $C_h = 0.01$ and $M = 2$ as well as an interfacial resolution of at least $N_\mathrm{I} \geq 8$. The solution procedure is *coupled* with equilibrium boundary condition and the viscosity interpolation is the old version *V1* with viscosity model *harmonic*. The viscosity treatment is the same as in the previous chapter.

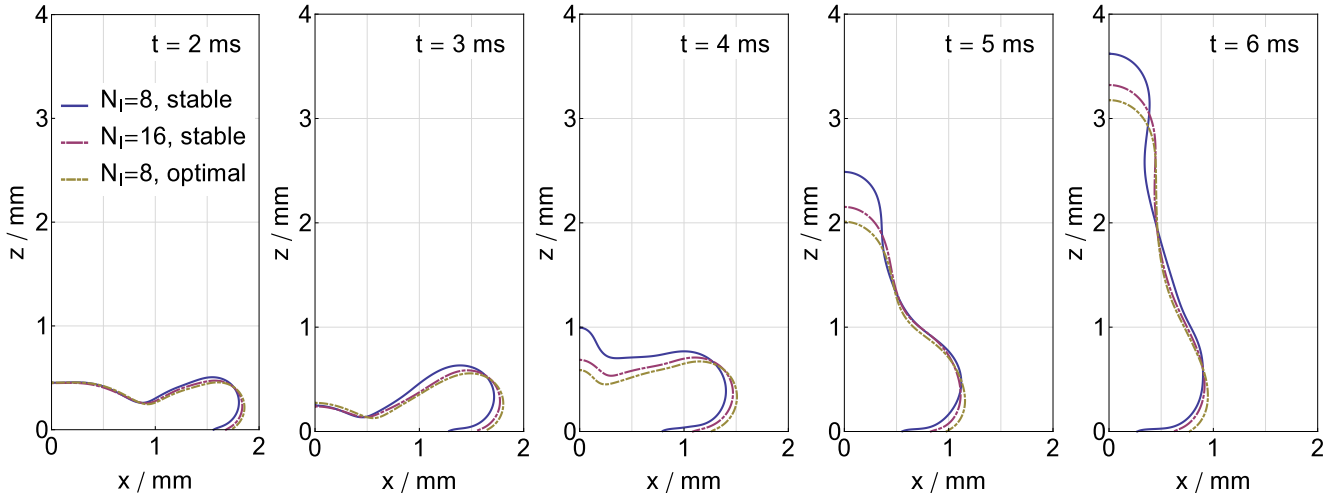

Figure 6.3.: Temporal evolution of iso-contour lines ($\overline{c} = 0$) for different linearisation methods and interfacial resolutions. Common simulation parameters are $C_h = 0.01$, $M = 2$ and the solution method is *coupled* with equilibrium boundary condition and viscosity model *V1-harmonic*.

In Fig. 6.3 the temporal evolution of iso-contour lines for $\bar{c} = 0$ is shown governing approximately the late spreading phase to mid receding phase. A large discrepancy is observed for the contact line motion of the *stable* and *optimal* linearisation with $N_\mathrm{I} = 8$. The receding velocity of the contact line for *stable* is faster, hence for $t \geq 3\,\mathrm{ms}$ the contact line undercuts the rim leading to an hovered water volume. No undercuts are observed for *optimal* as well as in Fig. 5.16, the latter using the *stable* method. The tip formation at $t = 4\,\mathrm{ms}$ is also faster for *stable* so that the droplet dimension along the z-axis at $t = 6\,\mathrm{ms}$ is larger. The *stable* method is also tested with $N_\mathrm{I} = 16$. Increasing the interfacial resolution reduces the undercut tendency and the overall droplet shapes can be describes as an interlude between the $N_\mathrm{I} = 8$ simulations, slightly more similar to *optimal*. Regarding the apparent contact angle one notices that the *optimal* method shows approximately a lower value as 160°.

Concluding, the *stable* method, which was the best choice for the experiment by Roisman [2], now has an unexpected influence on the contact line. The undercut seems to be nonphysical, at least no evidence can be seen in Fig. 6.1. Compared to the previous chapter, the equilibrium contact angle is increased by 15°, which most likely the main reason for the failure of the *stable* method. A higher interfacial resolution helped to reduce the undercut tendency, but it is to be pointed out that such high number of interfacial cells are not encountered in literature to the authors knowledge. Recall that the domain is 2D axis-symmetric, so that cell volumes increase in x-direction. The increased tip formation of the *stable* method is a consequence of the undercut, since a higher amount of water gathers closer to the axis enhancing the displacement. To avoid the influence of a nonphysical contact line motion on the transient characteristic of the droplet shape, the linearisation method of the present test case is set to *optimal* further on.

6.3.2 Comparison of Mixing Energy Parameter Models

The simulated droplet shape evolution is compared with experimental results in this section. The phase-field parameters are set to $C_h = 0.01$, $N_\mathrm{I} = 8$ and $M = 2$. The solution procedure is *coupled-optimal* with equilibrium boundary condition and the viscosity interpolation is *V1* with viscosity model *harmonic*.

In Fig. 6.4 the droplet shape evolution for homogeneous, global and local mixing energy parameter models are shown, the latter with two different correction widths δ_c. The different times correspond to Fig. 6.1. To improve the comparison between simulations and experiment, red lines where added which refer to the experimental droplet dimensions. First it is observed that homogeneous and global λ-model have thoroughly conformable droplet shapes in the simulated time interval. At $t = 2\,\mathrm{ms}$ all simulated droplets form a flat disc, the dimension of which is in good agreement with the experimental high-speed image and approximately shows the maximum spreading in x-direction. At $t = 4\,\mathrm{ms}$ the experiment indicates a faster receding of the droplet, where the local model is less consistent but the variance decreases with lower δ_c. The disc has thickened in z-direction and no tip is observed experimentally. For the homogeneous model the tip formation has started, but this is not visible in a 360° domain. At $t = 6\,\mathrm{ms}$ the transient characteristic of the experimental droplet is not matched, all simulations are about 0.8 mm behind in z-direction. Between $t = 8\,\mathrm{ms}$ and $t = 9.2\,\mathrm{ms}$ the total re-bounce of all simulated droplets occur. The variance of homogeneous and local λ-model is maximal at the last time. In z-direction the droplet is lengthened for λ_local, which increases for higher δ_c. The bottom-wall distance is slightly too low for all simulations, while the upper bounds show that the homogeneous model is in better agreement. However, caution has to be taken for the last two images because the upper bounds were extrapolated, since the experimental droplets were out of the camera range.

In conclusion, no tested λ-model has captured the transient characteristic of the experiment accurately for this given test case with $C_h = 0.01$. The real droplet recedes faster and is more stretched before and more compressed after the total re-bound, the latter inducing capillary waves. However a good overall resemblance is observed, which is a promising start for further parameter or model variations. The local λ-model leads to a significant stretching tendency after the total re-bound, similarly to Fig.

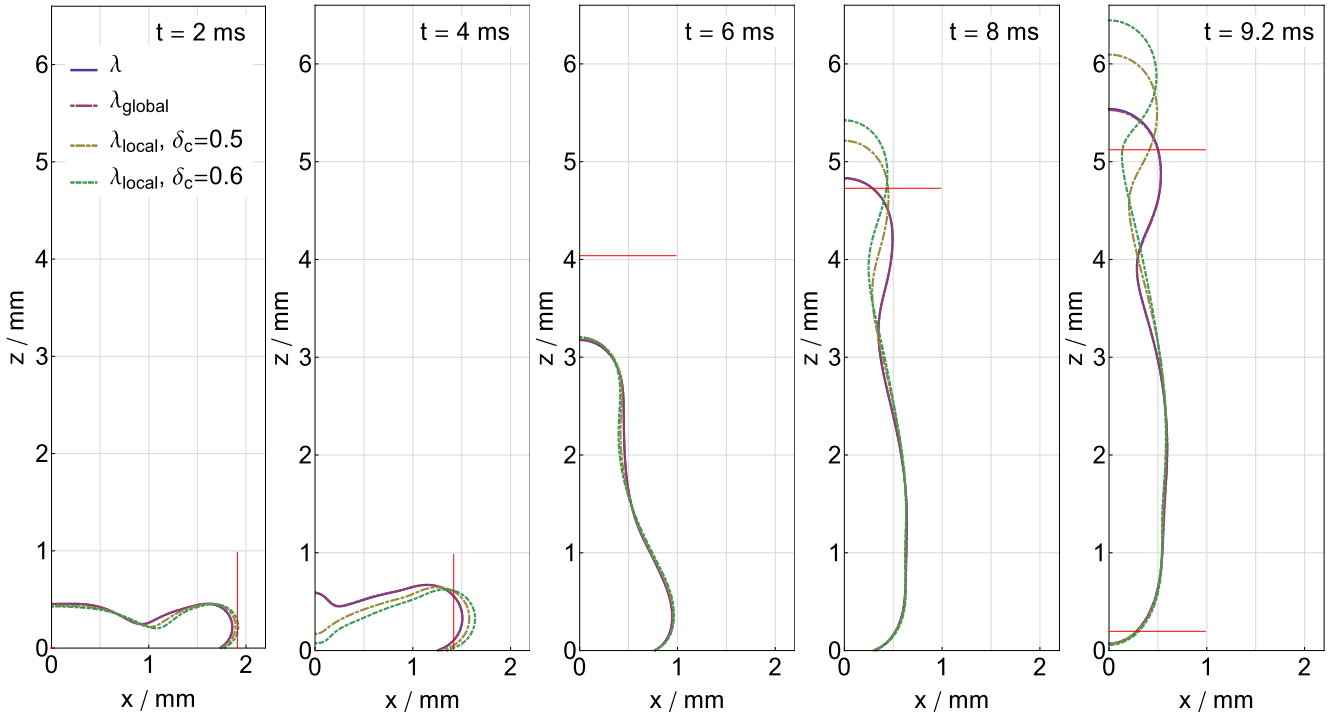

Figure 6.4.: Temporal evolution of iso-contour lines ($\bar{c} = 0$) for different mixing energy parameter models. Common simulation parameters are $C_h = 0.01$, $N_\mathrm{I} = 8$ and $M = 2$ and the solution method is *coupled-optimal* with equilibrium boundary condition and viscosity model *V1-harmonic* Sketched red lines with length $D_0/2$ mark the experimental droplet dimensions derived from graphic analysis (Fig. 6.1).

5.17d. In agreement with the test case from of the previous chapter, almost no difference between the homogeneous and global λ-model is observed.

6.3.3 Comparison of Viscosity Models

So far in this work the viscosity interpolation *V1* was studied with *harmonic* viscosity calculation. This choice was made because *V1* together with *arithmetic* or *blended* viscosity models showed nonphysical velocity fields, where artificial air-phase peaks occurred. In the course of this work the viscosity interpolation has been updated to version *V2* and test simulations have shown that the artificial velocity vanishes. In this section three viscosity models applied with *V2* are studied and the phase-field parameters are set to $C_h = 0.01$, $N_\mathrm{I} = 8$ and $M = 2$. The solution procedure is *coupled-optimal* with equilibrium boundary condition.

In Fig. 6.5 the droplet shape evolution for *arithmetic*, *harmonic* and *blended* viscosity models are shown. Similar to Fig. 6.4, the simulations are temporarily behind the experiment for $t = 4\,\mathrm{ms}$ and $t = 6\,\mathrm{ms}$. The main difference is that after the total re-bounce the bottom wall distance is higher and the tip is more spherically shaped. Comparing the viscosity models with each other one observes different shape behavior. For example at $t = 6\,\mathrm{ms}$ the *blended* model shows a capillary wave around $z = 2\,\mathrm{mm}$, which is however not present in the experiment. For $t \geq 6\,\mathrm{ms}$ the bottom part of the *arithmetic* model is more spherical. Overall the *harmonic* and *blended* models are more alike compared to *arithmetic*. For *arithmetic* the bottleneck in the last image is placed approximately at the same height as seen in the experiment, while the bottlenecks of the other models are located higher in z-direction.

A closer look around the maximum spreading and starting receding phase of the droplet is shown in Fig. 6.6. Although all viscosity models have approximately the same wetting factor, i.e. position of the

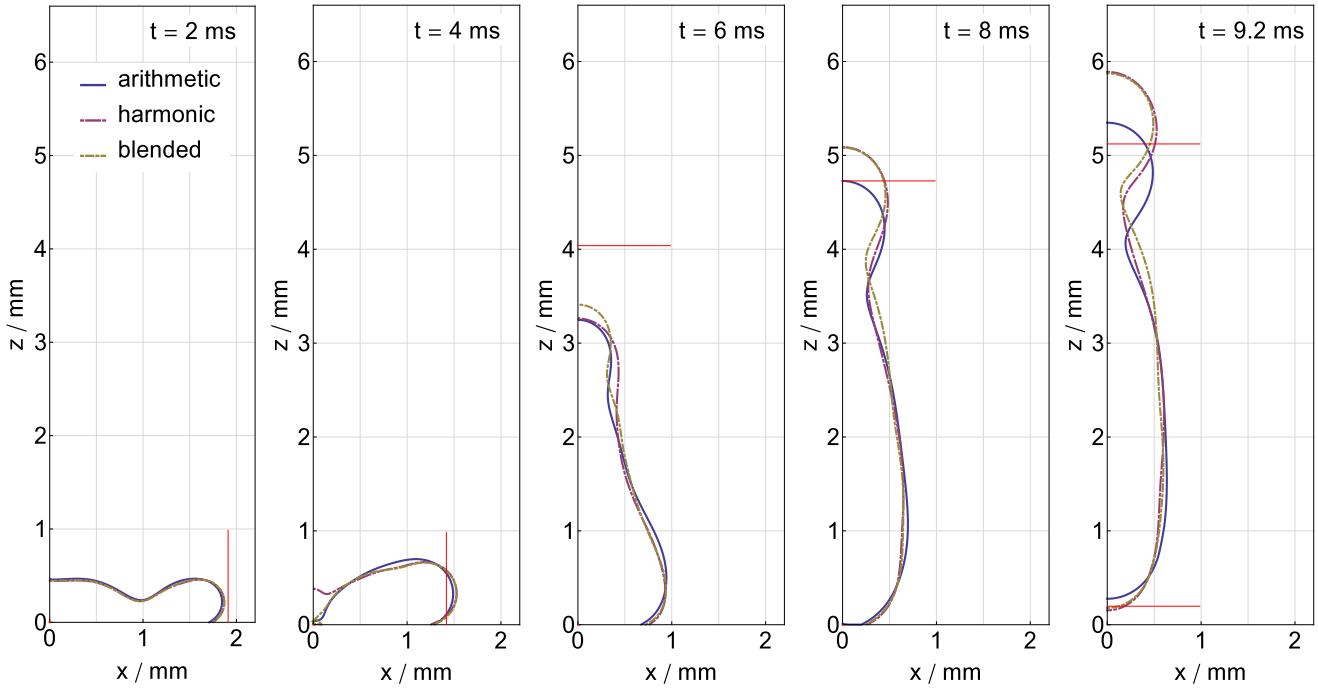

Figure 6.5.: Temporal evolution of iso-contour lines ($\bar{c} = 0$) for different viscosity models. Common simulation parameters are $C_h = 0.01$, $N_\mathrm{I} = 8$ and $M = 2$, homogeneous λ-model, viscosity interpolation method *V2* and the solution method is *coupled-optimal* with equilibrium boundary condition. Sketched red lines with length $D_0/2$ mark the experimental droplet dimensions derived from graphic analysis (Fig. 6.1).

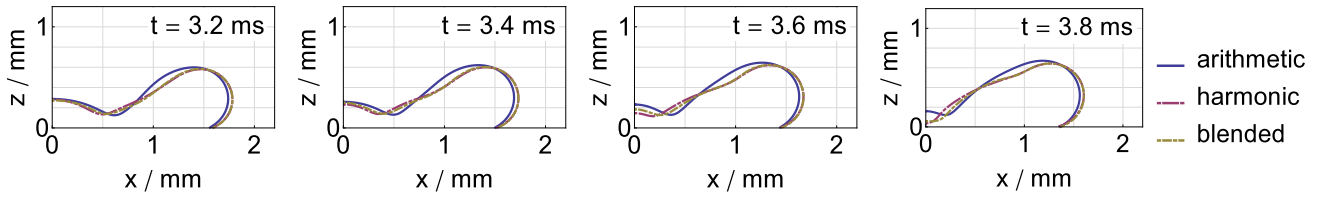

Figure 6.6.: Shape evolution of lamella and rim for different viscosity models. Common simulation parameters are $C_h = 0.01$, $N_\mathrm{I} = 8$ and $M = 2$, homogeneous λ-model, viscosity interpolation method *V2* and the solution method is *coupled-optimal* with equilibrium boundary condition.

contact line of $\bar{c} = 0$, rim and lamella are shaped differently. The *arithmetic* model leads to a round and less complex shape, while the other models look much alike and lead to an additional wave between rim and lamella.

Concluding, it has been demonstrated that the new viscosity interpolation *V2* with *arithmetic* viscosity calculation is the best candidate to bring the simulated droplet shape into agreement with the experiment for $C_h = 0.01$. Yet work is to do to improve and match the transient characteristic. As a next step it is recommend to study a smaller C_h, since in Fig. 5.16 a finding has been that this enhances the tip formation.

6.3.4 Variation of Interfacial Thickness

In this section a direct comparison of experimental and simulated droplet shapes is shown with varying interfacial thickness expressed by the Cahn number $C_h = \epsilon/D_0$. The value $C_h = 0.01$ is denoted as medium, while $C_h = 0.005$ is denoted as low Cahn number. For all simulations the common setting is

$N_\mathrm{I} = 8$ interfacial cells and mobility parameter $M = 2$, *coupled* solution procedure, equilibrium boundary condition and *optimal* linearisation method. Using the homogeneous mixing energy parameter model, all viscosity settings from this work are tested; viscosity interpolation *V1* with *harmonic* viscosity model in Fig. 6.7 and *V2* with *arithmetic*, *harmonic* and *blended* in Fig. 6.8. Additionally, the local mixing energy parameter model is tested, see Fig. 6.10.

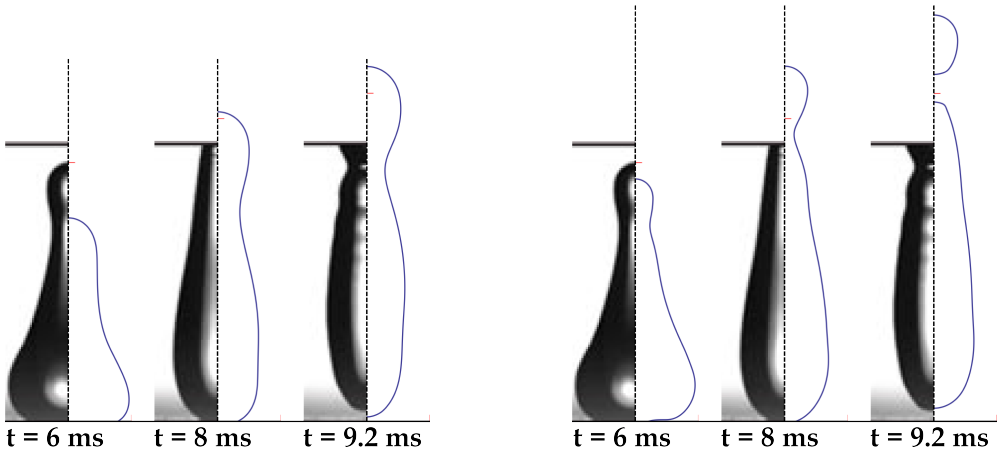

(a) $C_h = 0.01$ **(b)** $C_h = 0.005$

Figure 6.7.: Direct comparison of experimental (left) and simulated (right) droplet shapes at different times for two Cahn numbers (a) and (b). Common simulation parameters are $N_\mathrm{I} = 8$ and $M = 2$ with homogeneous λ-model, viscosity model *V1-harmonic*, solution method *coupled-optimal* and equilibrium boundary condition.

In Fig. 6.7a and 6.7b simulated results for medium and low Cahn numbers are compared with experimental high-speed images from [3] using the same viscosity model as in chapter 5. At $t = 6\,\mathrm{ms}$ the simulated droplet tip at low C_h has improved and is close to the experimental shape forming a bottleneck in contrast to medium C_h. One notices the undercut at the bottom, which resulted from a torus-formation (dry-out of the thin lamella with bubble entrapment moving in radial direction) at $t = 3.8\,\mathrm{ms}$ and should not be confused with undercuts using the *coupled-stable* solution procedure in section 6.3.1. At $t = 8\,\mathrm{ms}$ the experimental droplet forms a round-like main bottom part governed with low C_h, while with medium C_h the bottom part is bottle-shaped and has a misplaced bottle-neck. At $t = 9.2\,\mathrm{ms}$ there is uncertainty regarding the experimental tip behavior. The simulation with low C_h shows a droplet detachment and still misses any capillary waves. However the distance to the bottom is well matched.

In Fig. 6.8a and 6.8b the direct experimental comparison is done for the *arithmetic* viscosity model with interpolation *V2*. Overall the influence of C_h on the droplet shape is negligible for the observed times. At $t = 6\,\mathrm{ms}$ the droplet has close resemblance with the experiment, yet the transient is not matched correctly. The round-like main bottom part is well reproduced.

Comparable results are observed in Fig. 6.8c and 6.8d for *V2-blended*. However, one can deduce that the shape for low C_h has gotten worse because the transient characteristic seems to have fallen behind the one with medium C_h. This can be seen by the dimension in z-direction at $t = 6\,\mathrm{ms}$ and the bottle-neck position at $t = 8\,\mathrm{ms}$.

Lowering the Cahn number has huge influence for the *V2-harmonic* model shown in Fig. 6.8a and 6.8b. Similarly to *V1-harmonic* (Fig. 6.7b), the transient characteristic of the tip formation at low C_h has been improved, now matching exactly the experimental z-dimension. In the tip formation process small droplets are ejected with low C_h. At $t = 8\,\mathrm{ms}$ simulated and experimentally observable droplet shapes are in very good agreement. However at $t = 9.2\,\mathrm{ms}$ still no small-scale capillary waves occur in the mid part of the droplet. A large-scale capillary wave forms from tip to mid-part.

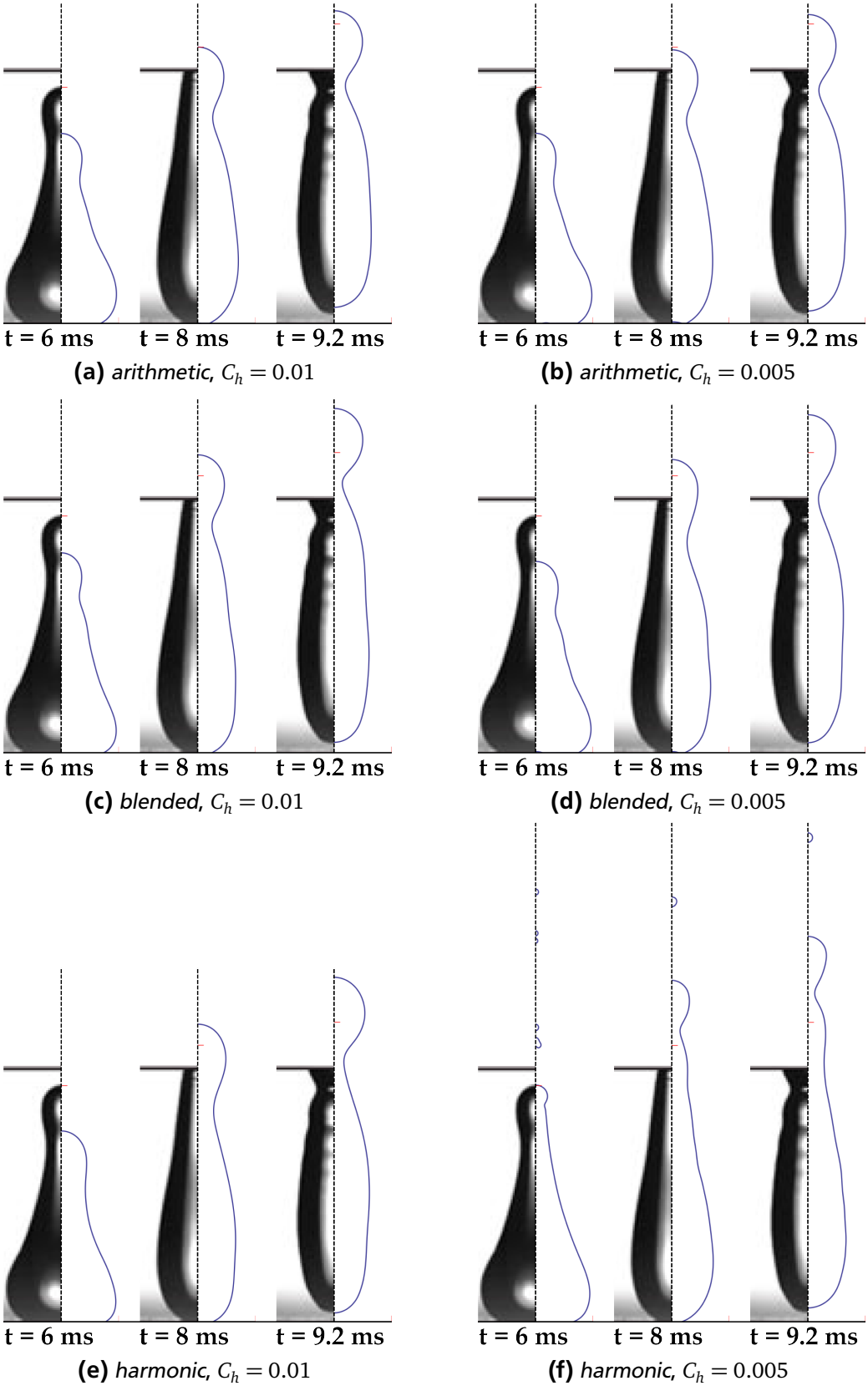

(a) *arithmetic*, $C_h = 0.01$ **(b)** *arithmetic*, $C_h = 0.005$

(c) *blended*, $C_h = 0.01$ **(d)** *blended*, $C_h = 0.005$

(e) *harmonic*, $C_h = 0.01$ **(f)** *harmonic*, $C_h = 0.005$

Figure 6.8.: Direct comparison of experimental (left) and simulated (right) droplet shapes at different times for two Cahn numbers and three viscosity models. Common simulation parameters are $N_\mathrm{I} = 8$ and $M = 2$ with homogeneous λ-model, viscosity interpolation *V2*, solution method *coupled-optimal* and equilibrium boundary condition.

In Fig. 6.9 the tip formation process for the simulation with *V2-harmonic model* from Fig. 6.8f is shown. Around $t = 4.4\,\text{ms}$ a small volume of water is accelerates along the z-axis forming a very sharp peak. At $t = 5.2\,\text{ms}$ a small secondary droplet is detached, while the remaining tip only consists of one inner bulk cells over a length of about $D_0/2$. Subsequently, the droplet is stretched further and the tip gets thinned until the interface collapses around $t = 5.5\,\text{ms}$ and multiple small droplets are formed. After $t = 5.8\,\text{ms}$ the detachments stop and a spherical tip starts to form.

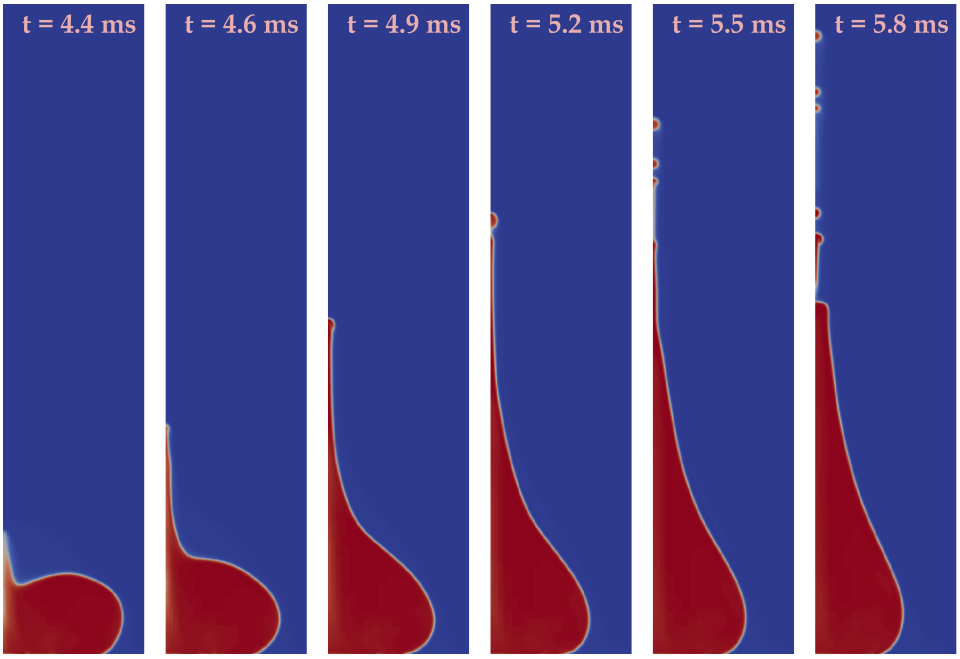

Figure 6.9.: Temporal evolution of the tip formation for the *V2-harmonic* viscosity model with $C_h = 0.005$, $N_\text{I} = 8$ and $M = 2$ with homogeneous λ-model, *coupled-optimal* solution procedure and equilibrium boundary condition.

The local mixing energy parameter model with $\delta_c = 0.5$ and *V2-harmonic* is used in Fig. 6.10a and 6.10b. One can observe that for medium C_h the tip formation at $t = 6\,\text{ms}$ is temporally behind the experiment and has close resemblance with Fig. 6.8. Later on the droplet is slightly more stretched in z-direction detaching a large spherical drop. For low C_h the stretching is increased, however, the drop detachment is delayed. Compared to Fig. 6.8f the overall cohesion of the interface is increased, and no tiny satellite droplets are observed. Especially at $t = 8\,\text{ms}$ the observed droplet shape is in very good agreement with the experiment.

In Fig. 6.11 the droplet shape evolution is shown from $t = 9.5\,\text{ms}$ to $t = 10\,\text{ms}$ after detachment of a satellite drop. The detached spherical drop is moving upwards, while the droplet tip is slightly retracting downwards. One can observe a small capillary wave forming around the main droplet tip. However, only one small capillary wave is formed, while the experiment shows multiple ones at lower times.

In conclusion, it has been shown that the influence of the interfacial thickness depends on the viscosity model. Using the *harmonic* model with interpolation method *V1* or *V2* and low Cahn number, the plasticity of the droplet is drastically increased leading finally to a matched transient characteristic for the present test case. However, this comes with droplet detachments, which can not be validated due to the limited experimental data range. The behavior of the droplet tip is very interesting and the *harmonic* model has suggested that there might be more behind to study on. The local mixing energy parameter model has showed the potential to increase the interfacial cohesion using the *harmonic* viscosity model with low Cahn number. This avoids the very sharp tip formation with tiny satellite drops, which might not be physical. If the experiment would show a clear spherical tip at $t = 8\,\text{ms}$, then λ_local helps to match the stretched experimental main bottom part even with medium Cahn number.

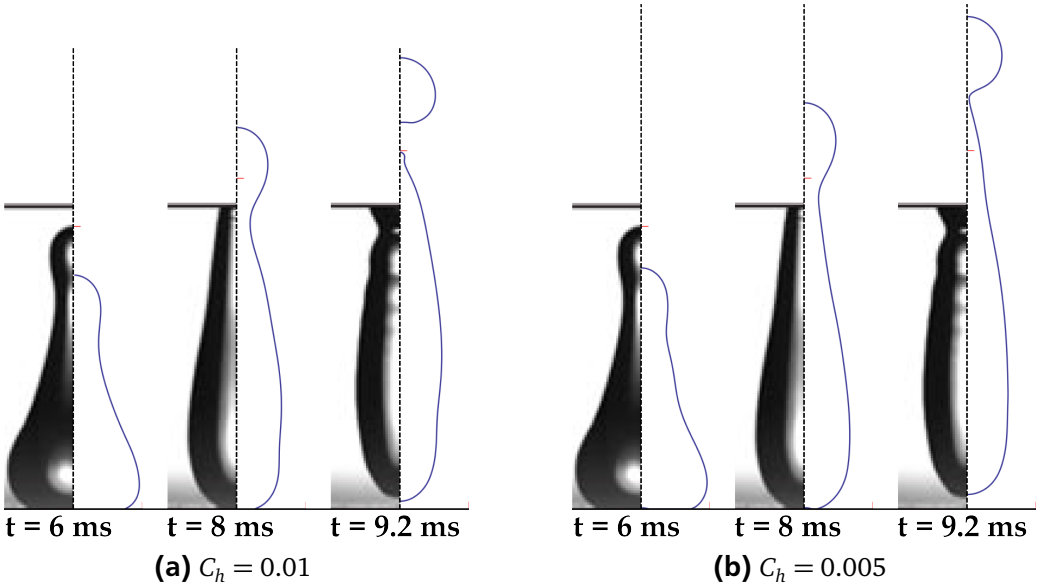

(a) $C_h = 0.01$ **(b)** $C_h = 0.005$

Figure 6.10.: Direct comparison of experimental (left) and simulated (right) droplet shapes at different times for two Cahn numbers (a) and (b). Common simulation parameters are $N_\mathrm{I} = 8$ and $M = 2$, λ_local-model with $\delta_c = 0.5$, viscosity model *V2-harmonic*, solution method *coupled-optimal* and equilibrium boundary condition.

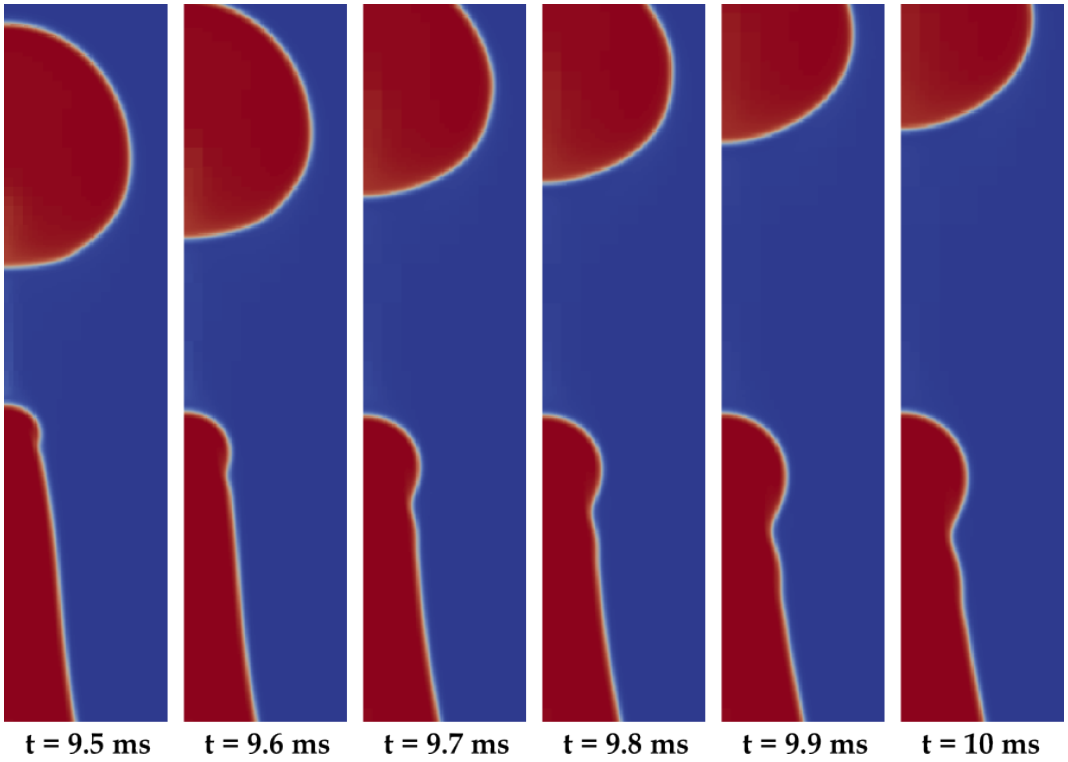

Figure 6.11.: Evolution of a small capillary on the main droplet tip after drop detachment. Common simulation parameters are $C_h = 0.005$, $N_\mathrm{I} = 8$ and $M = 2$, λ_local-model with $\delta_c = 0.5$, viscosity model *V2-harmonic*, *coupled-optimal* solution procedure and equilibrium boundary condition.

7 Executive Summary

Regarding the first fundamental questions it has been demonstrated that it is possible to use the diffuse-interface phase-field model for dynamic wetting processes on super-hydrophobic substrates and get good agreement with experiments. It has been shown in this work that super-hydrophobicity can be modelled by a single parameter, namely the equilibrium contact angle θ_e. Neither micro-structures nor additional contact line motion theory, like artificial pinning in the VOF context [35], were necessary for the given test cases. Applying only the natural boundary condition (2.10) for the phase-field on fluid-solid surfaces, the evolution of the wetting factor for a millimeter-sized droplet with about $Re \approx 2000$ can be well described; not only for the spreading phase but also for the receding phase. The mobility law (2.14) can be assumed to give the right scaling with respect to the capillary width. Relatively small modifications were needed for the mobility parameter to optimize the wetting factor, even setting the default value results into good experimental agreement.

An interesting finding for the diffuse-interface contact line motion, i.e. the motion of the iso-contour line $\overline{c} = 0$, is that lowering the Cahn number or the mobility leads to a faster receding droplet after the maximum wetting factor was reached. The lower the interfacial thickness or the mobility parameter, the higher the influence of advection processes in relation to diffusion processes, described also by the Péclet number. Hence, a well chosen amount of diffusion has been seen to effectively hinder the droplet receding, resulting in better agreement with experiments.

Using a homogeneous λ-model it is a challenging task to match the transient droplet shape charateristic precisely, beginning with the droplet tip formation until several milliseconds after the total re-bounce. The simulated interfaces have seemed to be too rigid and less flexible as in the experiment, the latter even showing small capillary waves. However, several aspects of the simulated droplet shapes have been seen to be in good agreement; for example the main bottom part of the droplet or the droplet-bottom distance after total re-bounce. A basic idea to improve the transient characteristic is to reduce the interfacial thickness, thereby increasing advection influences. Compared to other works [17, 18, 36], which use diffuse-interface phase-field models for rapid spreading, a fairly low Cahn number has been tested. However, notable transient improvements on the droplet deformability have only been seen for the *harmonic* viscosity model, leading to a very sharp tip, which is probably nonphysical.

Regarding the second fundamental questions, two additional mixing energy parameter models have been tested. For the simulated droplet dynamics the global approach (2.25) by Yue et al. [1] has been seen to have negligible influence on the wetting process and the droplet shape. Hence, it is recommended to not use the global approach in dynamic cases, since the computational cost is increased by the run-time iso-contour calculation. A promising new approach for the mixing energy parameter is the local model (2.30), derived in this work based on the global approach. In the local model the correction width δ_c occurs as an additional parameter. If the correction width is properly chosen, here $\delta_c = 0.5$, the simulated wetting process for the local model has been in good agreement with the experiment, closely resembling the homogeneous λ-model. An improvement in droplet shape deformability in terms of stretching has been seen for the local model compared to a homogeneous λ-model. The local model has also shown a cohesive effect for the interface, reducing the sharp tips of the *harmonic* viscosity model. The best results have been seen for the *harmonic* viscosity model in combination with a local mixing energy parameter and $C_h = 0.005$, which is a recommended setup to start further investigations.

Several numerical and technical improvements for the phaseFieldFoam-solver in foam-extend have been tested in this work. The adaptive mesh refinement technique has been the most relevant improvement, drastically reducing the computational cost. Adaptive mesh refinement should be used for any simulations so that the computational domain can be chosen large enough to allow for a velocity close to

zero on bulk-boundaries. The *coupled* solution procedure for the fourth-order Cahn-Hilliard equation (2.21c) has been successfully validated for the present dynamic case. A return to the less consistent *segregated* method is therefore not recommended. The linearisation methods for non-linear terms in the Cahn-Hilliard phase-field model have shown a conflict. On the one hand, the simulations regarding Roisman's wetting experiment [2] have been in best agreement using the *stable*-method. On the other hand, Yun's droplet shape analysis [3] have led to a failure of the *stable*-method resulting in undercuts of the diffuse-interface contact line. The undercuts have only appeared in Yun's experiment indicating that the *stable*-method can fail if the equilibrium contact angle is too large. The *optimal*-method has shown a feasible contact line motion in Yun's droplet shape analysis and is therefore recommended as the default linearisation method for instance. The non-equilibrium bondary condition (2.15) has been studied with respect to the wetting factor evolution. Influence has only been observed for the spreading phase, leading to a faster contact line motion when relaxation processes take longer. However, the spreading phase is already well described using the equilibrium boundary condition (2.10), the latter being clearly recommended. The phase volume conservation error (5.1) has been introduced and is potentially a good validation measure. It is emphasized to include the phase volume conservation error into the PHASEFIELDFOAM message output.

8 Future Work

Before starting new work with the diffuse-interface phase-field model, it is very important to validate the viscosity interpolation model (4.1) and (4.2) with multiple test cases ranging from low to high interface dynamics. Previous works with the PHASEFIELDFOAM-solver [18, 19] have used the *arithmetic* model, which is now complemented by the *harmonic* and *blended* approach, the latter has often been used in the VOF context [34]. Since all viscosity models have shown individual influences when varying the Cahn number, each model should be subject to future work.

An ideal experimental setup for dynamic droplet spreading should include validation data for the wetting factor with much more data points, especially around the maximum spreading radius. Additionally, high-speed images or video material to validate the droplet shapes in side-view should be included, particularly capturing the droplet apex. A bottom view of the rapid wetting process completes the experiment; a suggestion with a high-speed color camera is shown in [37].

A continuation of this work is to validate again the wetting factor for the different linearisation methods using the best matching viscosity model from a preliminary study. Using high equilibrium contact angles, the question would be whether the *optimal* linearisation can appropriately describe the wetting factor progress or, perhaps with a new viscosity model, the undercuts by the *stable* linearisation vanish. Regarding low equilibrium contact angles, there is experimental evidence [35] that the wetting factor forms a plateau around the maximum spread, which indicates a natural pinning process. Does the present phase-field model show such pinning on hydrophilic substrates using the local λ-model and the simple assumption of an equilibrium contact angle? The resulting in a non-constant effective contact angle during simulations is an excellent feature of the phase-field method and should be shown in terms of the Capillary number and compared with models from the VOF context, see [38]. In terms of data evaluation, the contact line velocity should be accessible by sampling and matching both the velocity field and phase-field parameter.

The droplet domain initialization can be modified. In the present work the droplet has been set to be in equilibrium and in direct contact with the solid substrate, which is nonphysical in real applications. The direct contact has been used because it has been seen in pre-studies that an initial droplet height enforces a bubble entrapment on the bottom patch. Although there is experimental evidence of bubble entrapment [37], the simulations have shown that the bubble dimensions are a magnitude to large. Hence, the phase-field model must ensure that the wetting process of the first contact of the droplet with the surface gets faster, so that less air can be trapped. Bottom-view high-speed images are needed for validation because side-views have been seen to have no insight on what is happening around the axis. Regarding the lamella behavior, there is expermental evidence of the formation of toroidal water drops, i.e. a dry-out of the lamella, after impacting on solid surfaces [39]. According to [39], the dynamics in the present case must show toroidal droplets during the spreading phase, which have only been seen in simulations with high mobilities. Other initialization ideas for isothermal systems are the variation of the impact angle or droplet impact on a shallow liquid layer [40].

Regarding the PHASEFIELDFOAM-solver the adaptive mesh refinement currently does not allow the use of *function objects*, which are crucial for run-time calculations. Probably there is a re-numbering of cell addresses after a refinement step, which should be fixed.

Appendices

A Overall Structure of phaseFieldFOAM

The class structure of the master-branch of phaseFieldFOAM is shown, implemented in foam-extend 3.2 or 4.0. On this page the adaption of the diffuse-interface Cahn-Hilliard phase-field equations is shown. The next page shows the embedding of the phase-field equation into the highly modular solver.

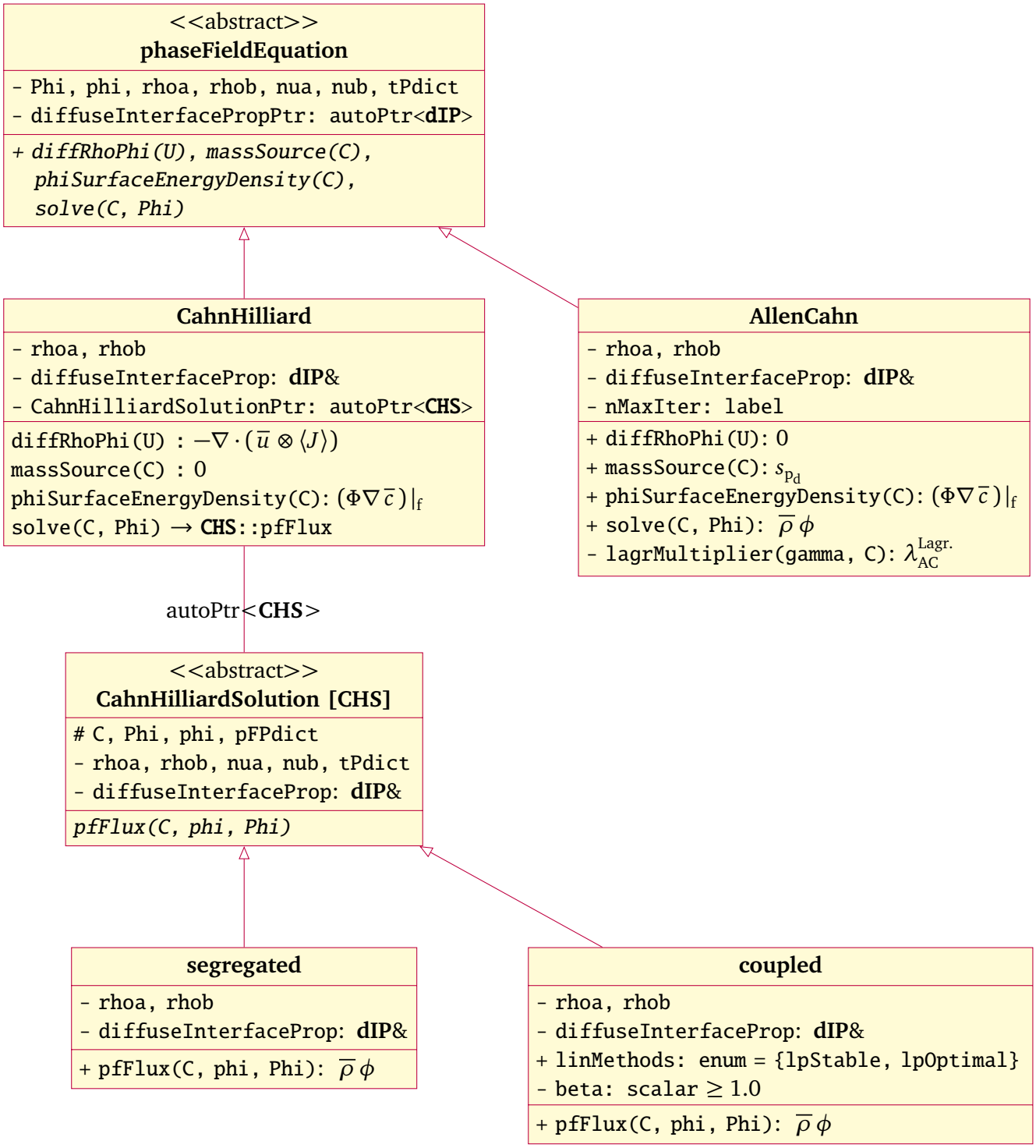

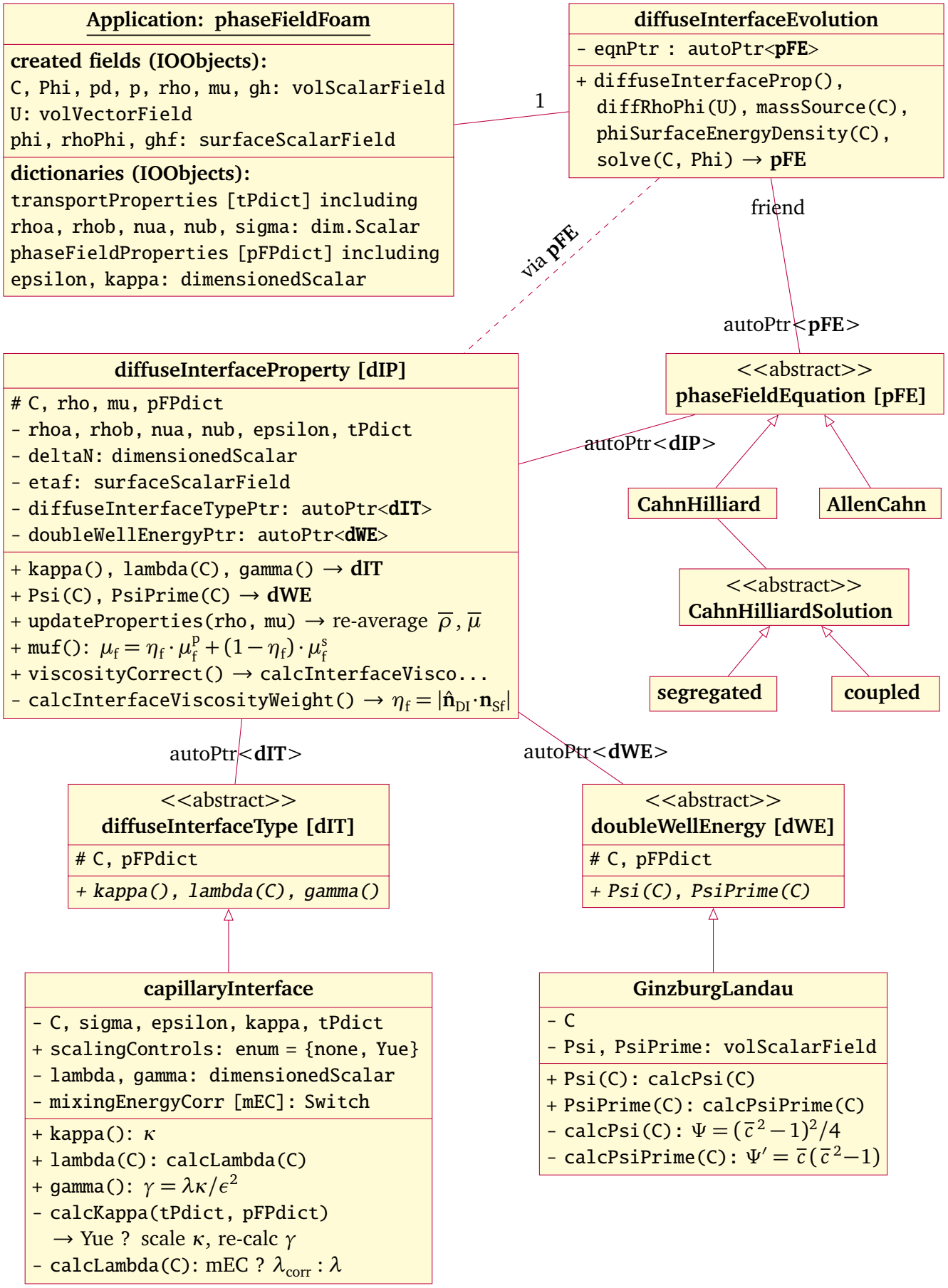
Application: phaseFieldFoam
created fields (IOObjects):
C, Phi, pd, p, rho, mu, gh: volScalarField
U: volVectorField
phi, rhoPhi, ghf: surfaceScalarField
dictionaries (IOObjects):
transportProperties [tPdict] including
rhoa, rhob, nua, nub, sigma: dim.Scalar
phaseFieldProperties [pFPdict] including
epsilon, kappa: dimensionedScalar
1
diffuseInterfaceEvolution
- eqnPtr : autoPtr<pFE>
+ diffuseInterfaceProp(),
diffRhoPhi(U), massSource(C),
phiSurfaceEnergyDensity(C),
solve(C, Phi) → pFE
friend
via pFE
autoPtr<pFE>
diffuseInterfaceProperty [dIP]
C, rho, mu, pFPdict
- rhoa, rhob, nua, nub, epsilon, tPdict
- deltaN: dimensionedScalar
- etaf: surfaceScalarField
- diffuseInterfaceTypePtr: autoPtr<dIT>
- doubleWellEnergyPtr: autoPtr<dWE>
+ kappa(), lambda(C), gamma() → dIT
+ Psi(C), PsiPrime(C) → dWE
+ updateProperties(rho, mu) → re-average $\overline{\rho}, \overline{\mu}$
+ muf(): $\mu_f = \eta_f \cdot \mu_f^p + (1-\eta_f) \cdot \mu_f^s$
+ viscosityCorrect() → calcInterfaceVisco...
- calcInterfaceViscosityWeight() → $\eta_f = |\hat{\mathbf{n}}_{DI} \cdot \mathbf{n}_{Sf}|$
<<abstract>>
phaseFieldEquation [pFE]
autoPtr<dIP>
CahnHilliard
AllenCahn
<<abstract>>
CahnHilliardSolution
segregated
coupled
autoPtr<dIT>
autoPtr<dWE>
<<abstract>>
diffuseInterfaceType [dIT]
C, pFPdict
+ kappa(), lambda(C), gamma()
<<abstract>>
doubleWellEnergy [dWE]
C, pFPdict
+ Psi(C), PsiPrime(C)
capillaryInterface
- C, sigma, epsilon, kappa, tPdict
+ scalingControls: enum = {none, Yue}
- lambda, gamma: dimensionedScalar
- mixingEnergyCorr [mEC]: Switch
+ kappa(): κ
+ lambda(C): calcLambda(C)
+ gamma(): $\gamma = \lambda\kappa/\epsilon^2$
- calcKappa(tPdict, pFPdict)
→ Yue ? scale κ, re-calc γ
- calcLambda(C): mEC ? $\lambda_{corr} : \lambda$
GinzburgLandau
- C
- Psi, PsiPrime: volScalarField
+ Psi(C): calcPsi(C)
+ PsiPrime(C): calcPsiPrime(C)
- calcPsi(C): $\Psi = (\overline{c}^2-1)^2/4$
- calcPsiPrime(C): $\Psi' = \overline{c}(\overline{c}^2-1)$

B Solution and Scheme Dictionaries

```
solvers
{
    pcorr
    {
        solver          PCG;
        preconditioner  DIC;
        tolerance       1e-12;
        relTol          0;
    }

    pd
    {
        solver          PCG;
        preconditioner  DIC;
        tolerance       1e-10;
        relTol          0;
    }

    pdFinal
    {
        solver          PCG;
        preconditioner
        {

            preconditioner  GAMG;
            nVcycles        5;
            tolerance       1e-07;
            relTol          0;
            smoother        DICGaussSeidel;
            nSmoothingSteps 4;
            nPreSweeps      2;
            nPostSweeps     1;
            nFinestSweeps   1;
            cacheAgglomeration false;
            nCellsInCoarsestLevel 100;
            agglomerator    algebraicPair;
            mergeLevels     1;
        }
        tolerance       1e-12;
        relTol          0;
        minIter         2;
        maxIter         50;
    }

    U
    {
        solver          BiCGStab;
        preconditioner  DILU;
        tolerance       1e-06;
        relTol          0;
    }

    C
    {
        solver          PBiCG;
        preconditioner  DILU;
        tolerance       1e-12;
        relTol          0;
    }

    Ccoupled
    {
        solver          GMRES;
        nDirections     5;
        preconditioner  Cholesky;
        tolerance       1e-12;
        relTol          0;
        minIter         2;
        maxIter         500;
    };
}

PIMPLE
{
    momentumPredictor no;
    nOuterCorrectors 3;
    nCorrectors     1;
    nNonOrthogonalCorrectors 2;
    nSubCycles          1;
    pdRefCell           0;
    pRefValue           0;
    pdRefValue          0;
    correctPhi          true;
    checkMeshCourantNo  true;
}
```

Listing B.1: fvSolution dictionary in /system.

```
ddtSchemes
{
    default          Euler;
}

gradSchemes
{
    default          Gauss linear skewCorrected 0.5;
}

divSchemes
{
    default          none;
    div(phi,C)       Gauss skewCorrected Gamma 0.25;
    div(rho*phi,U)   Gauss skewCorrected limitedLinearV 1;
}

laplacianSchemes
{
    default          Gauss linear corrected;
}

interpolationSchemes
{
    default          linear;
}

snGradSchemes
{
    default          corrected;
}

fluxRequired
{
    default          no;
    Phi;
    pd;
    pcorr;
    C;
}
```

Listing B.2: fvSchemes dictionary in /system.

References

[1] P. Yue, J.J. Feng, C. Liu, and J. Shen. A diffuse-interface method for simulating two-phase flows of complex fluids. *J. Fluid Mech.*, 515:293–317, 2004.

[2] Ilia V. Roisman, Romain Rioboo, and Cameron Tropea. Normal impact of a liquid drop on a dry surface: model for spreading and receding. *Proceedings of the Royal Society of London. Series A: Mathematical, Physical and Engineering Sciences*, 458(2022):1411–1430, 2002.

[3] S. Yun. Bouncing of an ellipsoidal drop on a superhydrophobic surface. *Scientific Reports*, 7:17699, December 2017.

[4] Pontus Olin, Stefan B. Lindström, Torbjörn Pettersson, and Lars Wågberg. Water drop friction on superhydrophobic surfaces. *Langmuir*, 29(29):9079–9089, 2013. PMID: 23721176.

[5] Frank Schellenberger, Noemí Encinas, Doris Vollmer, and Hans-Jürgen Butt. How water advances on superhydrophobic surfaces. *Phys. Rev. Lett.*, 116:096101, Feb 2016.

[6] Hans-Jürgen Butt, Nan Gao, Periklis Papadopoulos, Werner Steffen, Michael Kappl, and Rüdiger Berger. Energy dissipation of moving drops on superhydrophobic and superoleophobic surfaces. *Langmuir*, 33(1):107–116, 2017. PMID: 28001428.

[7] D. Jacqmin. Calculation of two-phase Navier-Stokes flows using phase-field modeling. *J. Comput. Phys.*, 155(1):96–127, 1999.

[8] D. Jacqmin. Contact-line dynamics of a diffuse fluid interface. *J. Fluid Mech.*, 402:57–88, 2000.

[9] H. Ding, P.D.M. Spelt, and C. Shu. Diffuse interface model for incompressible two-phase flows with large density ratios. *J. Comput. Phys.*, 226:2078–2095, 2007.

[10] P. Yue, C. Zhou, and J.J. Feng. Sharp-interface limit of the Cahn-Hilliard model for moving contact lines. *J. Fluid Mech.*, 645:279–294, 2010.

[11] J.D. van der Waals. The thermodynamic theory of capillarity under the hypothesis of continuous variation of density. *J. Stat. Phys.*, 20:200–244, 1979.

[12] P.C. Hohenberg and B.I. Halperin. Theory of dynamic critical phenomena. *Rev. Mod. Phys.*, 49, 1977.

[13] H. Abels, H. Garcke, and G. Grün. Thermodynamically consistent, frame indifferent diffuse interface models for incompressible two-phase flows with different densities. *Math. Models Methods Appl. Sci.*, 22(3):1150013, 2012.

[14] J.W. Cahn and J.E. Hilliard. Free energy of a nonuniform system I: interfacial free energy. *J. Chem. Phys.*, 28:258–267, 1957.

[15] V. Ginzburg and L. D. Landau. To the theory of superconductivity. *Zh. Exp. Teor. Fiz.*, 20:1046, 1950.

[16] W. Villanueva and G. Amberg. Some generic capillary-driven flows. *International Journal of Multiphase Flow*, 32(9):1072 – 1086, 2006.

[17] H. Ding, E. Q. Li, F. H. Zhang, Y. Sui, P. D. M. Spelt, and S. T. Thoroddsen. Propagation of capillary waves and ejection of small droplets in rapid droplet spreading. *Journal of Fluid Mechanics*, 697:92–114, 2012.

[18] Xuan Cai, Holger Marschall, Martin Wörner, and Olaf Deutschmann. Numerical simulation of wetting phenomena with a phase-field method using openfoam®. *Chemical Engineering & Technology*, 38(11):1985–1992, 2015.

[19] Xuan Cai, Martin Wörner, Holger Marschall, and Olaf Deutschmann. Numerical study on the wettability dependent interaction of a rising bubble with a periodic open cellular structure. *Catalysis Today*, 273:151 – 160, 2016. 5th International Conference on Structured Catalysts and Reactors, ICOSCAR-5, Donostia-San Sebastián, Spain, 22-24 June, 2016.

[20] Pengtao Yue and James J. Feng. Wall energy relaxation in the cahn–hilliard model for moving contact lines. *Physics of Fluids*, 23(1):012106, 2011.

[21] X.-P. Wang T. Qian and P. Shen. A variational approach to moving contact line hydrodynamics. *Journal of Fluid Mechanics*, 564:333–360, 2006.

[22] Andreas Carlson, Minh Do-Quang, and Gustav Amberg. Modeling of dynamic wetting far from equilibrium. *Physics of Fluids*, 21(12):121701, 2009.

[23] W. Dreyer, J. Giesselmann, and C. Kraus. A compressible mixture model with phase transition. *Physica D: Nonlinear Phenomena*, 273:1–13, 2014.

[24] H. Marschall, L. Cornolti, X. Cai, and M. Wörner. phasefieldfoam – conservative and bounded finite volume discretisation of diffuse interface models on general grids with application to dynamic wetting. In preparation.

[25] Chun Liu and Jie Shen. A phase field model for the mixture of two incompressible fluids and its approximation by a fourier-spectral method. *Physica D: Nonlinear Phenomena*, 179(3):211 – 228, 2003.

[26] Pengtao Yue, Chunfeng Zhou, and James J. Feng. Spontaneous shrinkage of drops and mass conservation in phase-field simulations. *Journal of Computational Physics*, 223(1):1 – 9, 2007.

[27] H. Ding and P.D.M. Spelt. Wetting condition in diffuse interface simulations of contact line motion. *Phys. Rev.*, E 75, 2007.

[28] Y. Sun and C. Beckermann. Diffuse interface modeling of two-phase flows based on averaging: Mass and momentum equations. *Physica D: Nonlinear Phenomena*, 198(3-4):281–308, 2004.

[29] M.E. Gurtin, D. Polignone, and J. Vieñals. Two-phase binary fluids and immiscible fluids described by an order parameter. *Math. Models Meth. Appl. Sci.*, 6(6):815–831, 1996.

[30] David N. Sibley, Andreas Nold, Nikos Savva, and Serafim Kalliadasis. The contact line behaviour of solid-liquid-gas diffuse-interface models. *Physics of Fluids*, 25(9):092111, 2013.

[31] Junseok Kim. Phase-field models for multi-component fluid flows. *Communications in Computational Physics*, 12(3):613–661, 2012.

[32] F. Guillén-González and G. Tierra. On linear schemes for a cahn–hilliard diffuse interface model. *Journal of Computational Physics*, 234:140 – 171, 2013.

[33] David J. Eyre. Unconditionally gradient stable time marching the cahn-hilliard equation. *MRS Proceedings*, 529:39, 1998.

[34] Daniel Deising, Holger Marschall, and Dieter Bothe. A unified single-field model framework for Volume-Of-Fluid simulations of interfacial species transfer applied to bubbly flows. *Chem. Eng. Sci.*, 139:173–195, 2016.

[35] Daniel Rettenmaier. *Numerical Simulation of Shear Driven Wetting*. PhD thesis, Technische Universität Darmstadt, November 2018.

[36] V. V. Khatavkar, P. D. Anderson, P. C. Duineveld, and H. E. H. Meijer. Diffuse-interface modelling of droplet impact. *Journal of Fluid Mechanics*, 581:97–127, 2007.

[37] Wilco Bouwhuis, Roeland C. A. van der Veen, Tuan Tran, Diederik L. Keij, Koen G. Winkels, Ivo R. Peters, Devaraj van der Meer, Chao Sun, Jacco H. Snoeijer, and Detlef Lohse. Maximal air bubble entrainment at liquid-drop impact. *Phys. Rev. Lett.*, 109:264501, Dec 2012.

[38] Ilias Malgarinos, Nikolaos Nikolopoulos, Marco Marengo, Carlo Antonini, and Manolis Gavaises. Vof simulations of the contact angle dynamics during the drop spreading: Standard models and a

new wetting force model. *Advances in Colloid and Interface Science*, 212:1 – 20, 2014.

[39] Y. Renardy, S. Popinet, L. Duchemin, M. Renardy, S. Zaleski, C. Josserand, M. A. Drumright-Clarke, D. Richard, C. Clanet, D. Quéré, and et al. Pyramidal and toroidal water drops after impact on a solid surface. *Journal of Fluid Mechanics*, 484:69–83, 2003.

[40] Edin Berberovic. *Investigation of Free-surface Flow Associated with Drop Impact: Numerical Simulations and Theoretical Modeling*. PhD thesis, Technische Universität Darmstadt, November 2010.